DMSP-SSM/I NASA Algorithm Validation using Primarily Landsat, and Secondarily DMSP and/or AVHRR Visible and Thermal Infrared Satellite Imagery

K. Steffen, R. Barry, A. Schweiger
Cooperative Institute for Research
In Environmental Sciences
University of Colorado, Boulder

NAG5-882

Annual Progress Report
to
National Aeronautics and Space Administration
(Goddard Space Flight Center)

June 1988

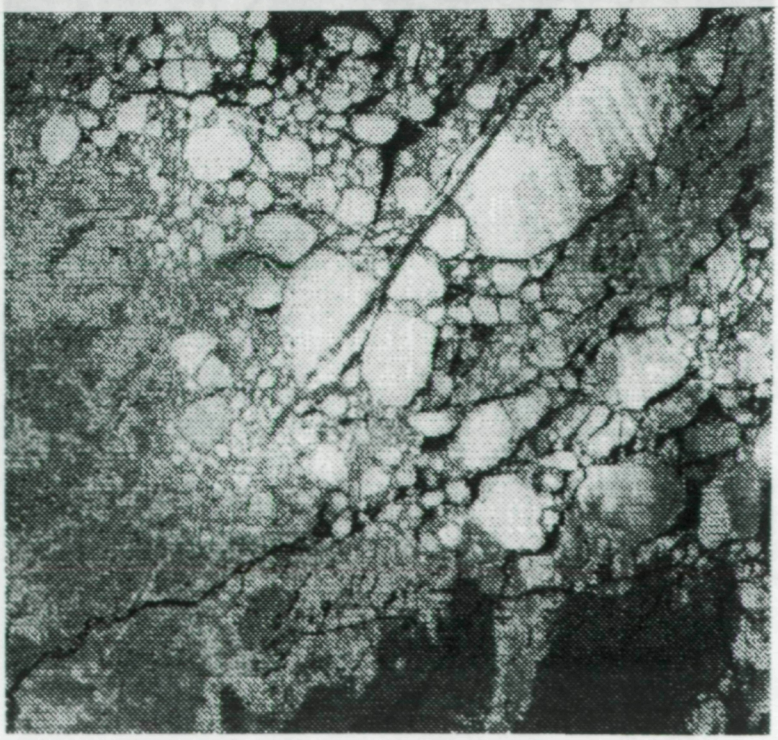

Table of Contents

Cover Picture: Ice conditions in the Bering Sea southeast of St. Lawrence Island during NASA DC-8 sea ice mission (Landsat 4 Image, March 13, 1987). Note condensation trail of NASA DC-8 aircraft in the center of the image. Landsat image from Alaskan Quicklook facility, Geophysical Institute, University of Alaska, Fairbanks.

1. Objectives

The overall approach to the DMSP SSMI sea ice validation effort is to demonstrate a quantitative relationship between the SSMI-derived sea ice parameters and those same parameters derived from other data sets including visible and infrared satellite imagery, aerial photographic and high-resolution microwave imagery from aircraft. The overall question to be addressed is to what accuracy (relative to these other observations) can we determine the following sea ice parameters:

(1) position of the sea ice boundary
(2) total sea ice concentration
(3) multiyear sea ice concentration

Specific tasks include (1) a study of the interrelationship of surface information content and sensor spatial and spectral resolution in order to establish relationships between ice surface features and the manner in which they are expressed in the satellite observations; and (2) apply these relationships to map the sea ice features which can be used to evaluate NASA's proposed SSM/I sea ice algorithms.

Other key points to be addressed include the accuracy to which these parameters can be determined in different regions (e.g. marginal ice zone such as Bering Sea, Arctic ocean such as Beaufort Sea); the accuracy of these parameters for different seasons; the accuracy of the algorithms weather filter under different weather conditions; and the effectiveness of the 85.5 GHz channels to locate the ice edge.

2. Approach

In two separate meetings at NSIDC in Boulder on July 16, 1987 (W.J. Emery, D.T. Eppler, J. Hawkins, R. Weaver, K. Steffen) and July 23, 1987 (D. Cavalieri, W.J. Emery, R. Waever, K. Steffen) we agreed upon several intercomparison case studies to be carried out during the SSM/I validation period. For each case study (also called "window") we plan to derive as much quantitative sea ice information as possible from four different satellites (Landsat MSS, NOAA AVHRR, DMSP OLS, DMSP SMMR) for each scene (e.g. percent of ice concentration) before averaging over on SSM/I footprint and comparing with the corresponding SSM/I parameter. The Landsat imagery would also be used to check the AVHRR, OLS and SMMR ice products (see Fig. 1).

The windows were chosen for different geographic regions where different radiometric properties of the sea ice can be expected, and for all seasons (Tab. 1) to meet the objectives mentioned in chapter 1. Due to the delayed launch of the DMSP SSM/I sensor and its malfunctioning during the winter months, we had postpone some data acquisition of Landsat data to summer 1988 and winter 1988/89.

In addition to the Landsat/AVHRR/OLS/SMMR - SSM/I intercomparison, we also collected Landsat images in the Bering and Beaufort Sea during the NASA DC-8 flight missions in March 1988. A total of 13 scenes were collected which coincides with the profile measurements of the passive microwave and SAR measurements (Appendix A). This data will provide an unique opportunity for the evaluation of a multifrequency algorithm (visible, passive and active microwave), particular in view of the forthcoming Earth Observing System (EOS).

A complete list of Landsat acquisition up to date (May 1988) with a brief description of the ice conditions is given in Appendix A. In the following chapter the methodology of ice typing and ice concentration classification for Landsat imagery, and the

comparison of Landsat, AVHRR, SMMR and SSM/I derived ice products is presented.

Figure 1: Flow diagram for intercomparison of sea ice parameters derived from five different satellites (Landsat, AVHRR, OLS, SMMR, SSM/I) during selected case studies (Tab. 1).

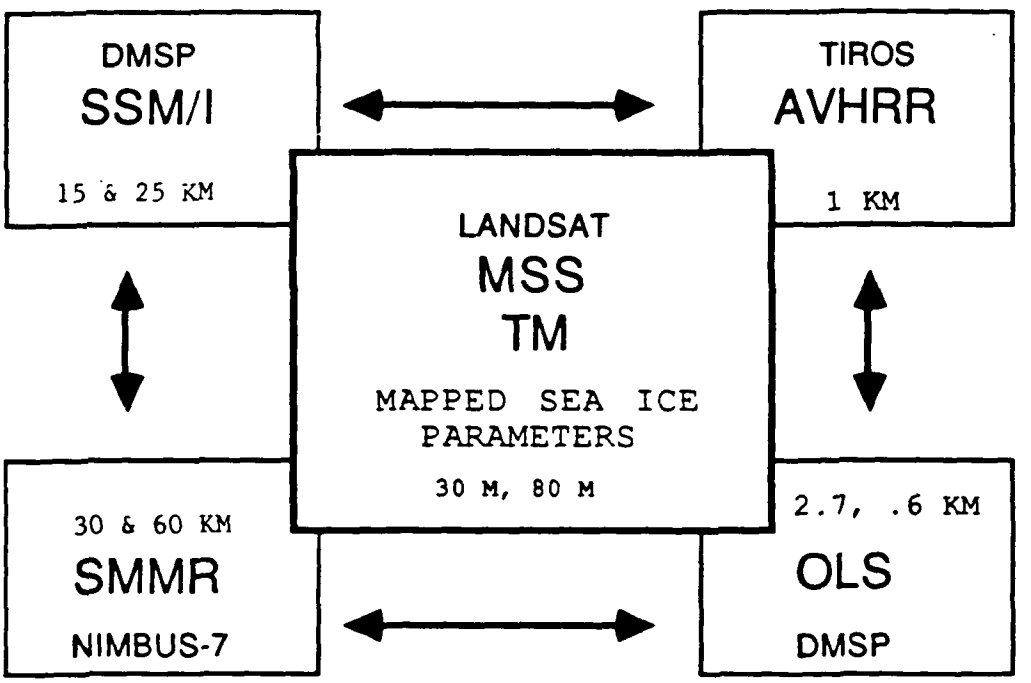

Table 1: Geographic and seasonal distribution of case studies (window) selected for the validation of the SSM/I derived ice products.

Window	Area	Season	Objective
1	Beaufort Sea	Fall	Position of ice edge, low MY ice conc.
2	Weddell Sea	Fall	high FY ice concentration
3	Beaufort Sea	Spring	FY/MY ice concentration (premelt)
4	Chukchi Sea	Spring	FY/MY ice concentration (premelt)
5	Bering Sea	Spring	FY ice conc., ice edge, FY ice typing (premelt)
6	Baffin Bay	Summer	FY ice conc., FY ice typing (onset of melt)
7	Barents Sea	Summer	FY/MY ice conc., ice edge (melt period)
8	Greenland Sea	Summer	FY/MY ice conc., ice edge (melt period)
9	Weddell Sea	Summer	FY ice conc., FY ice typing (no melt)
10	Beaufort Sea	Winter	FY/MY ice conc., FY ice typing
11	Baffin Bay	Winter	FY ice conc., FY ice typing

FY: First-year
MY: Multi-year

3. Results

3.1 Methodology for ice classification using Landsat and AVHRR imagery

The acquisition of high resolution Landsat MSS data fulfills a twofold purpose :

1) Validation and fine-tuning of NASA SSM/I sea ice parameter algorithms.
2) Comparison of Landsat derived ice concentrations with those calculated from AVHRR and OLS imagery to investigate the possibility of using lower resolution imagery for a validation of SSM/I sea ice parameters over large areas.

Cloud-free Landsat imagery was selected for a range of ice conditions and geographic locations to allow for a validation of the sea ice algorithms for a variety of ice concentrations and ice types. A list of already acquired imagery including their geographic locations and prevailing ice conditions is included in Appendix A.

Landsat imagery was acquired in two formats:

1) Digital imagery :

Geometrically and radiometrically corrected Landsat MSS imagery at 80 m resolution is available from EOSAT corporation. This imagery can easily be geolocated and regridded to match the SSM/I grid format. Due to the high reflectance of ice, MSS channels 1-3 are frequently saturated and can only be utilized in the ice parameter classification under low sun angle illumination conditions. However, reflectance differences between thin ice types and open water are greatest in the near infrared spectral range, so that MSS channel 4 is most suitable for the determination of ice concentrations. The combination of channels 1 and 4 under low illumination conditions (L1B see Appendix A) allows the identification of some cloud types and cloud shadows. (Fig. 2).

2) Landsat MSS photographic transparencies :

Due to data communication problems with the satellite downlink (TDRS) no digital imagery is available for some areas in the Bering Sea but photographic transparencies could be ordered through the Alaskan Quicklook system operated by the University of Alaska's Geophysical Institute. This imagery is received in real time and recorded on photographic transparencies. Data are geometrically corrected for earth rotation but geolocation information is unreliable due the lack of accurate ephemeris and real time satellite attitude data. Landsat MSS channel 4 data were therefore acquired in swaths so that at least one frame within each swath contains identifiable landmarks. Through comparison with maps, a geolocation correction can be calculated for the entire path resulting in a approximate geolocation error of 1.5 km. For the subsequent determination of ice concentration and sea ice types the transparencies were digitized using a high resolution scanner, geolocated using the above outlined procedure and projected to the polar stereographic projection (True at 70 degree latitude) used for the SSM/I gridded sea ice products.

Classification :

For the determination of ice concentration MSS channel 4 is most useful, since it displays the greatest reflectance differences between thin ice (dark nilas) and open water. The capability to distinguish thin ice types seems crucial for the validation of the SSM/I ice parameters since SMMR derived sea ice concentrations showed an underestimation in the presence of thin ice. (Steffen and Maslanik, in press). Channels 1-3 are only usable at low sun angles since they easily saturate. A combination of channel 1 and 4 appeared useful under those conditions for the distinction of clouds and cloud shadows (see Fig. 3).

Methods of Classification :

1) Threshold techniques

Using training areas, the brightness value ranges for different ice types and open water are determined. By selecting appropriate

thresholds an image can be classified into different ice types (Fig. 2). If only channel 4 is available, clouds as well as land areas need to be classified manually. For the determination of ice concentration (main objective) the class spectrum was reduced to open water and white ice. The identification of a third, sub-resolution feature class seemed necessary for the Weddell sea scene (L2 see Appendix A). The formation of new ice is not expected in the Weddell sea at that time of the year, so that brightness values falling between open water and white can only be attributed to the combination of open water and white ice at sub-resolution scales. By assigning a particular brightness value range to this 'sub-resolution' class, it can be considered separately in the calculation of ice concentration. Correlations between SSM/I and Landsat derived ice concentrations were greatest when this class was included as 75% ice concentration. Following classification, ice concentrations can be calculated for the corresponding SSM/I 25 by 25 km grid boxes.

2) Tie point algorithm :

The above described assignment of a 'sub-resolution feature class' to a particular ice concentration neglects the fact that brightness values anywhere between the classes open water and white ice actually represent sub-resolution features. If open water and white ice are the only two classes that are present the assumption can be made that all brightness values in between those classes must represent ice concentrations at sub-resolution. The following algorithm (Zwally et al., 1982) was devised to more realistically account for the presence of ice floes smaller that the MSS resolution.

$$Ic = (D_x - D_l / D_h - D_l) * 100 \qquad (1)$$

where:

Ic = ice concentration

D_x = Brightness value representing ice conc. Ic

D_l = Brightness value for open water

D_h = Brightness value for white ice

Tie-points were found using training areas for open water and large white ice floes, where D_b represents the mean brightness for that floe - 1 standard deviation.

Fig. 3 shows a comparison of the tie-points vs. the threshold algorithm for grid cells of 5 by 5 km. The tie-points algorithms seems to produce a more realistic distribution of ice concentrations. Zwally et al (1982) found this algorithm to produce higher correlations with ESMR derived sea ice concentrations due to its capability of accounting for size ice floes small than the sensor resolution.

In the presence of thin clouds, transparent enough to allow the distinction between open water and white ice, threshold and tie point algorithms can be combined for images containing a considerable amount of thin clouds.

Comparison with AVHRR imagery

Local area coverage AVHRR data at 1.1 km resolution were obtained from NESDIS for the Weddell sea area (L2 see Appendix A). The image was geolocated using geolocation information imbedded in the NESDIS data format. Due to the low illumination, only the thermal channels provided enough information to distinguish between open water and ice. The tie-points ice concentration algorithm developed for Landsat imagery was applied to the AVHRR data and ice concentrations calculated for 5 by 5 km grid cells. Fig. 4 shows a comparison between the Landsat and AVHRR derived ice concentrations for the Weddell Sea area. AVHRR ice concentrations are substantially lower. This effect can be attributed to a combined effect of the utilization of different spectral bands, as well as to the lower resolution of the AVHRR sensor. When more, accurately geolocated AVHRR imagery becomes available, (To be provided by Emery et al.) a detailed investigation of the causes of the ice concentration discrepancy can be undertaken. However, preliminary

parameters using different sensors requires great caution and the availability of accurately determined correction factors.

Figure 2 Ice classification of Landsat image (L1B subsection) using threshold algorithm based on MSS channels 1 and 4. Right display shows. Red : Open water, Green : grey ice, Blue : white ice, Pink : Clouds, Yellow : Cloud shadows. Left side of display shows the unclassified image.

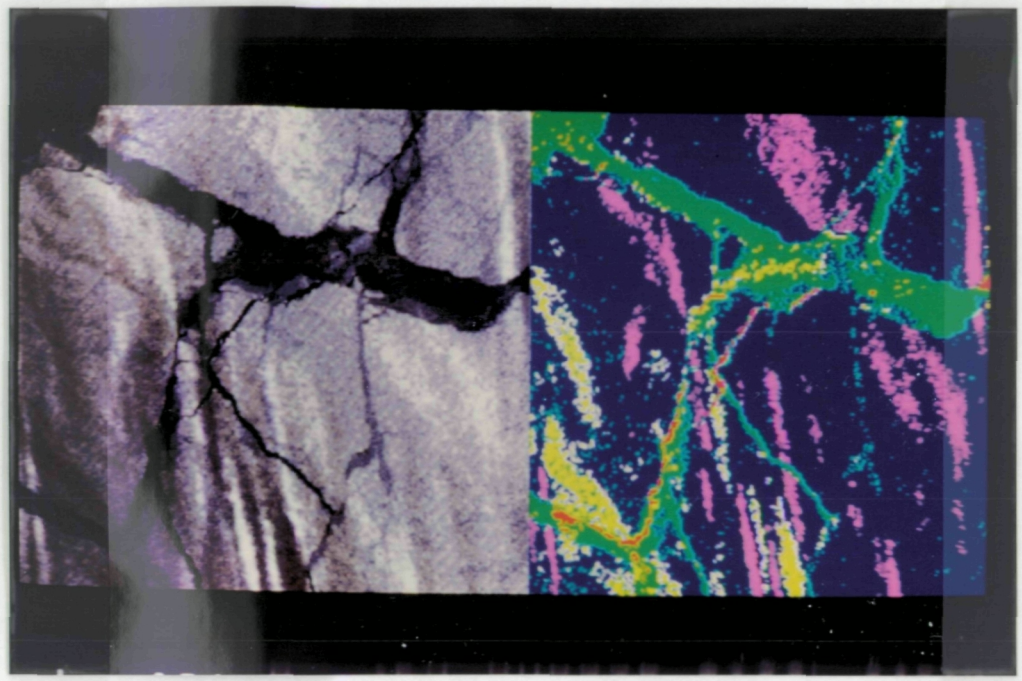

Figure 3 Comparison of tie-points vs. threshold ice concentration algorithms for Landsat image L2 . Histograms are based on 5km grid cells.

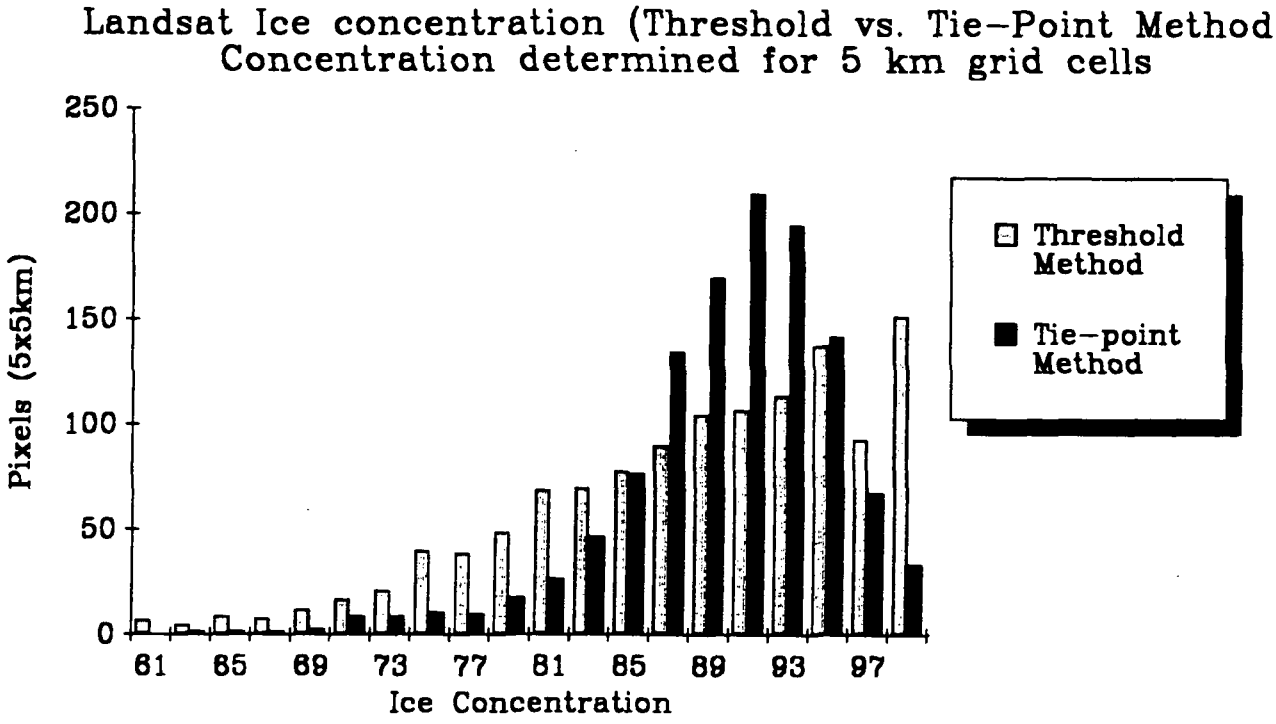

Figure 4 Comparison of ice concentrations based on the tie-points algorithm from Landsat MSS and AVHRR data in the Weddell sea.

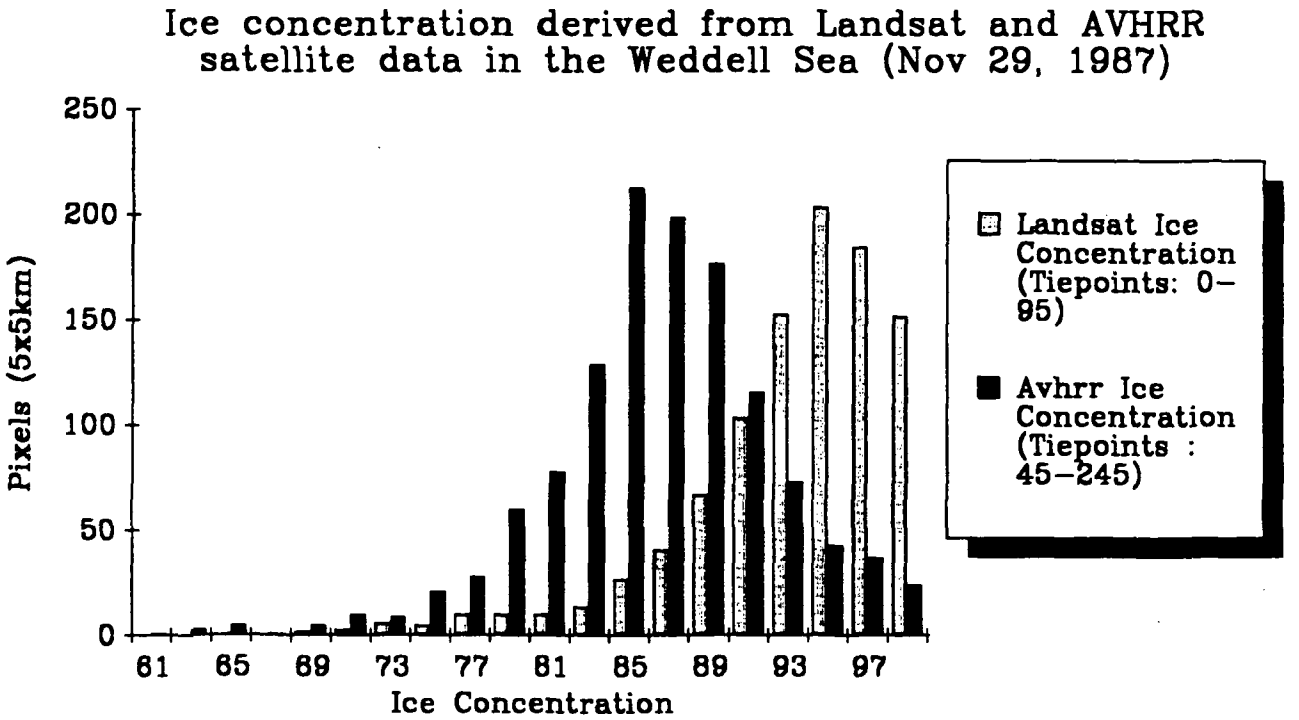

3.2 Comparison of SMMR and Landsat derived ice products

An intercomparison was carried out for microwave radiance and sea ice concentration derived from Nimbus 7 SMMR data with ice parameters interpreted from Landsat imagery. Landsat derived sea ice parameters were already available in digital form from a previous project for northern Baffin Bay (Sea Ice Atlas of Northern Baffin Bay, published by Ito, 1982, ETH-Zurich). The intercomparison covers the time period March to June 1981. The study focuses on the seasonal variations of white ice brightness temperatures, the effects of adjacent land on the sea ice brightness temperature, the polarization ratio of first-year ice types, and the comparison of the ice concentration derived from SMMR and Landsat data. The results were written up and submitted to the Journal of Geophysical Research, Oceans (paper accepted for publication, May 1988, see Appendix C).

In a second study the first-year ice type distribution was studied in an Arctic polynya during winter. A paper was presented at the Conference-Seminar: Polynyas with special reference to the North Water, McGill University, Montreal in October 1987, which is attached in Appendix D.

The results of the first study can be summarized as following:

The main objectives of this comparison between Nimbus 7 SMMR and Landsat MSS data were: (1) to study the seasonal variations of white ice brightness temperatures; (2) to test the ability to classify ice types (e.g. nilas, grey ice) based on SMMR data; (3) to determine the accuracy of ice concentration derived from Nimbus 7 SMMR data relative to Landsat data; and (4) to identify reasons for discrepancies between Landsat and SMMR-derived ice concentrations.

The analysis has shown that pack ice brightness temperature (T_B) is on the average 10 K higher than fast ice T_B for vertically

polarized data, and 15 K higher for horizontally polarized data at 18 and 37 GHz during the pre-melt period. During the onset of melt, the mean difference in T_B between pack ice and fast ice decreases and is nonexistent during the melt period. The three effects - (1) thinner pack ice compared to fast ice in the North Water region; (2) higher air temperatures in the pack ice areas due to a large sensible heat flux; and (3) thicker snow cover on fast ice - are assumed to account for the observed T_B difference. Accurate geolocation of SMMR data is important during periods of pre-melt and onset of melt since the misclassification of a SMMR footprint containing 50% snow-covered land resulted in an error of -3 K at 18 GHz, -6 K at 37 GHz, respectively, compared to a SMMR footprint over 100% fast ice. No significant change in T_B was observed for the melt period as long as land and ice were covered with wet snow.

Under certain circumstances, the polarization ratios of 18 and 37 GHz provide a possibility to classify ice types such as white ice, grey ice, nilas and open water. With the present resolution of the SMMR pixels (30x30 km for 37 GHz, 60x60 km for 18 GHz), this ice type classification seems feasible for large homogeneous ice areas depicting a single ice type. For mixed-ice SMMR footprints, a clear distinction is not possible.

A comparative analysis was carried out between estimates of ice concentrations derived from SMMR and Landsat data. Versions of the SMMR Team algorithm (ST_{18} and ST_{37}) and a single-channel linear interpolation algorithm (LI_{37}) were used to derive the SMMR ice concentration. During pre-melt and melt onset, the SMMR algorithms show less total ice concentration (3.5% for ST_{18}, 2.8% for ST_{37}, and 10% for LI_{37}) compared to the Landsat ice concentration. Largest differences (9.7% for ST_{18}, and 13.1% for ST_{37}) occurred during the melt period (June 8, 1981). At high ice concentrations (according to the Landsat classification), the ST algorithms tend to show lower amounts of ice while, at low concentrations, ST yields greater amounts of ice. These differences may be due to the

ability of SMMR to detect sub-resolution leads and thin ice types invisible on the Landsat images, and partially due to surface effects on the ice and open water. For individual footprints, the correlation coefficient for the SMMR ST_{18} and Landsat derived concentrations varied between 0.78 (June 8, 1981) and 0.3 (May 5, 1981). The somewhat poor correlation coefficients for individual footprints can be attributed to the dynamic nature of the pack ice in the North Water area, and to the fact that 50% of the power received by the radiometer lies outside the FOV.

Satellite passive microwave data are essential for long-term monitoring of the sea ice cover in order to study climate fluctuations. In order to detect changes in the ice cover, the accuracy of ice parameters derived from passive microwave data must be known. The Landsat/SMMR comparison shows that the overall ice concentration can be retrieved from SMMR data to a comparative agreement of 3.5% during the pre-melt and onset of melt, and 10% during melt periods.

3.3 Comparison of SSM/I and Landsat derived ice products

During the preparation of this report, we noticed that our analysis of ice concentration is based on a grid size of 25 x 25 km instead of 50 x 50 km as proposed by the validation team. We will modify our programs accordingly. With the larger grid size we would expect a better agreement between SSM/I and Landsat derived ice concentrations.

Window L1A: Beaufort Sea (Sept. 17, 1987)

Ice conditions: low ice concentration of second and multiyear ice, size of ice floes varying from 80 m (or lower; 80 m is best resolution for Landsat MSS) to 10 km. A few low stratus clouds were present during the acquisition of the image, however, ice concentration beneath the cloud layer could be estimated as the cloud were partly transparent (Photo 1, 2).

The objective of this window is the validation of low second-year and multiyear ice concentration at the end of the melt period. Two Landsat scenes were acquired from the Alaskan Quicklook facility at Gillmore Creek (see Chapt. 3.1) and navigated to an accuracy of 1.5 km. The tie-points used for the SSM/I ice concentration calculation were the mean brightness temperatures of min and max values over a time period of five days. During that time period strong winds occurred over the open water which resulted in relatively high values for the open water tie-points. A longer time period will be analyzed when Wentz tapes become available for that entire period. For the analysis the following tie-points (minimum and maximum T_B) were used:

19 GHz/V:	183 K,	245 K
19 GHz/H:	106 K,	225 K
37 GHz/V:	205 K,	240 K
37 GHz/H:	134 K,	220 K

The Landsat ice concentration was calculated based on the tie-point method (see Chapt. 3.1). Three different analyses were carried out to study deviations in ice concentration due to different SSM/I orbit corrections. In the first analysis no orbit corrections were applied (Fig. 5). The difference between Landsat and SSM/I ice concentration for all 25 x 25 km grid cells showed a standard deviation of 15.1%. SSM/I concentrations were higher compared to Landsat values by as much as 53%. In the second analysis the SSM/I orbit was corrected for a negative pitch angle of -0.5^0 and a positive yaw angle of 0.5^0. The standard deviation of the difference decreased to 12.2% (Fig. 6). Best agreement between the two ice concentrations was received for a pitch angle of -0.8^0 and a yaw angle of 0.8^0 (Fig. 7). The time difference of 6 hours between Landsat and DMSP satellite path over the Beaufort Sea during a period of strong surface wind could explain part of the disagreement between Landsat and SSM/I ice concentration. These results are still preliminary in view of the "crude" tie-point selection method, and therefore, more analysis is needed.

Photo 1: Landsat Image of sea ice in the Beaufort Sea on September 17, 1987. The picture does not display the full 80 m resolution of the Landsat image. The scene deppicts an area of 185 km in width.

Ice conditions: low ice concentration of second and multiyear ice, size of ice floes varying from 80 m (or lower; 80 m is best resolution for Landsat MSS) to 10 km. A few low stratus clouds were present during the acquisition of the image, however, ice concentration beneath the cloud layer could be estimated as the cloud were partly transparent.

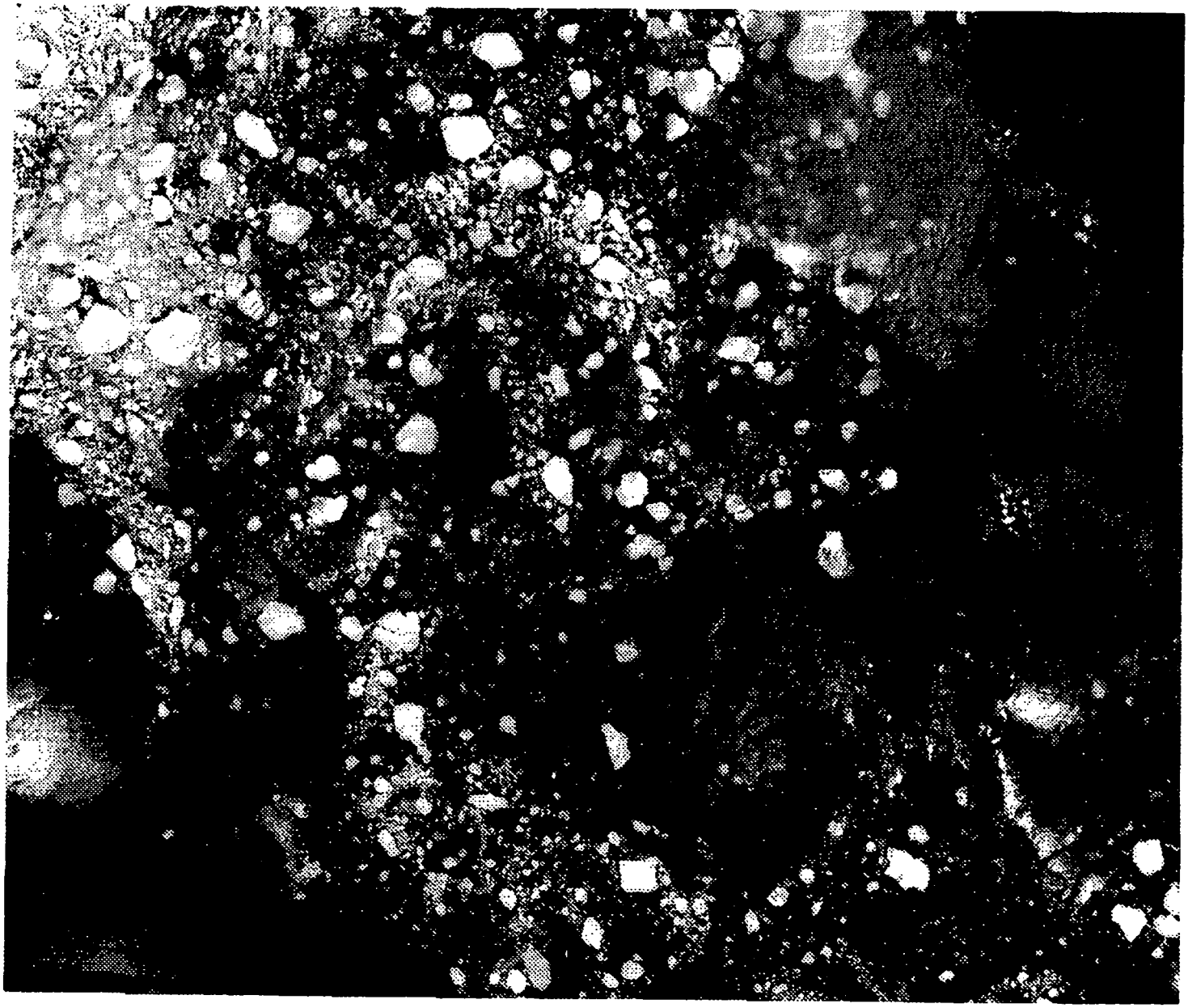

Photo 2: Landsat Image of sea ice in the Beaufort Sea on September 17, 1987. The picture does not display the full 80 m resolution of the Landsat image. The scene depicts an area of 185 km in width.

Ice conditions: low ice concentration of second and multiyear ice, size of ice floes varying from 80 m (or lower; 80 m is best resolution for Landsat MSS) to 4 km. Low stratus clouds obscure the sea surface on the left. The coast line of Alaska (Prudhoe Bay) is visible in the lower right corner.

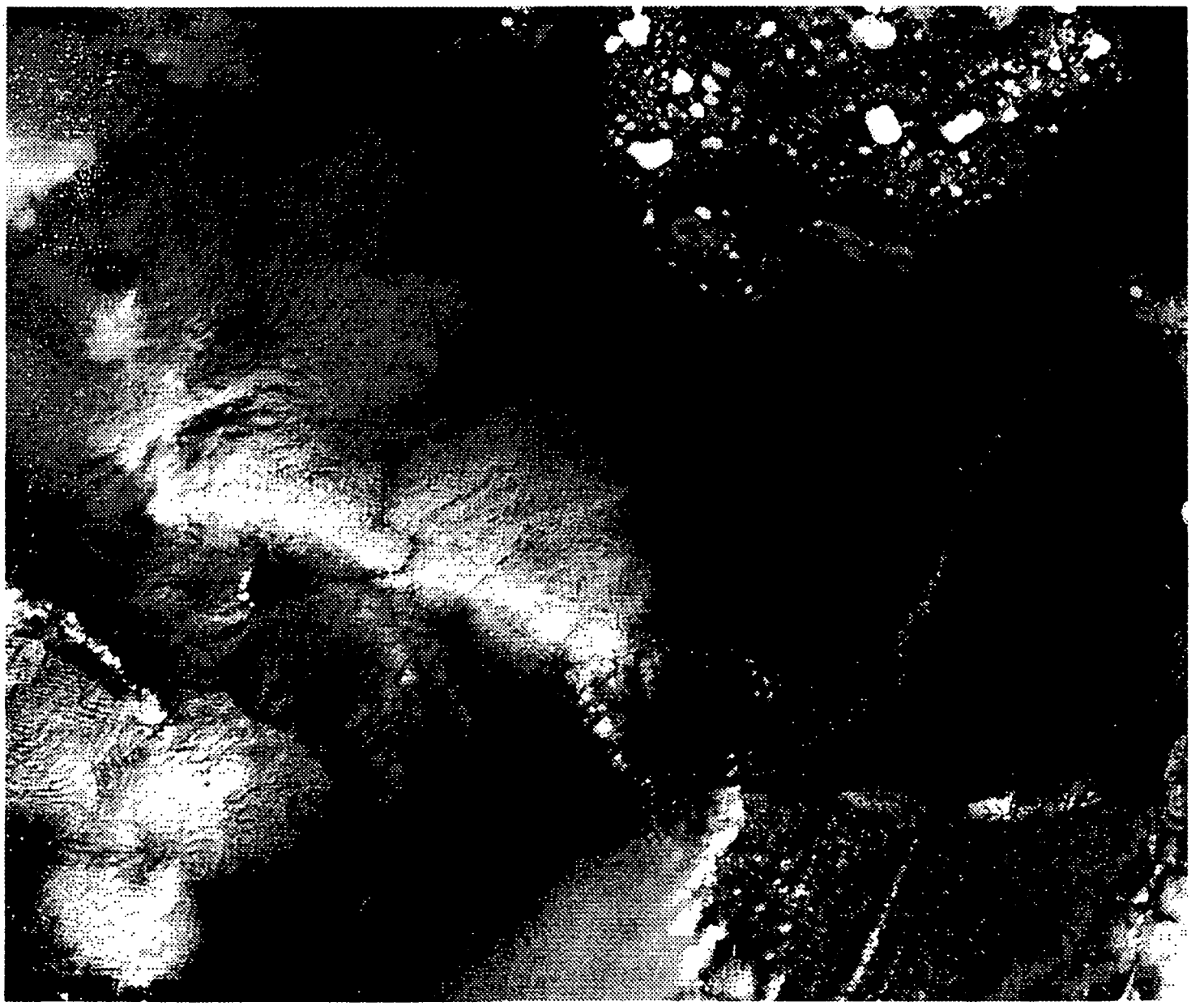

Figure 5 Ice concentration derived from Landsat image based on tie-point method (see Chapt. 3.1) versus SSM/I derived ice concentration for each 25 x 25 km grid cell in the Beaufort Sea on September 17, 1987. The standard deviation of the error (Landsat minus SSM/I ice concentration) is 15.1 %. No orbit corrections were applied for the SSM/I data.

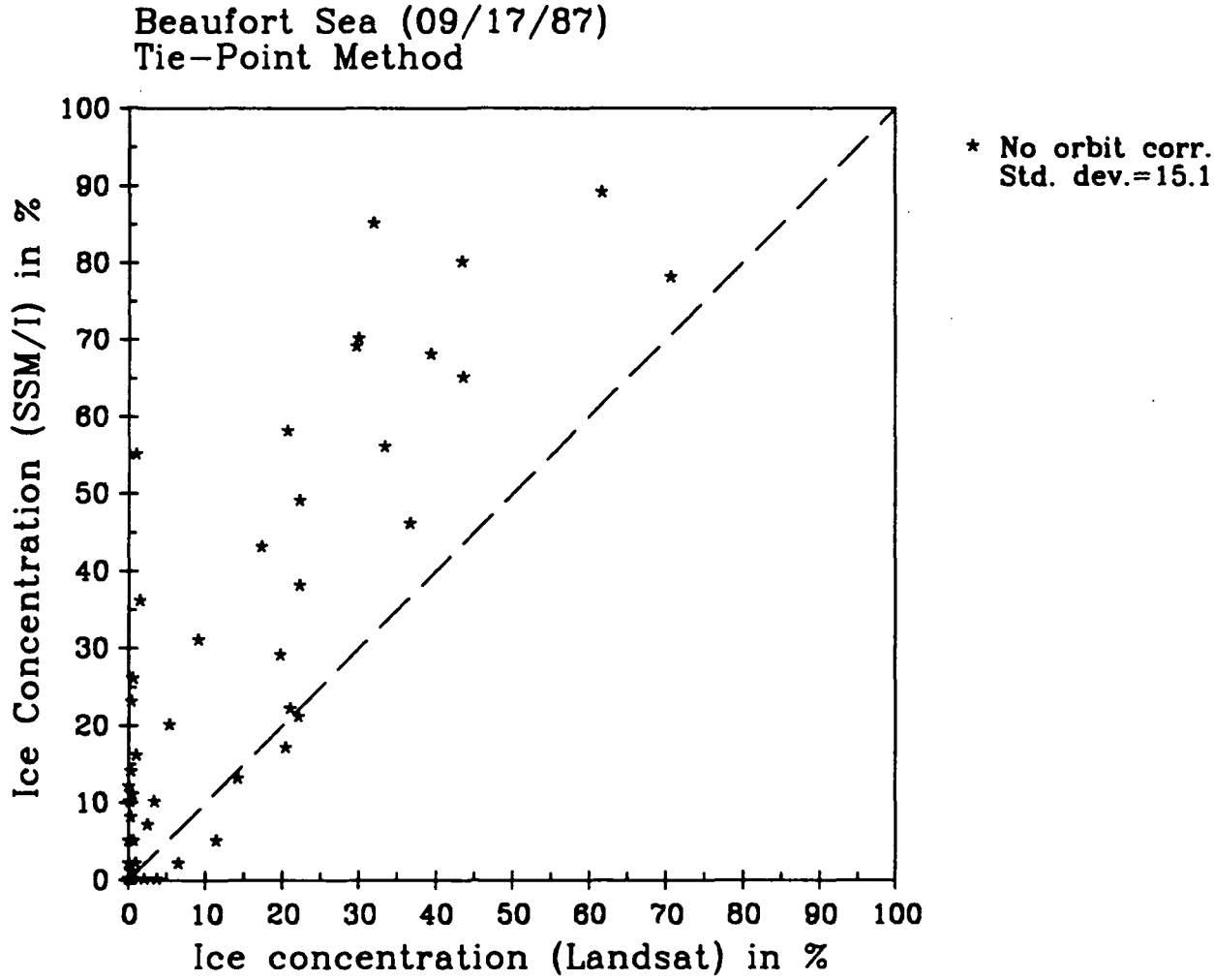

Figure 6 Ice concentration derived from Landsat image based on tie-point method (see Chapt. 3.1) versus SSM/I derived ice concentration for each 25 x 25 km grid cell in the Beaufort Sea on September 17, 1987. The standard deviation of the error (Landsat minus SSM/I ice concentration) is 12.5 %. SSM/I orbit corrected with pitch = -0.5^0 and yaw = 0.5^0.

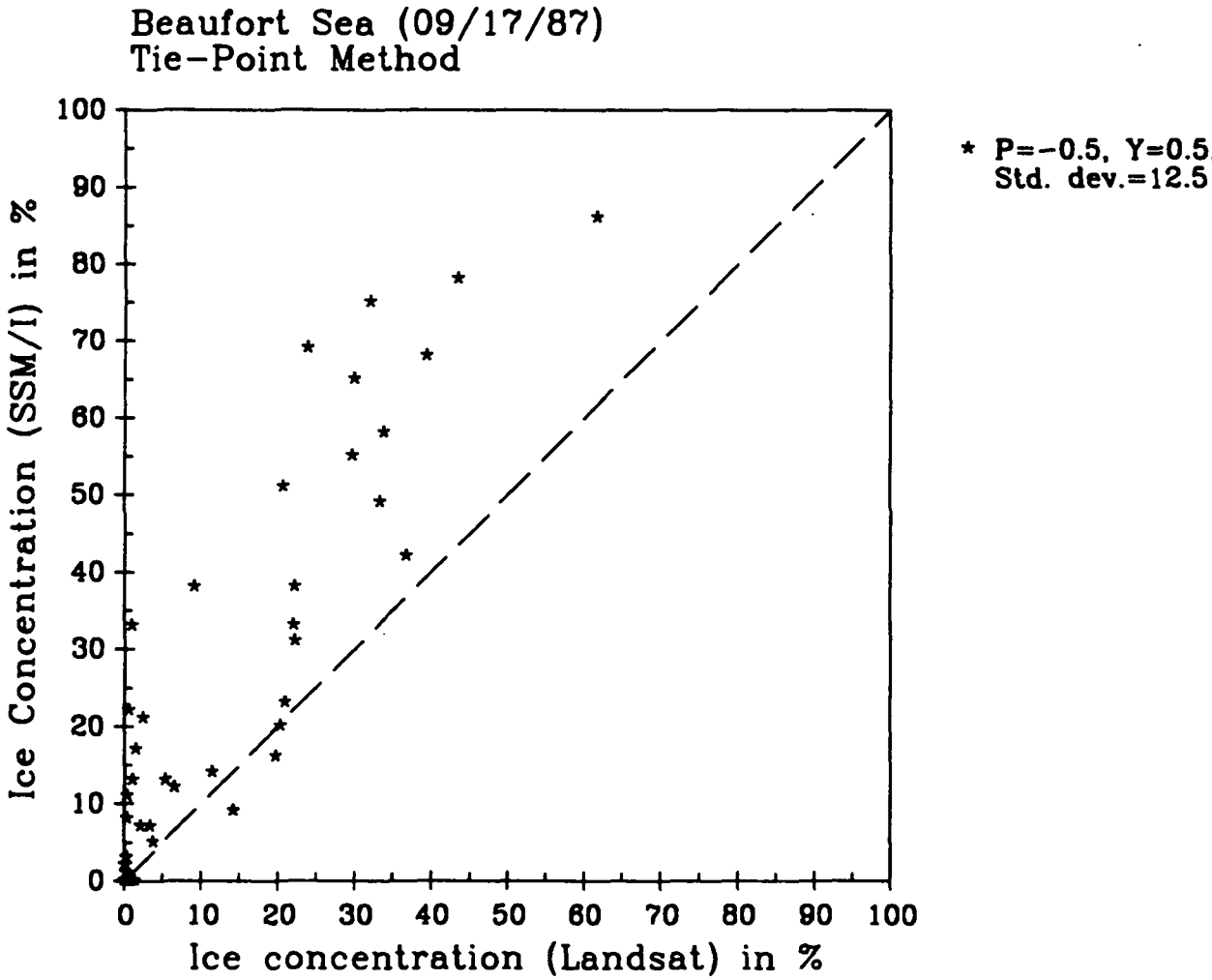

Figure 7 Ice concentration derived from Landsat image based on tie-point method (see Chapt. 3.1) versus SSM/I derived ice concentration for each 25 x 25 km grid cell in the Beaufort Sea on September 17, 1987. The standard deviation of the error (Landsat minus SSM/I ice concentration) is 12.2 %. SSM/I orbit corrected with pitch = -0.8^0 and yaw = 0.8^0.

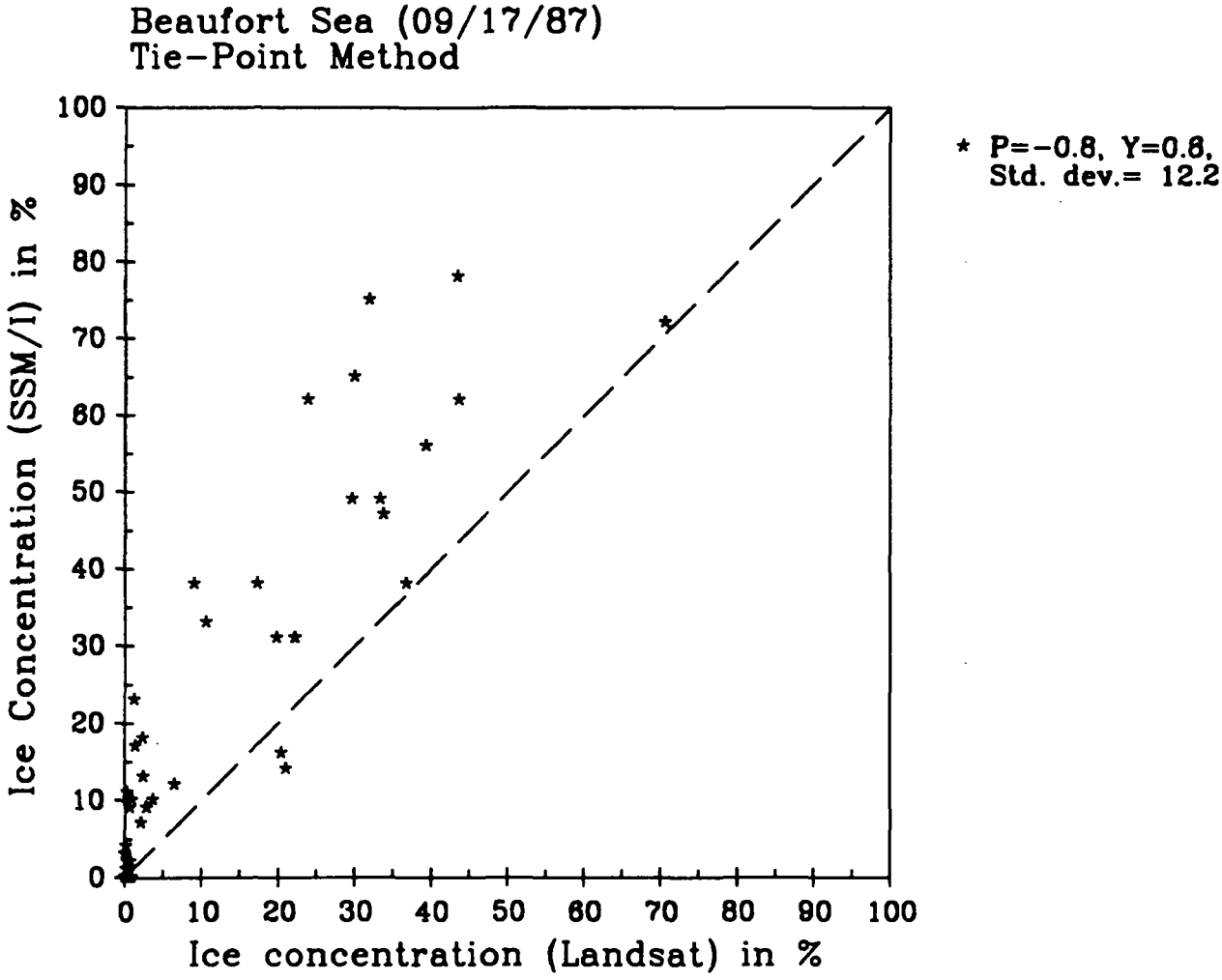

Window L2: Weddell Sea (Nov. 29, 1987)

Ice condition: close pack ice with the concentrations between 8/10 and 9/10, composed of floes mostly in contact. Floes size varied from small (<100 m) to giant (>10 km), with the largest floe being approximately 40 km in diameter. No large open water area occurred except in leads. A few alto cumulus clouds (< 5 %) were obscuring the ice surface (Photo 3).

The objective of this window is the validation of high first-year ice concentration during premelt. The tie-points for the NASA sea ice concentration algorithm were derived from a one week time series of SSM/I brightness temperatures. This time analysis of tie-points for the Weddell Sea will be continued in order to derived locally tuned tie-points for the algorithm. Fig. 8 dispicts the brightness temperatures for the Weddell Sea on November 29, 1987. The following tie-points were used:

19 GHz/V:	177 K,	266 K
19 GHz/H:	103 K,	254 K
37 GHz/V:	187 K,	261 K
37 GHz/H:	131 K,	253 K

The SSM/I ice concentration was compared with the ice concentration derived from the Landsat MMS databased on the tie-point method (see Chapt. 3.1). The analysis shows a 2.15 % standard deviation of the error (Landsat ice concentration minus SSM/I ice concentration) which can be considered a good agreement. Figure 9 depicts a scatter plot of the two derived ice concentrations for each 25 x 25 km grid cell. If the threshold method was applied (white ice and open water only) for the Landsat ice concentration, the standard deviation of the error increased to 4.25 % (Fig. 10). A third comparison was carried out with a threshold method for the Landsat ice classification using white ice, open water and ice/water mixture. The results are shown in Fig. 11. The tie-point ice classification method can be assumed to be the most accurate

one (as already discussed in Chapt. 3.1). No orbit corrections were needed for that date as the comparison of 37 GHz/V brightness temperatures of two consecutive orbits for the same area showed best agreement for zero pitch and yaw angles.

Photo 3: Landsat Multispectral Scanner Image of sea ice in the Weddell Sea on November 29, 1987. The picture does not display the full 80 m resolution of the Landsat image. The scene depicts an area of 185 km in width.

Ice condition: close pack ice in which the concentration is 8/10 to 9/10, composed of floes mostly in contact. Floes size varied from small (<100 m) to giant (>10 km), with the largest floe of approximately 40 km in diameter. No large open water area except in leads. A few alto cumulus clouds (< 5 %) were obscuring the ice surface.

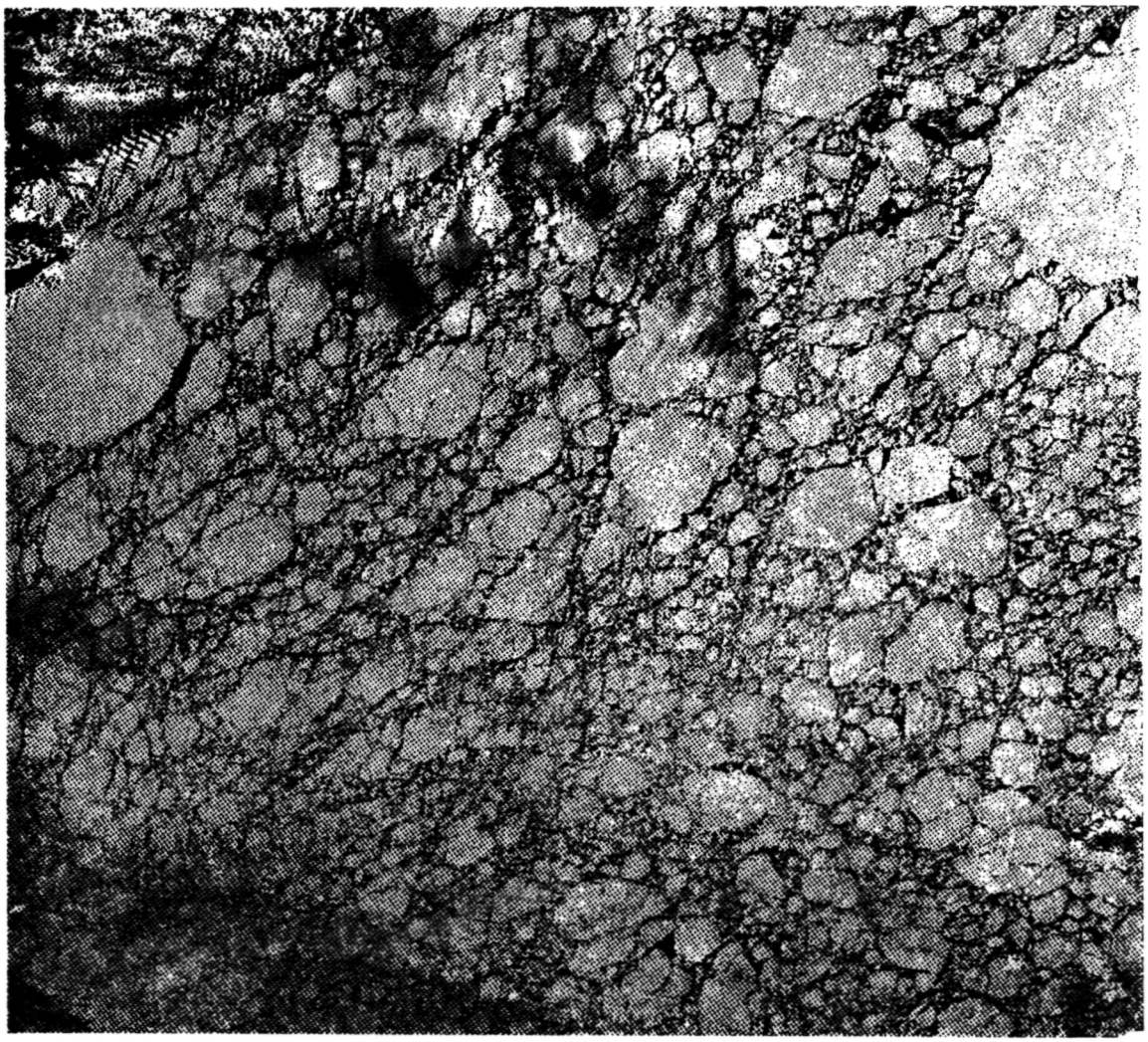

Figure 8 Brightness temperatures 19 GHz and 37 GHz for the Weddell Sea on November 29, 1987. Note clusters for open Water and first-year ice.

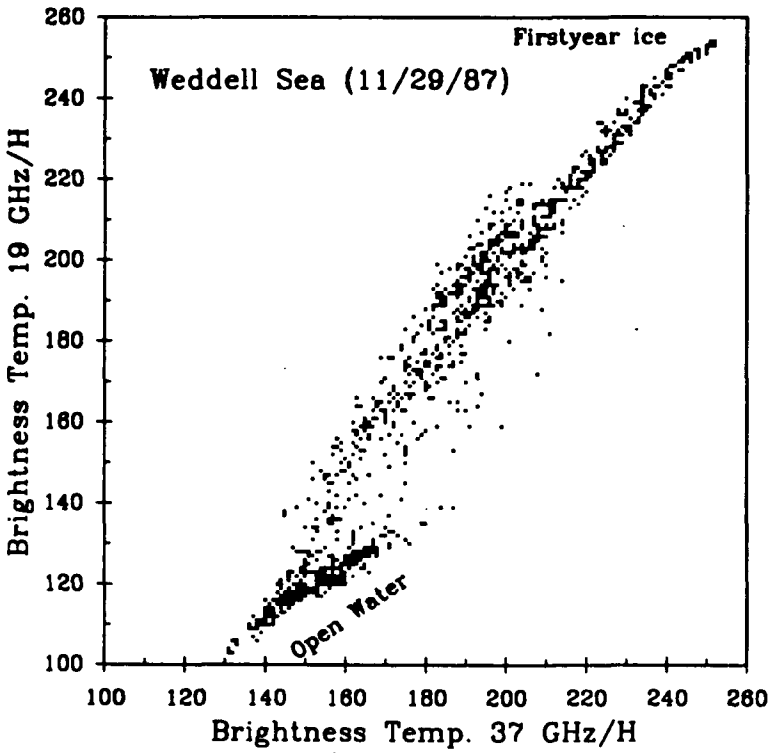

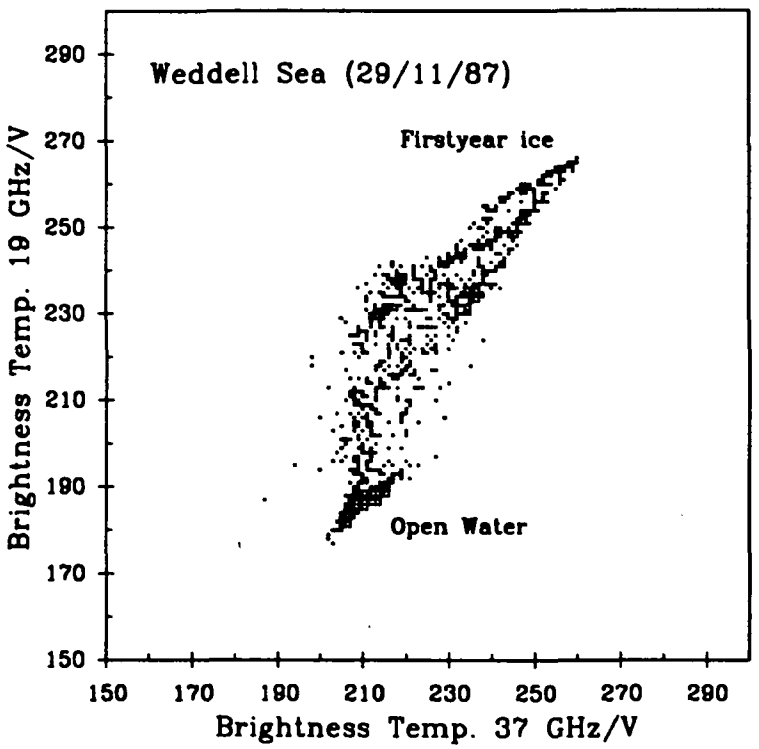

Figure 9 Ice concentration derived from Landsat image based on tie-point method (see Chapt. 3.1) versus SSM/I derived ice concentration for each 25 x 25 km grid cell in the Weddell Sea on November 29, 1987. The standard deviation of the error (Landsat minus SSM/I ice concentration) is 2.15 %.

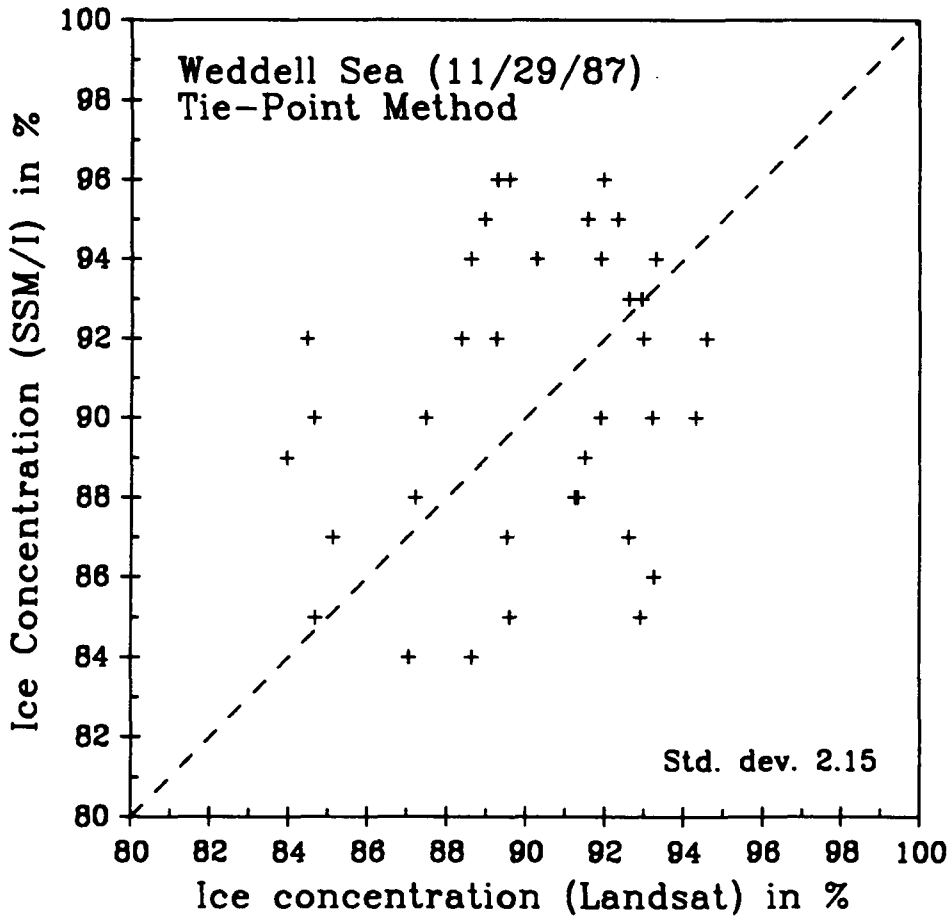

Figure 10 Ice concentration derived from Landsat image based on threshold method (white ice and open water only, see Chapt. 3.1) versus SSM/I derived ice concentration for each 25 x 25 km grid cell in the Weddell Sea on November 29, 1987. The standard deviation of the error (Landsat minus SSM/I ice concentration) is 4.25 %.

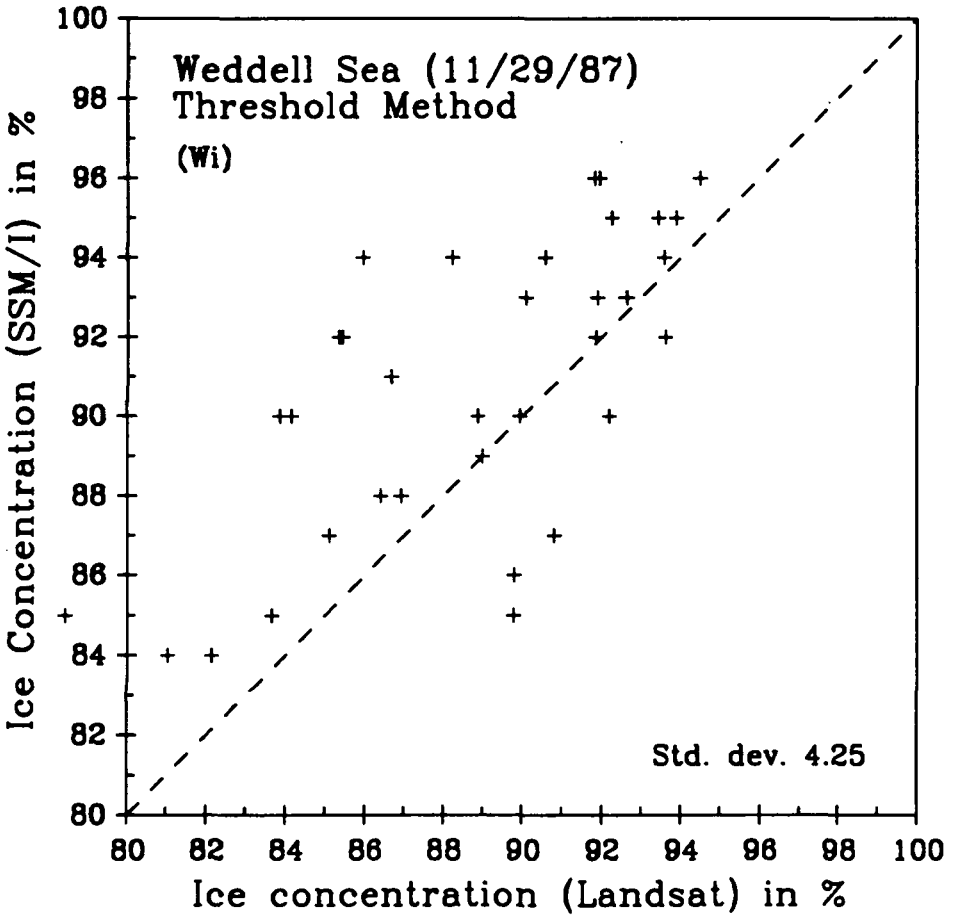

Figure 11 Ice concentration derived from Landsat image based on threshold method (white ice, open water and ice/water mixtures, see Chapt. 3.1) versus SSM/I derived ice concentration for each 25 x 25 km grid cell in the Weddell Sea on November 29, 1987. The standard deviation of the error (Landsat minus SSM/I ice concentration) is 3.11 %.

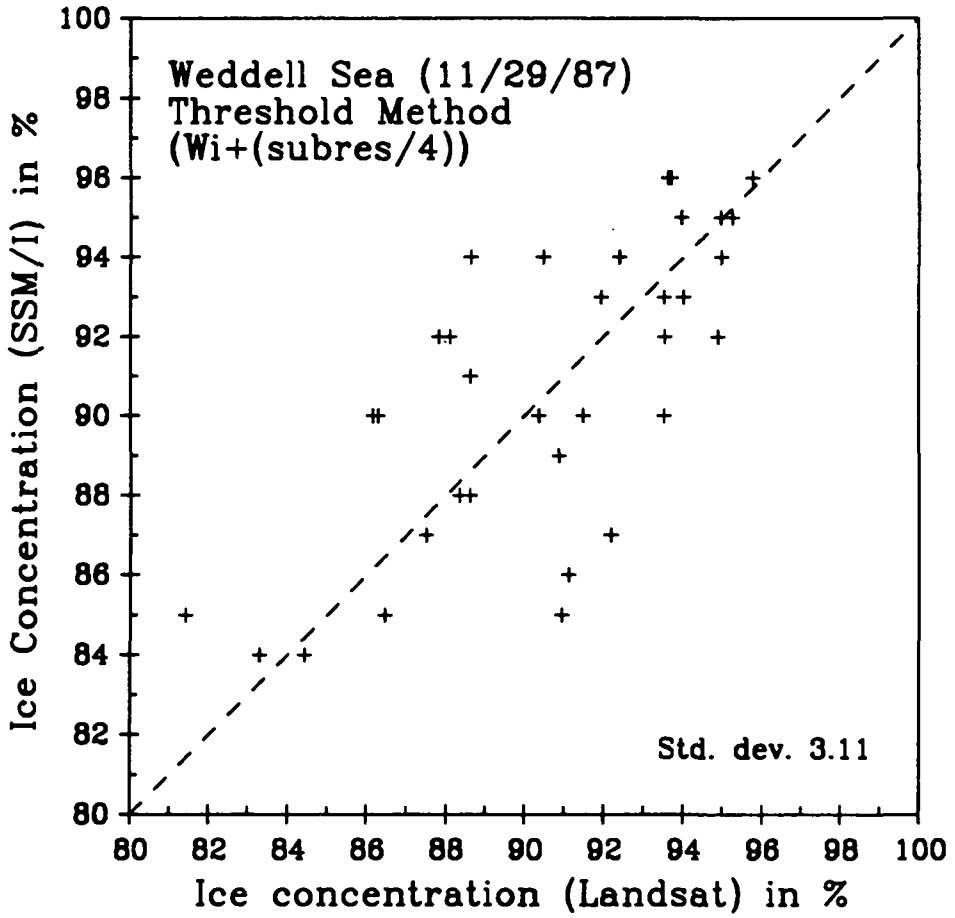

3.4 Orbit corrections for SSM/I

During the SSM/I validation meeting at NASA/GSFC (April 19, 88), Steffen had agreed to check the orbit corrections derived by Calvin Swift which were based on small changes in pitch, yaw and roll angles.

The following method was used to test the collocation accuracy: The original swath data (Wentz tapes: Latitude, Longitude, TB's) were gridded for each consecutive orbit to the 25 x 25 km SSM/I grid. Only 37 GHz/V brightness temperatures were used for this analysis (vertical polarization less effected by surface winds than the horizontal polarization, 37 GHz smaller footprint then 19 GHz, 85 GHz affected by water vapor). A second data set was generated with slightly different lat/long coordinates based on small changes in pitch, yaw and roll angle (program for this orbit correction was supplied by C. Swift).

For selected areas with large brightness temperature contrast (land - water), the 37 GHZ/V brightness temperature from two consecutive orbits covering the same area were compared for individual grid cells. The correlation coefficient of the two data sets (37 GHz/V from orbit 1 versus 37 GHz/V from orbit 2) was calculated. Brightness temperature differences of -7 to +3 K between the two orbits are related to actual changes in environmental conditions and, therefore, considered noise in the geolocation correction procedure and not included in the analysis (see bottom line of Table 2: total number of TB's and number of TB's used for for computation). The results are listed in Table 2 for the two areas Beaufort Sea (Julian Day 192, 193,194) and Bering Sea (JD 195, 203) of 1987. The correlation coefficient for the original data (uncorrected orbit) varied between 0.85 to 0.88. With Swift's corrections for pitch, yaw and roll, the coefficient increased about 7% (0.91-0.97).

During this analysis, numerous data sets were generated with varying pitch, yaw and roll angles. This study confirmed, that the orbit corrections derived by Swift show the correct sign for pitch (negative) and for yaw (positive), however, a better correlation was found (0.94 - 0.98) with smaller values (see Table 2) for latitudes north of 70 (Swift's values were derived for latitudes between 21 S and 52 N, averaged over three days). A latitude dependence of pitch and yaw angles was assumed and studied in more detail.

Through minimization of the SSM/I inter-orbit brightness temperature differences, a linear latitude dependence of the orbit correction angles for the northern hemisphere was found. The southern hemisphere seems to be a mirror image, however, the statistics are less significant because of fewer data points. Further computations by Mark Goodberlet, UMASS in association with Calvin Swift based on the island data set confirmed this latitudinal dependence. The mean monthly coefficients for the linear correction of pitch, yaw and roll angle are listed in Table 3 for July to October 1987. Mark agreed to compute the coefficients for a three day mean upon request.

Pitch angle

The latitude dependence of the pitch angle shows good agreement with the linear model (correlation coefficients 0.63 to 0.79, see Table 3). Case studies for a four day time period in the Beaufort Sea (Sept. 16 - 19, 1987), comparing consecutive orbits for best collocation fit, showed that the pitch angle can differ up to 30% from the linear model. In general, however, deviations from the linear model are small (<10%). Therefore, it is recommend that the pitch values derived by Swift's group be used with linear latitude corrections for both hemispheres (see Table 3).

Yaw angle

Yaw angle corrections are less well correlated with latitude using a linear model (see Table 3). Best orbit corrections were

achieved for selected case studies using the same angle for yaw as was derived for pitch, however with different signs (pitch negative, yaw positive). For the time being my suggestion would be to use the same angle for pitch and yaw corrections (different signs, pitch corrected for latitude dependence). We will work on other solutions to get this random yaw deviation under control.

Roll angle

Due to the fact that the roll angle is less than 0.1^0, I suggest to neglect this correction.

The orbit corrections have been checked for different polar regions (Beaufort Sea, Bering Sea, Greenland Sea and Weddell Sea). No longitude dependence of pitch and yaw angle corrections has been found. Only one comparison was carried out for the Antarctic region (Weddell Sea, November 29, 1987), where best agreement between two consecutive orbits was found for zero pitch and yaw angles. This collocation comparison was done with digital Landsat MMS data (navigation accuracy better than 200 m).

The mean monthly pitch and yaw correction angles are decreasing from July to September 1987 (Table 3); future analysis will reveal the mean correction for the remaining two months of 1987 (hopefully close to zero).

A method has been developed using scatter plots of TB differences from uncorrected versus corrected orbits which allows to tune pitch and yaw angle for best fit (Fig. 12, 13). This method, however, uses a considerable amount of computation time, and therefore, could not be used in an operational mode. For case studies such as validation of SSM/I data with Landsat imagery, or during the DC-8 flight period, this effort would be worth while.

In future the following problems will be addressed:

- sensitivity study of derived ice concentration due to pitch and yaw
- comparison of AVHRR (provided by Molly McElroy) with SSM/I for geolocation

Table 2: Correlation coefficient of 37 GHz/V brightness temperature for two consecutive orbits over the same area. The orbit corrections (pitch, yaw and roll) were applied to the original swath data (Wentz-tapes).
Julian Days 192, 193, 194: Beaufort Sea
Julian Days 195, 203 : Bering Sea

Julian Day -->	192	193	194	195	203
Uncorrected orbit Corr. Coeff.	0.85	0.87	0.88	0.88	0.87
Swift cor. applied Corr. Coeff.	0.92	0.91	0.93	0.97	0.92
pitch	-0.8	-0.8	-0.8	-0.7	-0.64
yaw	0.58	0.52	0.55	0.58	0.4
roll	-0.16	-0.2	-0.15	-0.13	0.0
Steffen cor. applied Corr. Coeff.	0.95	0.94	0.95	0.98	0.94
pitch	-0.6	-0.6	-0.6	-0.6	-0.6
yaw	0.6	0.6	0.5	0.6	0.6
roll	0.0	0.0	0.0	0.0	0.0
Pixels for comput. of corr. coeff.	46	110	160	41	40
Total pixels	702	891	1040	149	144

Table 3: Frequency of 37 GHz/V brightness temperature difference for two consecutive orbits on Julian Day 192 (7/11/88) for the Beaufort Sea.

uncorrected orbit

VALUE	FREQ	VALUE	FREQ	VALUE	FREQ
-27.00	1	-8.00	3	2.00	16
-23.00	1	-7.00	6	3.00	6
-22.00	1	-6.00	12	4.0	2
-19.00	1	-5.00	23	5.00	5
-18.00	2	-4.00	45	6.00	4
-16.00	1	-3.00	100	7.00	2
-12.00	2	-2.00	167	8.00	2
-11.00	2	-1.00	147	9.00	2
-10.00	2	-0.00	87	12.00	1
-9.00	2	1.00	56	14.00	1

Swift orbit cor: pitch=-0.8, yaw=0.58, roll=-0.16

VALUE	FREQ	VALUE	FREQ	VALUE	FREQ
-34.00	1	-7.00	7	4.00	4
-30.00	1	-6.00	5	5.00	2
-26.00	1	-5.00	15	6.00	4
-16.00	1	-4.00	29	7.00	2
-15.00	1	-3.00	91	8.00	1
-13.00	3	-2.00	158	9.00	1
-12.00	3	-1.00	160	10.00	2
-11.00	2	-0.00	127	11.00	2
-10.00	1	1.00	50	12.00	1
-9.00	2	2.00	18		
-8.00	2	3.00	5		

Steffen orbit cor: pitch=-0.6, yaw=0.6, roll=-0.0

VALUE	FREQ	VALUE	FREQ	VALUE	FREQ
-22.00	2	-6.00	8	3.00	6
-18.00	1	-5.00	17	4.00	6
-16.00	1	-4.00	30	5.00	5
-15.00	1	-3.00	96	6.00	3
-12.00	2	-2.00	174	7.00	3
-10.00	2	-1.00	164	8.00	1
-9.00	5	1.00	70	10.00	1
-7.00	6	2.00	15	12.00	1

Table 3: Geolocation correction for SSM/I data using Swift's pitch yaw and roll angles, and applying corrections for latitude dependence (July to October 1987).

P = a * L + b, P = pitch angle in deg.
Y = a * L + b, Y = yaw angle in degrees
R = a * L + b, R= roll angle in degrees
L = latitude in degrees (0-90)

Note: coefficients a and b are different for P, Y and R.

Month	a	b	R	linear Model val. for 75^0 N	suggested values for 75^0 N
JULY					
P	+0.0039	-0.79	+0.75	-0.5	-0.5
Y	-0.0057	+0.58	-0.75	+0.16	+0.5
R	+0.0042	-0.17	+0.53	+0.15	+0.0
August					
P	+0.0036	-0.67	+0.63	-0.4	-0.4
Y	-0.0065	+0.70	-0.64	+0.21	+0.4
R	+0.0061	-0.28	+0.73	+0.18	+0.0
September					
P	+0.0035	-0.69	+0.79	-0.43	-0.43
Y	-0.0016	+0.54	-0.34	+0.42	+0.43
R	+0.0012	-0.15	+0.27	-0.06	+0.0
October					
P	+0.0033	-0.57	+0.75	-0.33	-0.33
Y	-0.0031	+0.61	-0.29	+0.38	+0.33
R	+0.0038	-0.26	+0.36	+0.03	+0.0

Figure 12 Plot of 37 GHz/V brightness temperature difference for two consecutive orbits for corrected and uncorrected pitch, yaw and roll on Julian Day 192, 1987 (7/11/88) for the Beaufort Sea. The upper graph show the Swift correction, the lower graph shows our corrections (for correlation coefficients see Table 2).

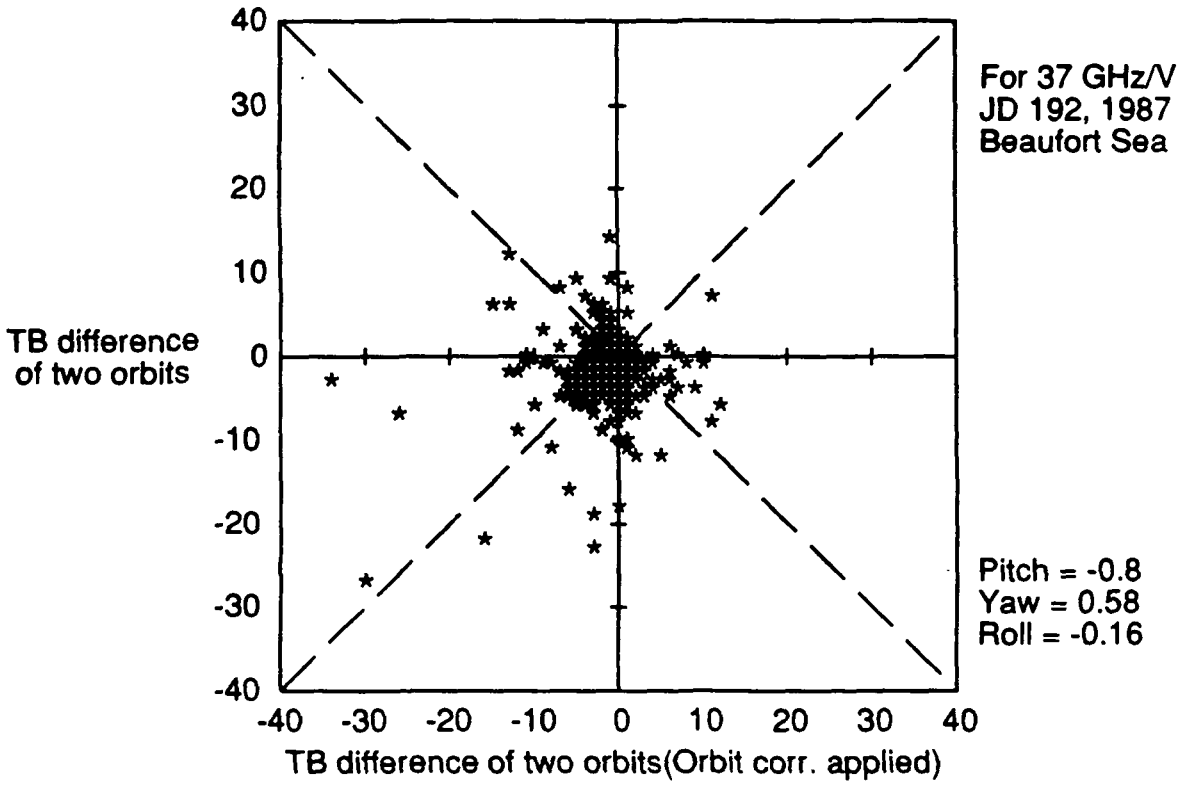

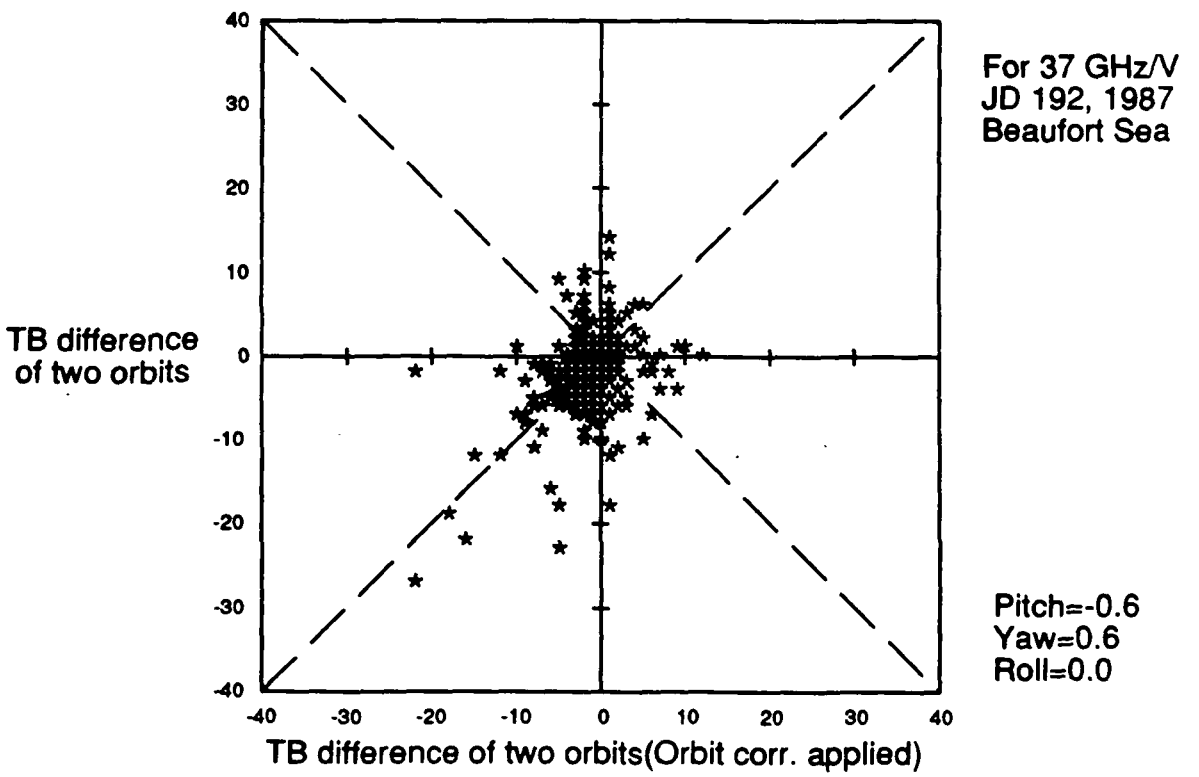

Figure 13 Plot of 37 GHz/V brightness temperature difference for two consecutive orbits for corrected and uncorrected pitch, yaw and roll on Julian Day 195, 1987 (7/14/88) for the Bering Sea. The upper graph show the Swift correction, the lower graph shows our corrections (for correlation coefficients see Table 2).

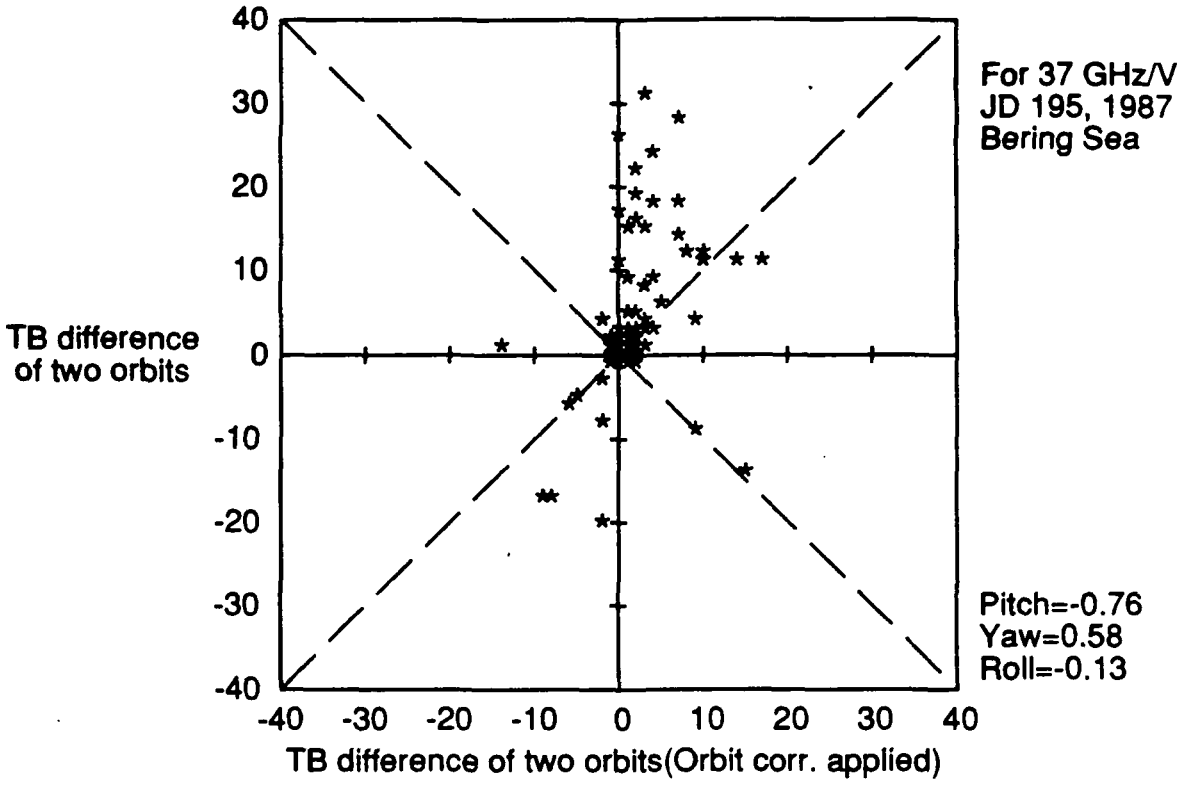

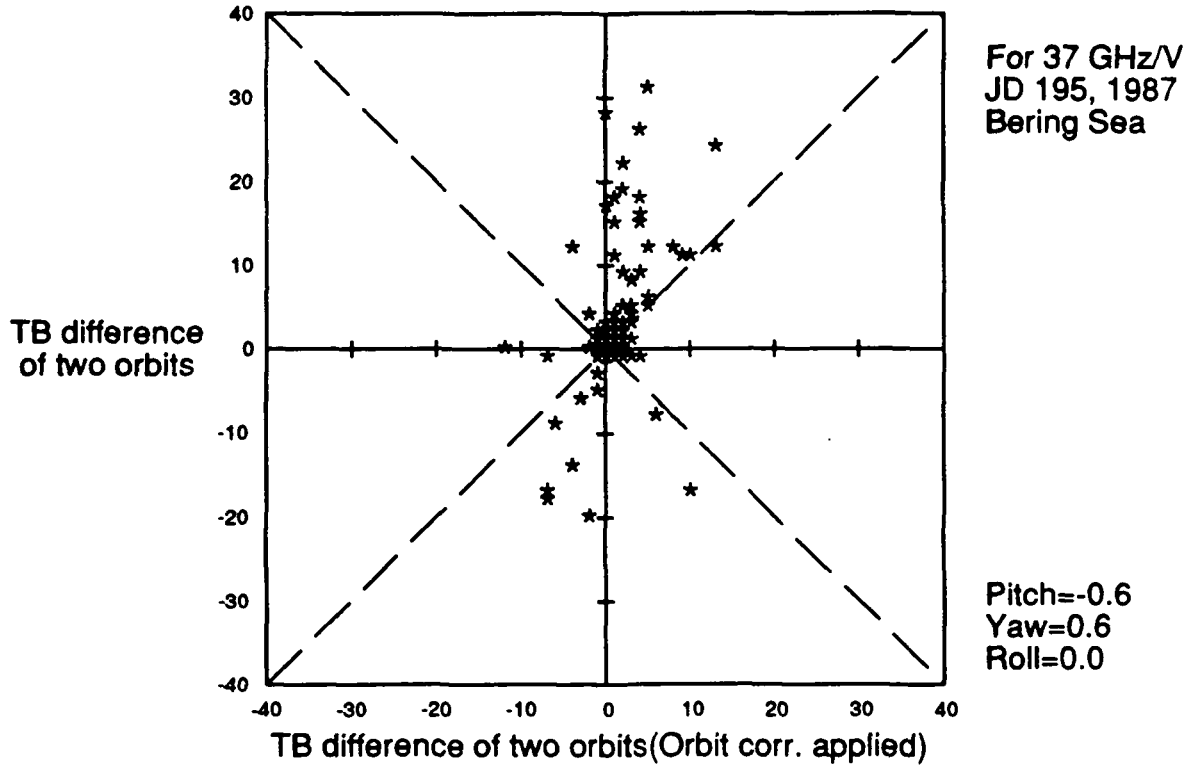

4. Development of software

The following computer software has been developed:

1. Extraction of SMMR data from cell-all format tapes on VAX computer by latitude and longitude and converting to the polar stereographic format planned for DMSP SSM/I. The data can be mapped to grid cells of different sizes to study the fact that 67% of the power received by the radiometer lies outside the field-of-view (FOV).

2. Extraction of SSM/I data from Wentz tapes on VAX computer by latitude and longitude with same option than mentioned in (1).

3. Transformation of Landsat data to polar stereographic projection on VAX computer.

4. Derivation of sea ice parameters (e.g. NASA Team algorithm for ice concentration, ice edge, multi-year ice concentration) from the brightness temperatures of the orbital swath data. In view of the rapidity of the ice concentration fluctuation, the orbital data will be remapped to coincide more closely in time with the Landsat data.

5. Program for cross-correlation of data fields from different satellite sensors (Landsat, AVHRR, SMMR, SSM/I). The satellite data can be transformed to polar stereographic projection and for each grid cell the corresponding sea ice parameter can be compared.

6. Ice type and concentration classification for Landsat images (for details see chapter 3.1).

7. Image display and analysis system for SSM/I, SMMR and AVHRR data on a personal computer (class AT with enhanced graphic system). The following features can be displayed:

   Brightness temperatures 19, 37, 85 GHz in both polarizations

   Histogram for all TB's with MIN and MAX calculated interactively

   Ice concentration based on SSM/I validation algorithm

   Difference in TB of two consecutive orbits

   Difference of Ice concentration of two consecutive orbits

   All the ice products were derived from SSM/I Wentz tapes or SMMR CELL ALL tapes. Further, the image can be evaluated using existing statistical programs (SPSSPC).

5. Future work

1. The main objective of the future work is the comparison of Landsat, AVHRR and SSM/I derived ice products for the windows defined in chapter 2. Further, the seasonal change of compact pack ice, open water and old ice brightness temperatures used as tie-points for ice concentration calculation will be carried out for different polar regions (Arctic as well as Antarctic).

2. The orbit correction procedure will be carried on for the remaining two months of 1987, and if necessary also for 1988. A major effort will be focussed on the irregular change of the yaw angle (see Chap. 3.4) and predictive models will be developed if rational.

3. Classification of Landsat and AVHRR images currently requires a substantial amount of manual interpretation due to the similar spectral signature of ice and clouds as well as due to the presence of cloud shadows. Classification methods employing the analysis of shape, texture and context could possibly be developed for a further automation of the ice classification procedure. While of limited merit for the current validation effort, research into the development of an expert system for the ice/cloud discrimination could produce valuable results for future studies involving large data sets of high resolution imagery (ISCCP,EOS, ERS-1, Radarsat). Under a seperate project (NAG-5-898), the problem of cloud/ice discrimination is being examined (Key et al., submitted).

6. References

Comiso, J.C., and H.J. Zwally., Antarctic sea ice concentration inferred from Nimbus 5 ESMR and Landsat imagery, Journ. of Geophys. Res., 87(8), 5836-5844, 1982.

Ito, H., Sea ice atlas of northern Baffin Bay, Zurcher Geogr. Schr., 7, 142 pp, 1982.

Key, J.R., Maslanik, J.A., and Barry, R.G., Classification from satellite data using fuzzy sets algorithms: a polar example, Int. J. Rem. Sens. (submitted).

Snyder, J.P., The Space Oblique Mercator Projection. Photogrammetric Engineering and Remote Sensing, 44(5), 585-596, 1978.

Steffen, K., and Maslanik, J., Comparison of Nimbus 7 SMMR microwave and derived sea ice concentrations with Landsat imagery for the North Water area of Baffin Bay, Jour. of Geophys. Res., (accepted for publication), 1988.

Appendix A: Landsat images for intercomparison with DMSP-SSM/I

Window	Date/Path/Row	Area
L1A	87-09-17/75/9,10	Beaufort Sea
L1B	87-11-10/77/9,10	Beaufort Sea
L2	88-11-29/195/112	Weddell Sea (Antarct.)
L3A	88-03-12/74/6,7,8	Beaufort Sea Transact
L3B	88-03-16/70/9,10	Beaufort Sea Ice Station
L3C	88-03-19/75/9,10	Beaufort Sea Mosaic
L3D	88-03-25/77/8	Beaufort Sea
L4	88-03-08/78/15	Norton Sound (Bering Sea)
L5A	88-03-13/81/15,16,17,18,19	Bering Sea
L5B	88-03-21/89/15,16,17	Bering Sea (Soviet side)
L5C	88-04-14/81/16,17,18,19	Bering Sea
L6	ordered for June	Northern Baffin Bay
L7	ordered for June	Barents Sea
L8	ordered for June	Greenland Sea

Appendix A: Landsat images in support of NASA DC-8 flight mission

Window	Date/Path/Row	Area
L3A	88-03-12/74/6,7,8	Beaufort Sea Transact
L3B	88-03-16/70/9,10	Beaufort Sea Ice Station
L3C	88-03-19/75/9,10	Beaufort Sea Mosaic
L4	88-03-08/78/15	Norton Sound (Bering Sea)
L5A	88-03-13/81/15,16,17,18,19	Bering Sea

Appendix A: Coordinate for Landsat images used in case studies

Window	Center coordinate	Ice conditions
L1A1	72.15 N/ 147.09 W	IC(20%), SY MY, FS 80m - 40km
L1A2	70.86 N/ 149.25 W	IC(2%), SY MY, FS 80m - 10km
L1B1	72.18 N/ 150.28 W	IC(90%), MY(50%) YI(40%), FS 2-50km
L1B2	70.90 N/ 152.44 W	IC(98%), MY(30%) YI(68%), FS 2-5km
L2	73.27 S/ 038.37 W	IC(85%), FS 80m-10km
L3A1	75.89 N/ 137.16 W	IC(97%), FY MY, large fracture pattern
L3A2	74.69 N/ 140.45 W	tito
L3A3	73.46 N/ 143.28 W	tito
L3B1	72.19 N/ 139.56 W	IC(95%), FY MY, large fracture pattern
L3B2	70.90 N/ 141.71 W	tito
L3C1	72.19 N/ 147.29 W	IC(98%), FY MY, some fractures
L3C2	70.90 N/ 147.29 W	IC(87%), coastal fractures (polynya)
L3D	73.45 N/ 147.75 W	IC(95%), large fracture pattern
L4	64.22 N/ 161.77 W	IC(70%), NI(15%) YI(20%) FY(60%)
L5A1	64.22 N/ 166.41 W	IC(95%), NI(20%) YI(35%) FY(35%)
L5A2	62.85 N/ 167.54 W	IC(95%), NI(10%) YI(10%) FY(75%)
L5A3	61.47 N/ 168.59 W	IC(90%), YI(10%), FY(80%)
L5A4	60.09 N/ 169.55 W	IC(75%), FS 2-60m
L5A5	58.70 N/ 170.44 W	IC(50%), FS 2-60km, ice edge
L5B1	64.21 N/ 178.78 W	IC(95%), YI(60%) FY(35%), FS 80m-20km
L5B2	62.84 N/ 179.71 W	IC(85%), YI(15%) FY(70%), FS 80m-8km
L5B3	61.47 N/ 179.05 W	IC(60%), YI(40%) FY(20%), ice edge
L5C1	62.82 N/ 167.58 W	IC(75%), YI(10%) FY(65%), FS 80m-15km
L5C2	61.45 N/ 168.62 W	IC(75%), YI(15%) FY(60%), FS 80m-20km
L5C3	60.06 N/ 169.58 W	IC(80%), lots of clouds
L5C4	58.67 N/ 170.47 W	IC(80%), lots of clouds

Ice Nomenclature

NI	new ice	YI	young ice
FY	first-year ice	SY	Second-year ice
MY	Multi-year ice	FS	floe size

Appendix A: Alaskan Quicklook System Landsat Images

Landsat MSS images were acquired through the Alaskan Quicklook system facility at Gilmore Creek. Digital imagery for this area is not available since the communication satellite (TDRS) serving as a downlink does not provide coverage for this area.

The images originate from the MSS sensors on board of Landsat - 4 and 5 with a resolution of 80 m. Each image represents a WRS (World Reference System) scene with a width of 188.5 km and a height of 156.5 km (Sizes refers to actual image data). WRS coordinates (Path, Row) for the scene are given below the image as the 2 first items in the second annotation line. (e.g. P74 R7).

Actual image center coordinates in Longitude Latitude are given in the third annotation line (First 2 items). Image center coordinates refer to the center of the central scanline and are calculated from the ephemeris data of the previous over-path.

Images are geometrically corrected for scan geometry and earth rotation and displayed in a (SOM) Space oblique Mercator Projection. Due to the nature of the SOM projection scan lines are skewed from the vertical axis of the SOM coordinate system by a small angle (ca 1 Deg. in higher latitudes). (see Snyder, 1978).

Images are received on the descending nodes of the Landsat orbit so that the top of the image is on the poleward side of a particular path. Images with identical path numbers and adjacent row numbers are adjacent with increasing row numbers along the path as it approaches the equator.

Annotation records further contain information on Spacecraft (Landsat-4 or 5), spectral band, date of acquisition (third item, second annotation line), Sun elevation and azimuth (third item in third annotation line) and type of contrast stretch applied to the

image. (First item 4 th. record). Acquisition date (Julian date) and time (Greenwich mean time).

NOTE : The scale given on the images refer to the original transparencies. Copies are reduced sizes.

Landsat 5 Image of the Beaufort Sea (Quicklook)

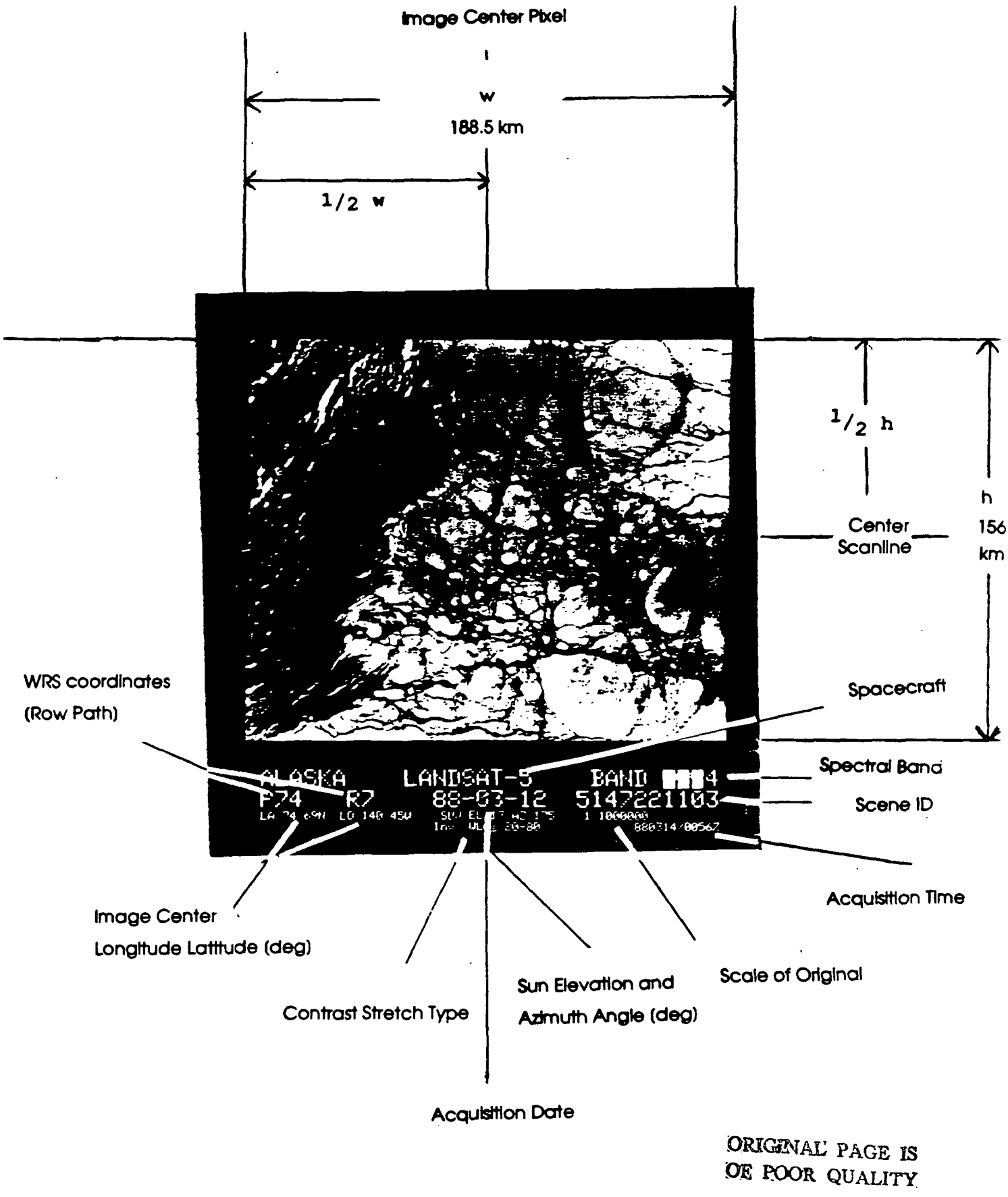

Appendix B: Abstract presented at International Union of Geodesy and Geophysics (IUGG), XIX General Assembly, Vancouver, August 9, 1987.

MICROWAVE OBSERVATION OF THE NORTH WATER POLYNYA

Steffen, K. and Maslanik, J., Cooperative Institute for Research in Environmental Sciences, University of Colorado, Boulder CO 80309, U.S.A.

The radiative characteristics of the ice cover in Northern Baffin Bay is studied using multichannel, dual-polarized satellite microwave data in conjunction with in situ low level airborne infrared thermometry and ground observations during the winters 1978/79 and 1980/81.

The North Water area is well suited for a microwave study of thin ice due to its large and homogeneous open water/ice mixture, new ice and young ice regions throughout the winter. Based on the low level infrared thermometry, the following ice types were classified: white ice/first year ice, young ice/new ice, open water/ice mixture. The classified ice types were compared with the brightness temperatures obtained from the Nimbus-7 Scanning Multichannel Microwave Radiometer (SMMR) at three frequencies (18, 21, 37 GHz) and two polarizations. Best correlation was found with the polarization ratio of 18 GHz. With the 37 GHz channel the ice classification gave a poor correlation compared to ground truth data. The 18 GHz channel is superior to 37 GHz for thin ice classification due to the frequency dependence of the penetration depth. For saline ice, the optical depth is in the order of the wavelength of the radiation. The ice type classification based on the 18 GHz polarization ratio will also be compared with the classification based on microwave emissivity and physical temperature.

Ice concentrations calculated using the operational Goddard sea ice algorithm were compared with known ice conditions in the North Water area, and with ice charts and satellite imagery for other areas (e.g. Hudson Bay). Preliminary results confirm that the ambiguity between the polarization of thin ice and open water

causes the Goddard algorithm to significantly underestimate ice concentration in areas with a uniformly high amount of thin ice types. Selection of different brightness temperature tie points improves ice retrieval, but requires a priori knowledge of ice conditions.

The 18 GHz polarization ratio was used to monitor the frequency of northerly storms in Smith Sound and Northern Baffin Bay. The storms cause an ice divergence in Smith Sound with open water/ice mixture covering most of the Sound after the storm system has passed. The mean storm frequency of 14 days throughout winter, based on microwave data analysis, is a new finding and gives further evidence that winds are the driving force of upwelling, believed to be the major cause of the polynyas in the North Water.

Appendix B: Abstract presented at the American Geophysical Union (AGU), New Orleans, January 20, 1988.

Comparison of Geophysical Sea Ice Parameters Derived from Passive Microwave Data and Landsat Imagery

KONRAD STEFFEN and J. A. MASLANIK (Cooperative Institute for Research in Environmental Sciences, University of Colorado, Boulder, CO 80309)

Satellite passive microwave data from satellite are essential for long term monitoring of sea ice cover due to the study of climate fluctuations. In order to detect changes in the ice cover, the accuracy with which geophysical sea ice parameters are retrieved from satellite passive microwave data have to be known.

Sea ice parameters derived from Scanning Multichannel Microwave Radiometer (SMMR) data are compared with ice types and concentrations interpreted using Landsat imagery and surface measurements for pre-melt and melt periods in the North Water area of Baffin Bay during 1981. The spatial and temporal distribution of microwave brightness temperatures, gradient ratios, and polarization ratios are studied for first-year pack ice and first-year fast ice areas.

Brightness temperatures and ratios for areas identified as young ice and nilas in the Landsat interpretation show a strong linear relationship between polarization ratio and ice thickness. The same relationship is found to hold for polarization ratio and modelled sensible heat flux. Ice concentrations are calculated using three versions of SMMR-based sea ice algorithms, and are compared with Landsat-derived concentrations. Differences between multispectral SMMR and Landsat-derived concentrations are within 3.5% for pre-melt and melt onset periods. During melt, differences increase to about 10%. Maximum differences for individual locations are greater, and contribute to a mean correlation of 0.53 between SMMR and Landsat-derived concentrations. The SMMR data yield slightly lower estimates of total ice concentration, and

tends to underestimate high concentrations and overestimate low concentrations relative to the Landsat interpretation. Due to the negative gradient ratios observed over fast ice, and over all ice types during melt, the SMMR algorithm overestimated the concentration of old ice.

Appendix D

Sea Ice Distribution Derived from Passive Microwave Data for the North Water in Winter

Konrad Steffen+
Cooperative Institute for Research in Environmental Sciences
University of Colorado at Boulder
Boulder, CO 80309

Conference-Seminar by IMTEC
Montreal, October 16 and 17, 1987
Polynyas with special reference to the North Water

+ On leave from Dept. of Geography, Swiss Federal Institute of Technology, Zurich, Switzerland

1. Introduction

The North Water is situated in the North American Arctic between Greenland on the east and the Canadian Islands Ellesmere and Devon on the west (Fig. 1). In this region the sea surface does not show a homogeneous ice cover during winter and spring months as one might expect from the climate conditions in such northern latitudes. On the contrary, an area of loose pack ice is found, formed by the three boundary polynyas of Smith Sound, Lady Ann Strait and Lancaster Sound/Barrow Strait (Steffen, 1985). The polynyas occur every year in the same place (recurring polynyas). To the north in the narrowest point between Greenland and Canada, 79° N, the area is bounded by a fast-ice arch. The southern boundary cannot be clearly defined as the pack ice in the North Water is constantly drifting southward. For the past two decades, the North Water has drawn scientific attention from the field of glaciology, climatology, oceanography, and biology (Franceschetti et al., 1964; Dunbar, 1969; Nut, 1969; Muench, 1971; Finley and Renaud, 1980; Dunbar, 1981). The center of the problem is the unusual ice conditions for which the region has been known since William Baffin's voyage in 1616. The actual North Water covers an area of approximately 80,000 km^2 (Fig. 1) which is dominated by close pack ice (ice concentration 7/10 to 8/10) with many leads and polynyas (located in Lancaster Sound, Barrow Strait, Smith Sound, and Lady Ann Strait) throughout winter.

This paper discusses in detail the ice-type distribution of the North Water area during winter. The analysis is based on passive microwave measurements of the Special Multichannel Microwave Radiometer (SMMR) onboard the Nimbus 7 satellite. The ability of SMMR to acquire imagery of the earth's surface in most weather and under all lightning conditions makes SMMR particular useful for sea ice studies in polar regions. SMMR data have been used for many years to monitor sea ice in polar regions (Zwally et al., 1983; Parkinson et al., 1987) with major applications in ice concentrations studies of first-year ice and multi-year ice, and in determining the position of the ice edge (Cavalieri, et al., 1984).

In this study, for the first time, passive microwave data is used to distinguish between different first-year ice types such as white ice (WI), grey ice/grey-white ice (GI), nilas (NI) and open water (OW). As by definition a polynya may contain brash ice and/or be covered with new ice, nilas or young ice (World Meteorological Organization, 1970). Therefore, the distinction between different first-year ice types is essential for monitoring the ice cover of a polynya, as the ice cover of a polynya. The SMMR collects data in five channels (6.6 GHz, 10.7 GHz, 18 GHz, 21 GHz, and 37 GHz), with two polarizations, however, in this work only the 37 GHz channel was used with a pixel size of 30 km x 30 km. Due to power limitation on board Nimbus 7, the SMMR

operates on alternate days, and a complete coverage of the North Water area is available every other day. Despite the large SMMR pixel, the passive microwave data is the only all year/all weather aerial information of the sea surface in the North Water area.

The study area for which the ice type classification was carried out is delineated by longitude 70° and 80° W and parallels 72° N and 80° N. The ocean surface in this area comprises approximately 100,000 km^2. The SMMR analysis was carried out for the same winters during which the North Water Winter Remote Sensing Project took place (1978/79 and 1980/81) (Steffen, 1986).

2. Method

The accuracy with which sea ice parameters can be derived from SMMR data has been studied in detail for the North Water area (Steffen and Maslanik, submitted). In that validation study the sea ice parameters derived from SMMR data were compared with ice types and concentrations interpreted using Landsat imagery and surface measurements during winter and spring of 1980/81. That study showed, that for the three ice types WI, GI and NI, the polarization ratio (PR) at 18 and 37 GHz increases with decreasing ice thickness (Fig. 2). Similar results were reported for airborne passive microwave measurements (Cavalieri et al., 1986), and for ground based measurements (Grenfell, 1986).

The polarization ratio is defined as

$$PR_{fq} = (T_B(V,fq) - T_B(H,fq))) / (T_B(V,fq) + (T_B(H,fq))$$

where PR_{fq} is the polarization ratio at frequency fq, $T_B(V,fq)$ and $T_B(H,fq)$ an observed brightness temperature at frequency fq and vertical or horizontal polarization. The SMMR data used in this study consists of data that had been converted from CELL-ALL format to a polar stereographic projection corresponding to the format planned for the Special Sensor Microwave Imager (SSM/I). Tapes containing these data are archived at the National Snow and Ice Data Center (NSIDC) at Boulder, Colorado.

Based on the relation of increasing polarization ratio with decreasing ice thickness (Fig. 2), a threshold technique was applied to classify the different ice types. For the ice typing presented in this paper the following PR values were used:

$$OW > 0.08$$
$$0.08 > NI > 0.05$$
$$0.05 > GI > 0.03$$
$$0.03 > WI$$

where OW is open water, NI is nilas (ice between 0 - 0.1 m in thickness), GI is grey ice and grey-white ice (ice between 0.1 - 0.3 m in thickness), and WI is white ice (ice thicker than 0.3 m). Ice type classification by means of PR seems possible for large homogeneous ice areas consisting of a single ice type. In nature however, and for the ice cover of polynyas in particular, young ice like nilas and grey ice seldom completely covers areas of 30 km x 30 km (one 37 GHz

SMMR pixel). To address this problem, the polarization ratio of mixed-ice SMMR pixels was analyzed (Steffen and Maslanik, submitted). The PR values of white ice/grey ice (WIGI), white ice/nilas (WINI), white ice/open water (WIOW) and grey ice/nilas (GINI) of which each ice type, e.g. WI and GI, covered 50% of the SMMR pixel are given in Figure 2. It is obvious that a clear distinction of ice types and ice type mixtures based on the PR method is not possible (e.g. grey ice and white ice/grey ice have almost the same signature, Fig. 2) and, therefore, the classified ice types have to be considered with care (e.g. the open water class could include also SMMR pixels consisting of 20% white ice and 80% open water).

3. Results and Discussion

The ice types were classified within the ocean surface of the study area (100,000 km^2) according the method described above for the months October to March of 1978/79 and 1980/81. Figure 3 dispicts the ice type percentages for white ice (WI), grey ice/grey-white ice (GI), nilas (NI) and open water (OW) on alternate days during winter 1978/79. In the lower part of Figure 3 the mean ice type percentages for each four weeks are given. The ice cover of the North Water shows major changes throughout winter. More than 70% white ice was present in early winter (JD 303-331), whereas young ice and open water made up almost 50% in November and December. For the remaining month January to March white ice was again the dominant ice type with up to 80% of the total ice cover. Only a few percent of open water were classified throughout the winter which is in good agreement with the low level aircraft measurements carried out during the same time period (Steffen, 1986).

During winter 1980/81 young ice and open water were dominant through October and part of November (Fig. 4). Considerable more open water was found compared to 1978/79, especially for the months January, February and March. The freeze up of the North Water ice cover was retarded by several weeks in fall 1980 which is well documented by this analysis. Again the "pulse-like" changes in the ice cover was dominant throughout the winter, a phenomenon which will be discussed in the following section.

The drastic changes of the ice cover over short time periods (e.g. JD 333 and 361, 1978 in Fig. 3) were analyzed in detail. Because the dielectric constant of ice and water is largely different, open water areas in the ice cover can be detected by their low brightness temperatures. Whenever a storm occurs the ice cover will break up resulting in a decrease of the brightness temperature in that area. Even small open water areas, subresolution to the SMMR pixel, will decreases the brightness temperature. Therefore, the brightness temperature of one SMMR pixel (37 GHz horizontal polarization) was plotted versus time for two different regions (Fig. 5). The first region lies within Smith Sound, close to Cape Alexander (Fig. 1). Because of frequent storms, the Cape Alexander area is reportedly the only place in this part of Greenland where the ice cover never freezes into a strong and persisting field (Steffen, 1986). The second area chosen for the brightness temperature comparison is located in the vicinity of the Carey Oer, in northern Baffin Bay (Fig. 1). The Cape Alexander pixel was used as an indicator of storm occurrences in the Smith Sound and the Carey Oer pixel is an indicator for the effect of the storms on the ice cover in the northern Baffin Bay; e.g. a brightness temperature decrease in both regions indicates that a major storm occurred over the North Water.

During the North Water Project wind measurements were carried out at Cape Sabine (close to Cape Herschel, western side of Smith Sound, Fig. 1) from November to March 1974 - 1977. They showed a predominant northerly component with a mean wind speed of 8.7 ms^{-1} from NNW in winter 1975/76 (Steffen, 1986). During this period 14 gales ($v>20$ ms^{-1}) from NNW were observed which lasted for a total of 270 hours with maximum wind speeds as high as 40 ms^{-1}. This record shows that the predominant wind direction in Smith Sound is from the north with frequent storms throughout the winter.

Based on the brightness temperature decrease in the two regions Cape Alexander and Carey Oer, three storm types were classified (Table 1): (a) major storm; TB decrease in both regions (b) storm; TB decrease in both regions but a minor one in the Carey Oer region (c) local storm: TB decrease in the Cape Alexander region only.

Table 1: Occurrence of storms in the North Water area during winter 1978/79. The storm types were classified according the brightness temperature decrease of SMMR 37 GHz in two specified areas (Cape Alexander and Carey Oer).

STORM TYPE	JULIAN DAY 1978	JULIAN DAY 1979
Major storm	335, 353	30
Storm	313, 317, 341, 345, 359	58, 70, 80
Local storm	305, 327	12, 24, 40, 46, 66

The storm pattern derived from the SMMR data were verified by the low level aircraft measurements during the same winter. On JD 12, 1979 a wind speed of 40 ms^{-1} was recorded along the flight profile in Smith Sound, and less then 5 ms^{-1} in the Carey Oer area. Figure 5 dispicts a large decrease for the Cape Alexander brightness temperature for that time period and no effect for the Carey Oer area. This storm which was of local nature in the Smith Sound show only a slight change in the North Water ice cover (Fig. 3). On the contrary, the two major storms on JD 335 and 353, 1978 (Fig. 5) had a large impact on the North Water ice cover (Fig. 3).

These northerly gales are known to be the prime cause of the polynyas in the North Water. During the North Water Winter Remote Sensing Project (1978/79 and 1980/81) patches of open water above freezing point were found in the area of the North Water (Steffen, 1985). They were located most frequently along the Greenland coast, in particular in the vicinity of Cape

Alexander. The existence of these warm water cells can be explained by the strong northerly winds resulting in a Coriolis force that induces ice divergence and coastal upwelling.

Acknowledgement

This work was supported by the Cooperative Institute for Research in Environmental Sciences (CIRES), University of Colorado at Boulder through a Visiting Fellow to the author. I also acknowledge the National Snow and Ice Data Center (NSIDC) at CIRES for providing the gridded SMMR data, and the SMMR Information Processing Team of the Nimbus Project and the National Space Science Data Center for providing the CELL ALL SMMR tapes.

References

Cavalieri, D. J., P. Gloersen, and W. J. Campell, Determination of sea ice parameters with Nimbus 7 SMMR, J. Geophy. Res. 89, 5355-5369, 1984.

Cavalieri, D. J., P. Gloerson, and T. T. Wilhelt, Aircraft and satellite passive microwave observations of the Bering sea ice cover during MIZEX West, IEEE Trans. Geosci. Remote Sensing, GE-24(3), 368-377, 1986.

Dunbar, M., The geographic position of the North Water, Arctic, 22(4), 439-441, 1969.

Dunbar, M., Physical causes and biological significance of polynyas and other open water in sea ice, in Stirling I., and Cleator, H., eds. Polynyas in the Canadian Arctic, Ottawa Wildlife Service, Occasional Paper No. 45, 29-40, 1981.

Franceschetti, A. P., D. A. McGill, N. Corwin, and E. Uchupi, Oceanographic observations, Kennedy Channel, Kane Basin, Smith Sound and Baffin Bay, summer 1963, Washington DC, United States Coast Guard (Oceanographic Report No. 5, 1964.

Grenfell, T. C., Surface-based passive microwave observations of sea ice in the Bering and Greenland Sea, IEEE Trans. Geosci. Remote Sensing, GE-24(3), 378-382, 1986.

Muench, R.D., The physical oceanography of the northern Baffin Bay region, Washington DC, Arctic Institute of North America. Baffin Bay-North Water Project (Scientific Report No. 1), 1971.

Nutt, D. C., The North Water of Baffin Bay, Polar Notes. Occasional publication of the Stefansson Collection, No. 9, 1-25, 1969.

Parkinson, C. L., J.C. Comiso, H. J. Zwally, D. J. Cavalieri, P Gloersen, and W.J. Campell, Arctic Sea Ice, 1973-1976: Satellite passive-microwave observations, NASA SP-489, 1987.

Steffen, K., Warm water cells in the North Water, northern Baffin Bay during winter, J. Geophy. Res., 90(C5), 9129-9136, 1985.

Steffen, K., Ice conditions of an arctic polynya: North Water in Winter, Jour. of Glaciology, 32(112), 383-390, 1986.

Steffen, K., and J. A. Maslanik, Comparison of geophysical sea ice parameters derived from passive microwave data and Landsat imagery for the North Water area of Baffin Bay, submitted to J. of Geophy. Res.

Zwally, H. J., J. C. Comiso, C. L. Parkinson, W. J. Campell, F. D. Carsey, and P. Gloersen, Antarctic Sea Ice, 1973-1976: Satellite passive-microwave observations, NASA SP-459, 1983.

Figure 1: Map of the North Water area

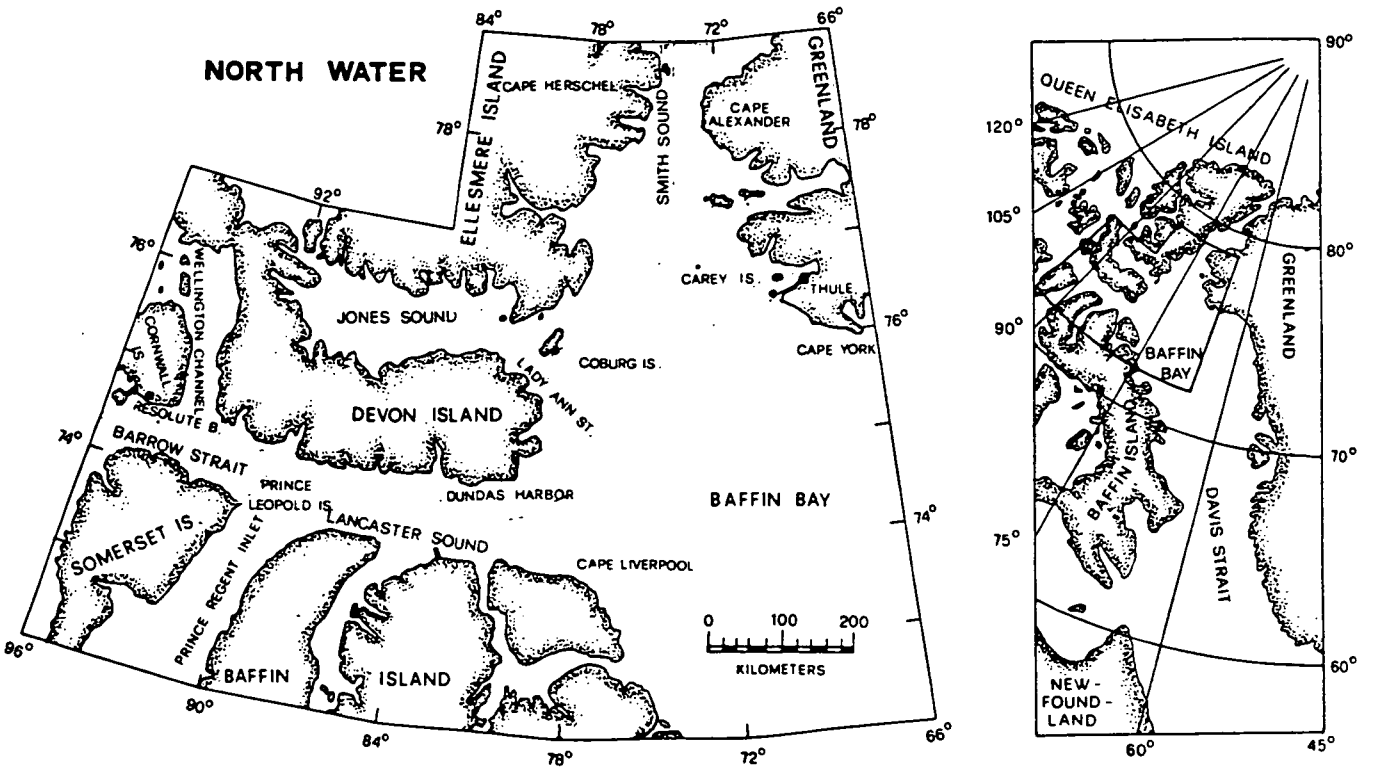

Figure 2: Polarization ratio (PR) at 18 GHz and 37 GHz for white ice (WI), grey ice/grey-white ice (GI), nilas (NI), open water (OW), and for mixed-ice SMMR pixels for white ice/grey ice (WIGI), white ice/nilas (WINI), white ice/open water (WIOW) and grey ice/nilas (GINI). These values were derived from Landsat/SMMR intercomparison (Steffen and Maslanik, submitted).

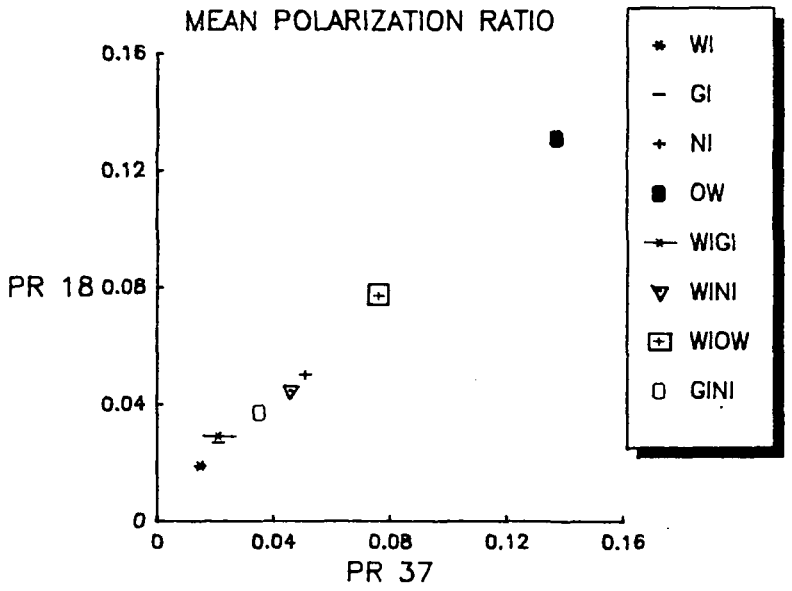

Figure 3: Ice type percentage for the North Water area (100,000 km^2) derived from SMMR passive microwave data (37 GHz polarization ratio) for the winter 1978/79. The lower part of the graph dispicts the four weeks mean of the ice types white ice (WI), grey ice (GI), nilas (NI) and open water (OW).

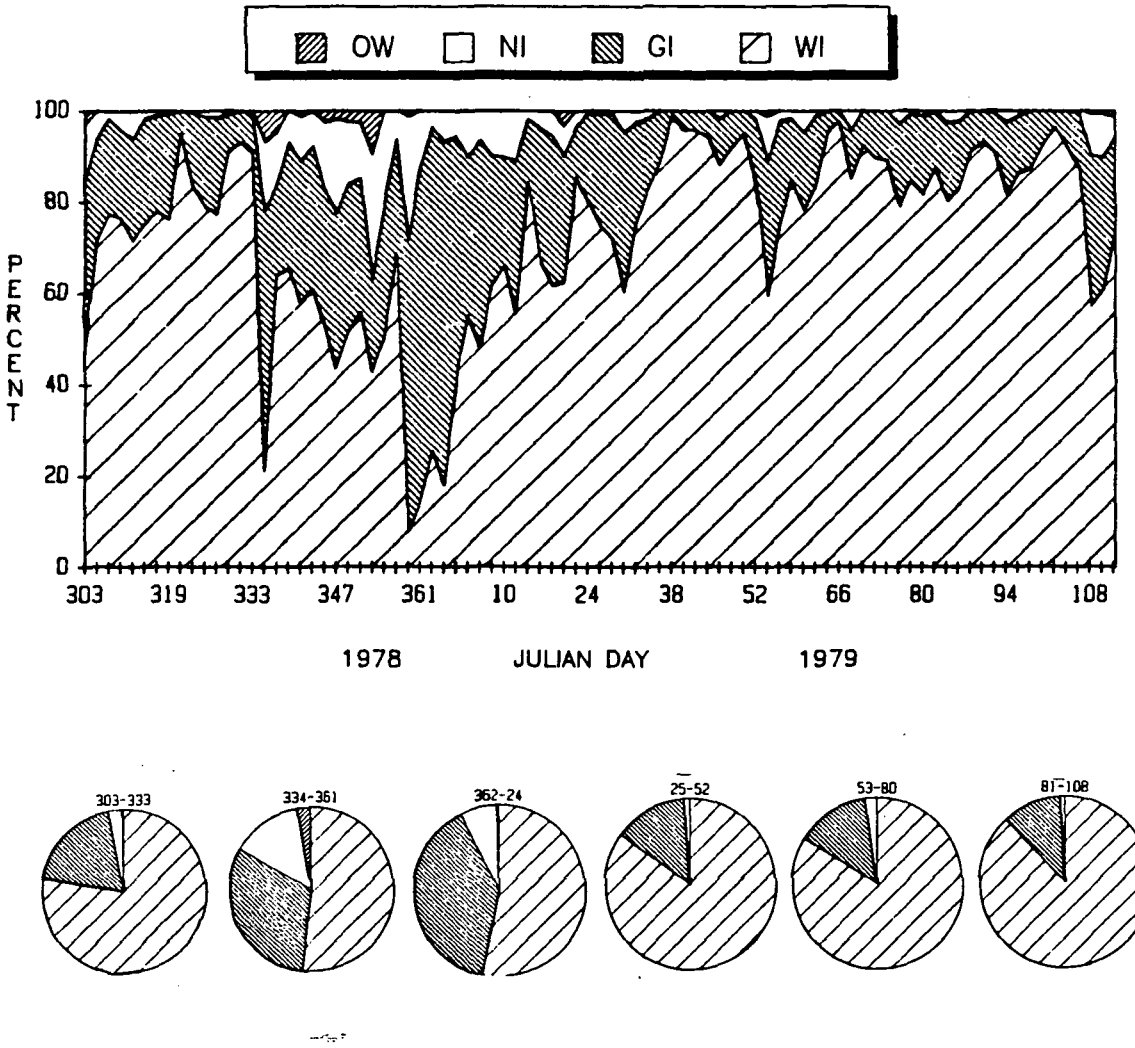

Figure 4: Ice type percentage for the North Water area (100,000 km^2) derived from SMMR passive microwave data (37 GHz polarization ratio) for the winter 1980/81. The lower part of the graph dispicts the four weeks mean of the ice types white ice (WI), grey ice (GI), nilas (NI) and open water (OW).

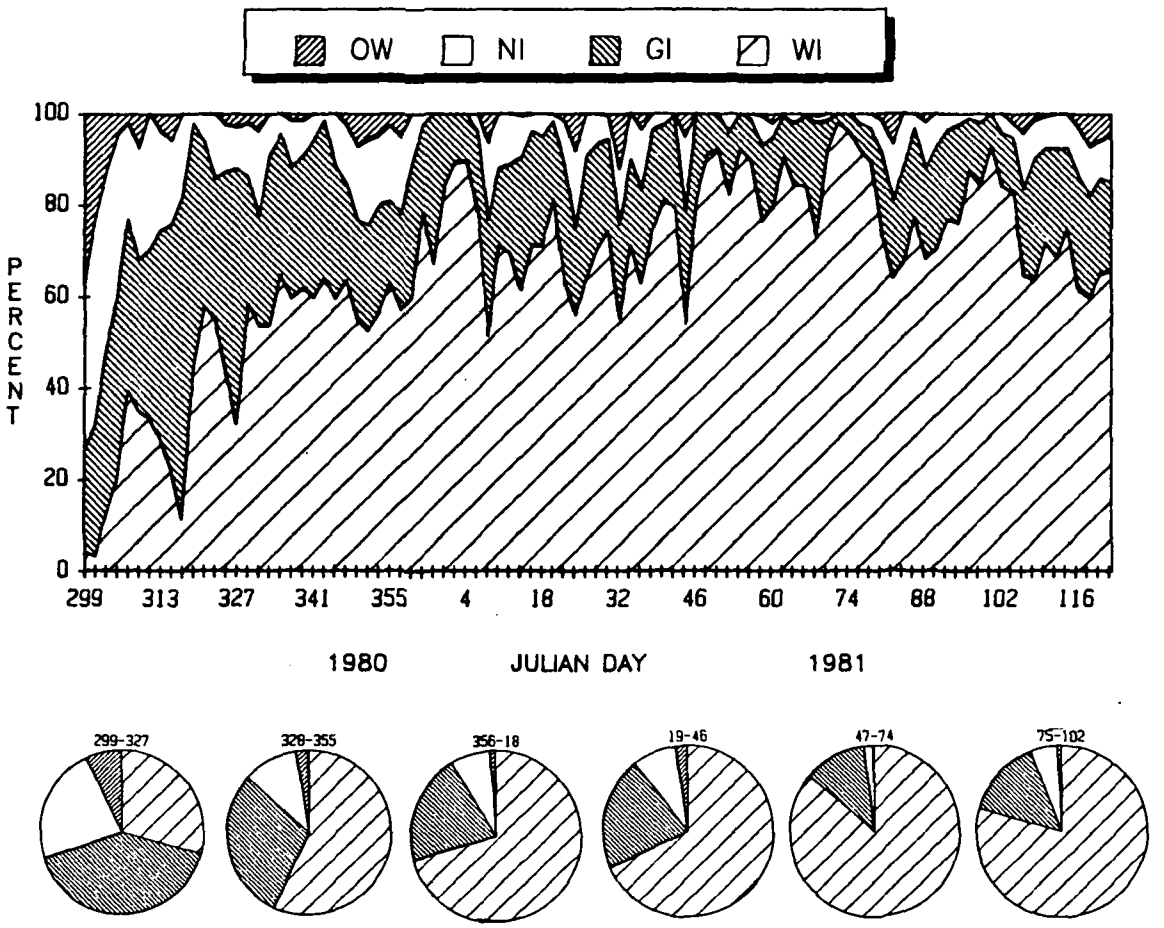

Figure 5: Time sequence of the brightness temperature (TB) 37 GHz horizontal polarization for the Cape Alexander and Carey Oer region. When both graphs indicate a large decrease in TB, a major storm occurs over the North Water resulting in large change in the ice cover. See Table 1 for the different storm types.

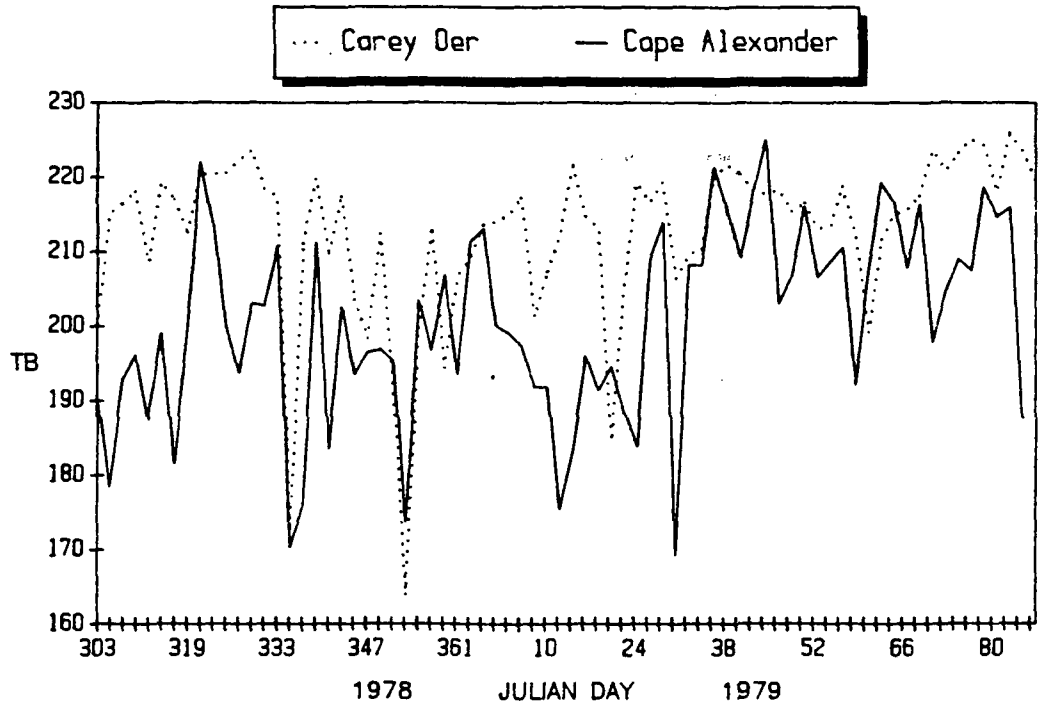

Appendix C

Comparison of Nimbus 7 SMMR Microwave Radiance and Derived Sea Ice Concentrations with Landsat Imagery for the North Water area of Baffin Bay

Konrad Steffen and James A. Maslanik

Cooperative Institute for Research in Environmental Sciences, Campus Box 449, University of Colorado, Boulder, CO 80309

Abstract

Landsat imagery for the northern Baffin Bay (May to June, 1981) is used to compare ice concentration estimates derived from Nimbus 7 Scanning Multichannel Microwave Radiometer (SMMR) data. Periods of pre-melt, onset of melt and melt are identified based on changes in brightness temperature and on gridded air temperature data from the European Center for Mid-Range Weather Forecasting. Differences between multispectral SMMR and Landsat-derived total ice concentrations are within 3.5% for pre-melt and onset of melt periods. During melt, differences increase to about 10%. Differences for individual SMMR footprints are greater, and contribute to a mean correlation coefficient of 0.53 between SMMR and Landsat-derived ice concentrations. The SMMR data yield slightly lower estimates of total ice concentration, and for individual SMMR footprints tend yield lower estimates at high concentrations and higher estimates at low concentrations relative to the Landsat interpretation. Although statistically different, the mean concentrations derived using the Landsat and SMMR data were separated by less than 10% in virtually all cases. Possible reasons for these discrepancies are discussed. The brightness temperatures for compact pack ice compared to fast ice are on the average 10 K higher at vertical polarization, and 15 K higher at horizontal polarization for 18 and 37 GHz during the pre-melt period. Classification of ice types such as first-year ice, young ice and nilas by means of polarization ratios seems feasible for large homogeneous areas of a single ice type.

1. Introduction

Over the past 15 years, passive microwave data collected by satellites have been used to monitor sea ice in polar regions. The first circumpolar ice concentration map was obtained from the Nimbus 5 one-channel Electrically Scanning Microwave Radiometer (ESMR) (Gloersen et al., 1974). Based on ESMR data, sea ice concentration maps were produced for the Arctic (Parkinson et al., 1987) and the Antarctic (Zwally et al., 1983). Using the multiple frequencies provided by the Nimbus 7 Scanning Multichannel Microwave Radiometer (SMMR) in 1976, algorithms to derive sea ice concentrations were improved, resulting in more accurate estimates of ice concentration, and the ability to map ice types (Cavalieri et al., 1984; Comiso, 1986; Gloersen and Cavalieri, 1986).

Long term monitoring of sea ice is of prime interest for studies of global climate. Polar regions are sensitive to small climate changes that affect the seasonal fluctuation of the sea ice cover, and the associated modifications of albedo and energy transport. In order to detect changes in the ice cover, the overall accuracy with which geophysical sea ice parameters (e.g. ice concentration) are retrieved from satellite data has to be known. Due to the coarse satellite footprint of the ESMR and SMMR radiometers (30-150 km), a direct comparison with ground-truth measurements is not feasible, especially in pack ice regions where large changes of ice concentration and large variability in ice types occur within one satellite footprint. However, surface-based passive microwave observations of sea ice are essential for the interpretation of satellite data. The effect of snow cover on emissivity, and the change in brightness temperature of different frequencies as ice thickness increases are important factors and have been investigated in detail for limited case studies (Matzler, 1982; Matzler et al., 1984; Grenfell and Comiso, 1986). Surface-based passive microwave measurements collected by Grenfell and Lohanick (1985) during the onset and development of melt on pack and fast ice point out the local variability of the ice surface. Satellite or aircraft based measurements are probably best suited to estimate the accuracy of the sea ice products derived from Nimbus 7 SMMR data due

to similar sizes of area sampled. In the past only a few such comparisons have been carried out. A comparison of aircraft passive microwave data, thermal infrared data and aerial photography with SMMR data was reported for the Bering sea ice cover by Cavalieri et al. (1986), and for the Greenland Sea by Burns et al. (1987) and Campbell et al. (1987). Observations of near-shore Beaufort sea ice using passive and active microwave measurements were reported by Campbell et al. (1980). The latter measurements were also compared with geophysical sea ice parameters obtained with the ESMR radiometer. Comparisons of data from airborne and Nimbus-5 ESMR and surface investigations in the Beaufort Sea have been widely reported (Campbell et al., 1976; Campbell et al., 1978; Gloersen et al., 1973; Gloersen et al., 1978. Similar comparisons were reported as a result of a cooperative US/USSR experiment in the Bering Sea (Kondratyev et al., 1975; Gloersen et al., 1975a; Gloersen et al., 1975b; Ramseier et al., 1975). Ice concentrations derived from Nimbus 5 one-channel ESMR radiometer have also been compared with Landsat imagery for the Antarctic pack ice (Comiso and Zwally, 1982a).

In this paper, we present a comparison of microwave radiances and sea ice concentrations derived from Nimbus 7 SMMR data with ice parameters interpreted from Landsat imagery. The study area is delineated by longitudes 66° and 96°W and parallels 72°, 77° (84°-96°W), and 79°N (66°-84° W) (Figure 1). This area, which includes the North Water, does not show consistent, substantial ice cover during winter and spring as one might expect from the climatic conditions (Steffen, 1985; 1986). The North Water area is dominated by loosely packed ice, and it includes the three polynyas of Lancaster Sound/Barrow Strait, Smith Sound and Lady Ann Strait (Figure 1), the latter two of which are known as recurring polynyas. At its northern extremity between Greenland and Ellesmere Island at 79°N, the North Water is bounded by fast ice. Its southern boundary, however, cannot be clearly defined because the concentration of pack ice gradually increases toward Baffin Bay to the south.

2. Extraction of geophysical parameters from satellite data

2.1 Landsat Multispectral Scanner (MSS)

Landsat imagery in the form of positive paper prints in 240 mm format for MSS band 7 (near infrared, 800-1100 nm) were used. The observation area was divided into 55,000 small rectangular cells (2.54x4.23 km). The predominant ice type in each cell was determined visually. The sea ice classification was made on the basis of age (distinguishable by different grey tones) and according to whether the ice in question is attached to land (fast ice) or not (pack ice). Six ice types and two additional categories were identified: (1) fast ice; grey-white or thicker; (2) fast ice; grey ice and nilas; (3) pack ice; grey-white ice or thicker; (4) pack ice; grey ice; (5) pack ice; nilas; (6) pack ice; new ice or ice free; (7) land, and (8) data missing. The ice types were classified using standard nomenclature for sea ice (World Meteorological Organization, 1970). The results of this sea ice classification using Landsat are published in the form of an atlas (Ito, 1982). The data from the atlas, originally in Universal Transverse Mercator (UTM) coordinates, were transformed to the 25x25 km grid format in a polar stereographic projection as specified for the DMSP Special Sensor Microwave Imager (SSM/I). For each 25x25 km SMMR footprint, up to 72 Landsat ice information cells were available. The following number of SMMR footprints (abbreviated as SF) were compared for six different Landsat data sets: 55 SF consisting of fast ice only, 230 SF fast ice/land mixture, 260 SF pack ice only, 38 SF fast ice/pack ice mixture, 46 SF fast ice/pack ice/land mixture, and 210 SF containing land only. To cover the area of investigation with Landsat 2 imageries required 12 successive days. Data for the nearest Nimbus 7 satellite path were used for each Landsat path. Since SMMR data are available every other day for the entire North Water area, the two data sets are separated in time by one day at most. In this paper, the middle day of the full time period for each Landsat-derived map is used to represent the map. There are 13 such periods in the daylight half of the year. The first 6 periods (March to June) of the year 1981 were used for the Landsat/SMMR comparison.

During the "North Water Project" (1972-1981), a number of climatological, glaciological and aerological measurements were carried out (Muller et al., 1977; Steffen and Ohmura, 1985). During the winters of 1978/79 and 1980/81, a sea-ice station was established at latitude 74°40'N,

longitude 95°10'W in Barrow Strait near Resolute Bay. Observations from this station provided ground truth for airborne infrared thermometry over the North Water area (Steffen, 1986), and served as a source of all energy flux measurements on the sea ice. Ice thickness and salinity profiles of sea ice, as well as snow depth and density were also measured on alternate days. These results served as ground truth for the interpretation of the SMMR data.

2.2 Nimbus 7 Scanning Multichannel Microwave Radiometer (SMMR)

Passive microwave data used in this study were acquired by the Nimbus 7 Scanning Multichannel Microwave Radiometer (SMMR). The SMMR which was launched in October 1978 operates at five frequencies (6.6 GHz, 10.7 GHz, 18.0 GHz, 21.0 GHz, and 37.0 GHz). The microwave radiances are measured at both H and V polarizations for each frequency. The 18 GHz (1.67 cm wavelength) and 37 GHz (0.81 cm wavelength) were used throughout this paper for the derivation of sea ice products. For more information on the Nimbus 7 SMMR see Gloersen and Barath (1977).

The process of converting from SMMR footprint data to CELL-ALL format (orbital data) generates cell sizes of 60x60 km for the 18 GHz channel, and 30x30 km for the 37 GHz data. The SMMR data used here have been converted further from CELL-ALL format to the polar stereographic format planned for the DMSP SSM/I, with both the 18 and 37 GHz data mapped to grid cells with a dimension of 25x25 km at 70 degrees latitude. The 18 GHz data are interpolated to accommodate the 25 km resolution grid. During the gridding process, no distinction is made between day, night, and twilight orbits. Tapes containing these data (and the remaining SMMR channels gridded to 50 km cells) mapped onto the SSM/I grid are archived at the National Snow and Ice Data Center (NSIDC), Boulder, Colorado.

Mapping of sea ice parameters using passive microwave data is possible due to the large difference in emissivity between calm water and sea ice. In addition, the differences in emissivity of first-year versus old ice (sea ice that has survived at least one melt season) at different

microwave frequencies provide a means of separating ice types. The capabilities of SMMR data, and passive microwave data in general, have been discussed in a number of articles (Svendsen et al., 1983; Comiso, 1983; 1986; Cavalieri et al., 1984; Gloersen and Cavalieri, 1986). These capabilities will not be addressed further, except to note that surface snow cover, surface roughness, thin ice types, and direct and indirect weather effects modify the emissivities observed by SMMR, and therefore affect the ability of SMMR-based algorithms to retrieve accurate ice information.

The derivation of ice type and concentration from the SMMR data was carried out using the algorithm described by Cavalieri et al. (1984), with the addition of the weather filter as discussed in Gloersen and Cavalieri (1986). This algorithm, referred to as the SMMR Team (ST) algorithm, is based on ratios of radiances, the polarization ratio (PR) and gradient ratio (GR), and uses representative brightness temperatures to serve as "tie-points" for surfaces of 100% water, first-year ice, and old ice. The ratios are defined as follows:

$$PR(f) = (T_{BV}(f)-T_{BH}(f))/(T_{BV}(f)+T_{BH}(f)) \quad (1)$$

$$GR = (T_{BV}(37)-T_{BV}(18))/(T_{BV}(37)+T_{BV}(18)) \quad (2)$$

where T_{BV} and T_{BH} are the observed vertically polarized and horizontally polarized brightness temperatures, respectively, and f is either 18 or 37 GHz. The ST algorithm has been chosen by NASA as their operational algorithm for ice mapping using SMMR and SSM/I data. Performance characteristics of the ST algorithm are discussed by Swift and Cavalieri (1985). In its implementation, the algorithm uses vertically-polarized data for the gradient ratio, and 18 GHz or 37 GHz data for the calculation of the polarization ratio. The ST algorithm based on 18 GHz will be referred to as ST_{18}, and based on 37 GHz as ST_{37}. A detailed account of the reduction of weather effects in the calculation of sea ice concentration using the ST algorithm is reported by Gloersen and Cavalieri (1986).

Ice concentrations in the Bering Sea, predominately first-year ice, were also calculated using a single-channel, linear interpolation approach (Cavalieri and Martin, 1985) that compares the observed brightness temperature to tie-point brightness temperatures. The algorithm is defined as

$$C = (T_B - T_{BW})/(T_{BI} - T_{BW}) \quad (3)$$

where C is the calculated ice concentration, T_B is the observed brightness temperature at a given satellite footprint, and T_{BW} and T_{BI} are the brightness temperatures (tie-points) of 100% water and 100% ice, respectively. The algorithm was used with 37 GHz vertically-polarized data, and will be referred to as LI_{37}. The validity of this simple linear algorithm is limited to small areas where the ice temperature may be assumed constant and where the ice has a simple radiometric signature.

3. Comparison of Landsat and SMMR derived ice parameters

3.1 Seasonal change of white ice brightness temperatures

Regardless of age, oceanic white ice ice can be divided into two broad categories based on its ability to move. These types are fast ice and pack ice (also called drift ice). The surface of fast ice is typically characterized as smooth with little rafting and ridging, and its snow cover exceeds that on pack ice by up to 30% in thickness. The field measurements on the fast ice near Resolute Bay (spring 1981) showed snow depths of 0.1 m on flat surfaces with larger depths among the few ridges. A hard wind-crust was common on the snow surface. Growth of fast ice in early fall is slow resulting in a smaller amount of salt trapped in the brine pockets compared to faster-growing pack ice (Nakawo and Sinha, 1984). Figure 2 shows a systematic salinity observation throughout the complete growth season on the fast ice in Barrow Strait near Resolute Bay. Fast ice is also unique in offering several properties (e.g. homogenous ice cover

with no fractures, snow cover usually thicker than on pack ice) that make it useful for passive microwave studies. The fact that fast ice can be considered as 10/10ths concentration, with white ice of a uniform surface and a fairly even snow cover in spring serves to eliminate several of the variables that add ambiguity to ice classification using SMMR. The most significant drawback to the study of fast ice using SMMR is the potential mixing of responses from the ice and the adjacent land.

The surface temperature of white ice (T_s=255 K) was measured on March 2, 1981 during the remote sensing flight (Steffen and Lewis, in press). Other physical temperature records for the time of the SMMR/Landsat comparison were not available. Gridded air temperatures (T_a) at 1000 mb from the European Center for Mid-Range Weather Forecasting (ECMWF) were used to estimate T_s. The comparison of ECMWF T_a and in-situ T_a measurements on March 2, 1981 (remote sensing flights) showed a 10 K difference indicating that the gridded temperatures do not fully reflect the local effects of the North Water. Contact of the Arctic air mass with the water surface and thin ice areas significantly changes air temperatures during winter and spring. This change consists mainly of heating caused by the large sensible heat flux of the polynya (Steffen, Ohmura, 1985). The ECMWF T_a were corrected for the local warming in the North Water region (+10 K in March, +8 K in April, +6 K May, +4 K in June) resulting in the following values: 255 K on March 2, 255 K on March 30, 264 K on April 12, 271 K on May 5, 273 K on May 17 an 276 K on June 8. Because snow and ice are good insulators, air temperature and snow surface temperature can be considered equal for ice (>1 m) with a snow cover of at least 0.1 m. Based on these corrected temperatures, the SMMR/Landsat comparison can be divided into a pre-melt period (March 2, March 30, April 12, 1981), a period of likely onset of melt (May 5, May 17, 1981), and a melt period (June 8, 1981).

Since the ST algorithm uses T_B tie-points typical for white ice, the seasonal change in white ice T_B may effect the calculation of ice concentrations. Figures 3,4 and 5 show the frequency distribution of the T_B of pack ice and fast ice at 37 and 18 GHz. The effect of the adjacent land on brightness temperatures was minimized by selecting only those SMMR grid elements that

included no land as determined from the Landsat data. Although this approach helps to assure that the SMMR grid elements selected are entirely over ice or water (within the limits of the precision of earth location), it does not serve to eliminate the influences of land on the SMMR observations due to the wings of the main antenna lobe outside a given grid element.

The analysis shows that the T_B of fast ice is significantly lower than pack ice T_B during the pre-melt period (Figure 3). A t-test analysis of the population of fast ice and pack ice T_B on March 2, 1981 shows that the probability for equal T_B of fast and pack ice is less than 0.05. The mean difference between pack ice and fast ice T_B is 11 K for vertical polarization and 14 K for horizontal polarization (18 GHz and 37 GHz). During the pre-melt period (March 2, March 30, and April 12, 1981), this difference remained constant. Several explanations can be given for the reduced T_B of fast ice. Our remote sensing flights over the same area on March 2 and March 16, 1981 showed that the fast ice surface temperature (T_s) was 10 K lower on the average than that of compact pack ice (Steffen and Lewis, in press). The T_B difference of pack ice and fast ice at vertical polarization is, therefore, caused primarily by differences in the physical temperature in the snow cover and not by emissivity. Also, microwave scattering due to density and structure variations in the snow cover reduces the brightness temperature further, particularly at horizontal polarization. Our field measurements indicate that the snow cover on fast ice is up to 30% thicker than on pack ice. Scattering due to this greater snowdepth would also explain part of the T_B difference. The higher T_s of pack ice can be partly attributed to the thinner ice over the upwelling ocean in the North Water region (Steffen, 1985), and partly to the warmer air temperature in the pack ice region caused by the extensive sensible heat flux in that area (Steffen and Ohmura, 1985). These three effects - (1) thinner pack ice compared to fast ice, (2) thicker snow cover on fast ice, and (3) warmer air temperatures in the pack ice areas - are assumed to account for the observed T_B difference of the two ice types.

Figure 4 shows the frequency distribution of T_B for pack and fast ice for May 5, 1981. The t-value comparing the two T_B of pack ice and fast ice decreases throughout the period assumed to represent onset of melt (May 5 and May 17, 1981). For 18 GHz horizontal polarization, the

probability of equal means (pack ice versus fast ice) cannot be rejected. The mean T_B of fast ice increases by 10 K from pre-melt to onset of melt. For pack ice the increase was found to be 5 K.

For the first time in the season, 18 and 37 GHz T_B are higher for fast ice than for pack ice, whereas the t-test analysis shows no significant difference between the T_B means of pack ice and fast ice. The lowest T_B of 186 K was found for the horizontally-polarized microwave radiation at 37 GHz.

For the typical first-year ice cover in the North Water area, the microwave emission emanates mainly from the snow/ice interface, since the optical depth of saline, first-year ice is in the order of the wavelength of the radiation. For first-year ice, scattering of microwave radiation can be neglected except for that caused by snow or crusts on the ice surface. The emission from the snow itself is negligible unless the snow pack is unusually thick (>1 m) (Comiso et al., 1982b). During the onset of melt however, the emissivity of snow changes due to the presence of a thin water film forming around the snow grains. This change increases the dielectric constant, lowers scattering loss, and thus results in a higher observed T_B (Stiles and Ulaby, 1980), which can be seen in Figure 6. This phenomenon was also reported for other Arctic regions by Livingstone et al. (1987). The comparison of ice T_B also shows that, during the pre-melt period, the smallest standard deviation of T_B occurs for pack ice at 18 GHz vertical polarization (Figure 6). The black diamonds in Figure 6 represent the mean +standard deviation of three pre-melt cases of the Landsat/SMMR comparison (March 2, March 30, and April 12, 1981). The largest standard deviation is found for 37 GHz during the melt period (June 8, 1981). In general, the T_B increases between pre-melt and onset of melt with little change in the standard deviation. During the melt period, the T_B falls below the pre-melt value with a significant increase in the standard deviation due to freeze/thaw cycles. The largest change was observed for the 37 GHz data, whereas the T_B for fast ice at 18 GHz V, unlike the 37 GHz data, shows a further increase in T_B between onset of melt and melt. It is worth noting that the standard deviations of white ice T_B is smaller for pack ice than for fast ice throughout the season.

3.2 Effects of adjacent land on sea ice T_B

In mapping sea ice T_B close to land (e.g. in bays, channels and along the coast), there is always a potential risk of mixing the emissivity responses from sea ice and adjacent land due to the large footprint of SMMR. This effect is shown in Figure 7, where the change in fast ice T_B is plotted for SMMR footprints containing different percentages of ice and land as classified by the Landsat data.

A decrease of 3 K at 18 GHz, 6 K at 37 GHz, respectively, for the fast ice T_B was found for a SMMR footprint containing 50% snow-covered land during the pre-melt period (March 30, 1981). During this time period, the snow cover had a mean depth of 0.5 m, whereas in ravines and small valleys, snow depths due to wind drift of up to 1.5 m were measured. The observed decrease in T_B with the inclusion of land is speculated to be caused primarily by the microwave scattering due to the thicker snow cover on the land, and secondarily by the different emission properties of first-year ice and permafrost. This would also explain the larger decrease in T_B for 37 GHz compared to 18 GHz due to the greater scattering of short wavelengths by snow. For the melt period (June 8, 1981), only a small change in T_B (<3 K) due to the mixing of sea ice and land footprints was found as long as ice and land were covered with wet snow.

3.3 Polarization ratios of ice types

The knowledge of ice type distribution is important for determining large-scale heat input at the ice-atmosphere boundary. Despite the extremely rapid decrease in energy-exchange rates as ice forms in open water, young ice with a thickness of 0.3 m still has a net heat loss of an order of magnitude larger than that of thick first-year ice (Steffen, 1986).

The hemispheric coverage and the year-round availability of satellite passive microwave measurements provide us with an ideal data set for the estimation of large scale energy fluxes

over pack ice. In the following, the possibility of ice type classification with the use of different SMMR channels is demonstrated. Our analysis is limited to 18 and 37 GHz, because of the strong attenuation due to atmospheric water vapor in the 21 GHz channel, and the large footprints (55 km and 150 km) for 10.7 GHz and 6.6 GHz, respectively. The polarization ratio (PR) of 18 and 37 GHz was used for the ice typing. Old ice is not found in the North Water area during the times studied, and therefore will not be discussed further. White ice (WI), grey ice (GI), nilas (NI) and open water (OW) categories (World Meteorological Organization, 1970) classified in the Landsat data set according to their grey tone were compared with the SMMR polarization ratios. The comparison was made for each 25x25 km SMMR footprint of the North Water pack ice for which 100% of the above specified ice type occurred. The analysis covered the period of pre-melt and onset of melt (March, April and May) in 1981.

For the three ice types WI, GI and NI, the PR at 18 and 37 GHz increases with decreasing ice thickness. The standard deviations, shown as diamonds in Figure 8a, do not overlap, indicating that a classification of ice type based on satellite derived PR may be possible over fully consolidated ice. Similar results were reported for aircraft measurements (Cavalieri et al., 1986) and for ground measurements (Grenfell, 1986). The standard deviations of open water show a broad range that can be explained by the presence of small ice floes not resolved in the Landsat imagery, and by the change of T_B due to spray and foam on the ocean surface and variations in cloudiness. Ice type classification by means of PR seems feasible for large homogeneous ice areas consisting of a single ice type. In nature however, young ice like nilas and grey ice seldom completely covers areas of 25 x 25 km (one SMMR footprint).

To address this problem, the polarization ratios of mixed-ice SMMR footprints were analyzed. All SMMR footprints consisting of white ice/grey ice (WIGI), white ice/nilas (WINI), white ice/open water (WIOW) and grey ice/nilas (GINI) of which each ice type, e. g. WI and GI, covered 50% of the SMMR footprint, were classified according to the Landsat data. The PR at 18 and 37 GHz are given in Figure 8b. Again the periods of pre-melt and onset of melt were analyzed. The number of SMMR footprints (SF) which fulfill the classification criteria were the

following: WIGI 55 SF, WINI 6 SF, WIOW 31 SF, and GINI 5 SF. The mean PR +standard deviation for WIGI, WINI and GINI partly overlap with the ones of the ice types GI and NI, and therefore, a clear distinction based on PR is not possible. If we compare the mean PR only (Figure 8c), GI and WIGI signatures are almost identical. It is assumed that with a smaller satellite footprint, the PR standard deviation for ice types (e.g. GI, NI) and ice type mixtures (e.g. WIGI) would decrease. Further, an additional channel with the same satellite footprint as 37 GHz, or smaller (e.g. SSMI 85 GHz: 15x15 km) would increase the classification accuracy of young ice types. This analysis shows that ice types such as white ice, grey ice, and nilas can be classified if they occur over large homogeneous areas. For climatological applications such as heat flux estimations over pack ice areas, the PR-method for ice typing appears promising. A detailed analysis for the North Water area throughout the winter is under preparation.

Lastly, the polarization ratio for different white ice concentrations was analyzed for the melt period (June 8, 1981). The total number of SMMR footprints (SF) for each category is the following: WI100 (no open water) 95 SF, WI80 (20% open water) 31 SF, WI60 (40% open water) 6 SF, WI40 (60% open water) 2 SF, WI20 (80% open water) 4 SF, OW (100% open water) 49 SF. The PR value of 100% white ice is more than twice as large during the melt period than the pre-melt period (Figures 8a,d). The PR value for white-ice concentration increases linearly with decreasing concentration. The large standard deviations can be attributed to the small sample size, to small ice floes in open water (sub-resolution to Landsat imagery), and to the change in T_B due to variation in surface winds and cloudiness (very high surface winds are known to occur in North Water in winter and early spring).

3.4 Spatial and temporal variations of tie-points

Successful application of the sea ice algorithms described earlier is controlled to a significant degree by the brightness temperatures selected to represent the 100% concentrations of first-year ice, old ice, and open water. The selection of these tie-points can be carried out in

several ways. Typically, tie-points are selected by locating areas that are likely to represent a single surface type, and then selecting the minimum (for old ice and open water) and maximum (for first-year ice) T_B observed in each area (Cavalieri, et al., 1984).

In the present study, the Landsat data provided sufficient control to establish areas of approximately 100% ice, and offered a standard against which the SMMR-derived ice concentrations could be compared. Several approaches for tie-point selection for 100% first-year ice were tested. Because of lack of old ice and, in most cases, a lack of large open water areas in the North Water, tie-points for old ice and open water were chosen from published figures (Cavalieri, et al., 1984; Comiso, 1983). Best agreement between SMMR and Landsat derived ice concentration was achieved using as white ice tie-points the mean T_B plus one standard deviation for SMMR footprints corresponding to areas shown as 100% pack ice in the Landsat data. These tie-points were used throughout this study and are shown in Figure 9 for the six different data sets for 1981. For the northern Baffin Bay, the mean, standard deviation and maximum brightness temperature for 100% white ice (18 and 37 GHz) are presented in Table 1. Compared to the first-year ice tie-points published by Cavalieri et al. (1984) for the Baffin Bay , the "North Water" tie-points (northern Baffin Bay) are on the average 10° K higher during the pre-melt period. This regional difference in brightness temperatures for white ice is significant (see also Section 3.1.).

The changes in the pack ice tie-points over time provide a good indication of changes in the snow/ice cover typical of the progression from spring to early summer. Average mid-winter first-year ice T_B ranged from 239 to 241 K for vertically-polarized data (18 and 37 GHz), and 234 to 235 K for horizontally-polarized data (18 and 37 GHz) (March 2 and March 30, 1981). On April 12, 1981 decreases in the horizontally-polarized T_B at 18 and 37 GHz, and an additional decrease at 37 GHz V were found compared to the two previous data sets. This reduction in T_B could result from melt-freeze cycles affecting the metamorphosis of ice lenses and snow crystals. These cycles generate large crystals and crusts that preferentially scatter horizontally-polarized radiation, with greatest effect at higher frequencies (Foster, et al., 1984; Stogryn, 1986). Schanda

and Hofer (1977) describe how melt-freeze metamorphosis may cause preferential lowering of brightness temperatures at higher frequencies in snow packs. On May 5 and May 17, 1981 an increase in all T_B occurred, with larger amplitudes at vertical polarizations. This change could be attributed to the onset of melt as discussed earlier in this paper. During the melt period (June 8, 1981) the T_B decreased significantly, particularly at 37 GHz. Comiso (1986) observed similar patterns over time for the Weddell Sea ice pack using SMMR data, and Grenfell and Lohanick (1985) and Grenfell (1986) measured the effect on brightness temperatures of such surface changes. Melt-freeze metamorphism are considered to be the likely cause of the observed changes in emissivity.

3.5 Ice concentration

Ice concentrations were calculated for ST_{18}, ST_{37} and LI_{37}, and were compared with the Landsat data (Figure 10). In the following, only the comparison of ST_{18}-derived ice concentrations and Landsat ice concentrations will be discussed. The ST_{37} and LI_{37} ice concentrations, used by several authors in the past (e.g. Cavalieri and Martin, 1985), are also given in Figures 10 and 12.

The ST_{18} algorithm consistently yielded lower total concentrations than those produced by the Landsat interpretation, with the exception on May 17, 1981. Part of this difference may be attributed to the ability of SMMR to detect leads that were not visible in the Landsat imagery. The largest difference between the Landsat and ST_{18}-derived ice concentrations was 10% on June 8, 1981, the minimum difference of -1.5% was found on May 17, 1981. The statistical significance of these differences were tested using two-tailed t-tests. With the exception on May 17 and June 8, 1981, the hypothesis of equal means can be rejected at the 99% significance level. On May 17, 1981, the ST_{18} and Landsat-derived concentrations appear equal. Ice concentrations on June 8, 1981 show a greater difference, but can still be considered equal at a 95% confidence level. Although statistically different, the mean concentrations derived using the

Landsat and SMMR data were separated by less than 10% in virtually all cases. However, the range of differences for individual satellite footprints can be large. The largest observed differences for individual footprints are ST_{18}-derived concentration greater than Landsat by 84% on May 17, 1981, and Landsat-derived concentration greater than ST_{18} by 45% on June 8, 1981 (Figure 11).

To determine whether the differences between concentrations are limited to particular locations, plots were generated showing the spatial distributions of positive and negative deviations between SMMR and Landsat concentrations. The Landsat-derived concentrations are typically greater than the ST_{18} concentrations over high ice concentration areas, with the largest differences occurring on pack ice in Lancaster Sound and several locations in southern Smith Sound. The cases where the SMMR data show greater ice concentration than that classified from the Landsat imagery appear to be associated with grey ice, nilas, and new ice/open water areas, and for low ice concentration areas. Figure 11 shows Landsat-derived ice concentration versus the SMMR-derived ice concentration for the melt period (June 8, 1981). We believe that the somewhat poor correlation coefficients between the Landsat and SMMR ice concentration, compared to the good agreement with the mean Landsat/SMMR ice concentration, can be attributed to the dynamic nature of the pack ice in the North Water area, as the two satellite paths - Nimbus and Landsat - can be separated in time by as much as one day.

An additional comparison of ice concentrations was performed using concentration classes summed over 20% intervals, as described in section 3.3. For the 80% class (based on the Landsat-derived concentrations), the ST_{18} algorithm yielded 71%, the 60% class 68%, the 40% class 49%, and the 20% class 44% respectively. Thus, although the ST_{18} algorithm produced lower total sea ice concentrations than shown by the Landsat interpretation, this difference is limited to high concentration areas. These tendencies could be explained by (1) the ability of SMMR to detect sub-resolution leads in high concentration areas, and (2) a possible mis-classification of thin ice types as open water using the Landsat imagery. The overestimation of ST_{18}-derived ice

concentrations for low concentrations may be due to surface effects such as spray and foam on the open water or heavy clouds. As noted earlier, these effects reduce polarization and cause an increase in brightness temperature which in turn cause the ST_{18} algorithms to overestimate ice concentration.

Figure 12 depicts correlation coefficients of Landsat versus ST_{18}, ST_{37}, and LI_{37} derived ice concentrations, with each satellite grid element treated as a separate case. Differences between the algorithms are more apparent than in the comparison of the total concentrations, with LI_{37} showing the poorest agreement with the Landsat data. All algorithms yield a relatively poor correlation on May 5, 1981. As noted earlier, this date appears to represent the onset of surface melt in the data set used. The greater sensitivity of the 37 GHz channel to surface effects may explain the poorer correlations, on April 12 and June 8, 1981, of the ST_{37} compared to ST_{18} values based on this channel.

In summary, ice concentrations derived from the SMMR data appear to agree well with the concentrations interpreted from the Landsat imagery when the concentrations are represented as total concentrations summed over the entire study area. Differences are small even during the melt condition, although more significant differences occur when spatial comparisons are made, and when concentrations are divided into ranges. Some of these differences may be due to sub-resolution leads, thin ice types, or surface effects on open water areas, and due to the time difference of the two satellite paths. Also, a major reason for these differences when comparing individual FOV's is that a given FOV represents only 50% of the actual power received by the radiometer. The remaining 50% of the received power lies outside the FOV. In addition, agreement between SMMR and Landsat-derived concentrations are different during the periods of pre-melt (March and April), onset of melt (May) and melt (June).

4. Conclusions

The main objectives of this comparison between Nimbus 7 SMMR and Landsat MSS data were: (1) to study the seasonal variations of white ice brightness temperatures; (2) to test the ability to classify ice types (e.g. nilas, grey ice) based on SMMR data; (3) to determine the accuracy of ice concentration derived from Nimbus 7 SMMR data relative to Landsat data; and (4) to identify reasons for discrepancies between Landsat and SMMR-derived ice concentrations.

The analysis has shown that pack ice T_B is on the average 10 K higher than fast ice T_B for vertically polarized data, and 15 K higher for horizontally polarized data at 18 and 37 GHz during the pre-melt period. During the onset of melt, the mean difference in T_B between pack ice and fast ice decreases and is nonexistent during the melt period. The three effects - (1) thinner pack ice compared to fast ice in the North Water region; (2) warmer air temperatures in the pack ice areas due to large sensible heat flux; and (3) thicker snow cover on fast ice - are assumed to account for the observed T_B difference. Accurate geolocation of SMMR data is important during periods of pre-melt and onset of melt since the mis-classification of a SMMR footprint containing 50% snow-covered land resulted in an error of -3 K at 18 GHz, -6 K at 37 GHz, respectively, compared to a SMMR footprint over 100% fast ice. No significant change in T_B was observed for the melt period as long as land and ice were covered with wet snow.

Under certain circumstances, the polarization ratios of 18 and 37 GHz provide a possibility to classify ice types such as white ice, grey ice, nilas and open water. With the present resolution of the SMMR pixels (30x30 km for 37 GHz, 60x60 km for 18 GHz), this ice type classification seems feasible for large homogeneous ice areas depicting a single ice type. For mixed-ice SMMR footprints, a clear distinction is not possible.

A comparative analysis was carried out between estimates of ice concentrations derived from SMMR and Landsat data. Versions of the SMMR Team algorithm (ST_{18} and ST_{37}) and a single-channel linear interpolation algorithm (LI_{37}) were used to derive the SMMR ice concentration. During pre-melt and melt onset, the SMMR algorithms show less total ice concentration (3.5% for ST_{18}, 2.8% for ST_{37}, and 10% for LI_{37}) compared to the Landsat ice concentration. Largest differences (9.7% for ST_{18}, and 13.1% for ST_{37}) occurred during the melt

period (June 8, 1981). At high ice concentrations (according to the Landsat classification), the ST algorithms tend to show lower amounts of ice while, at low concentrations, ST yields greater amounts of ice. These differences may be due to the ability of SMMR to detect sub-resolution leads and thin ice types invisible on the Landsat images, and partially due to surface effects on the ice and open water. For individual footprints, the correlation coefficient for the SMMR ST_{18} and Landsat-derived concentrations varied between 0.78 (June 8, 1981) and 0.3 (May 5, 1981). The somewhat poor correlation coefficients for individual footprints can be attributed to the dynamic nature of the pack ice in the North Water area, and to the fact that 50% of the power received by the radiometer lies outside the FOV.

Satellite passive microwave data are essential for long-term monitoring of the sea ice cover in order to study climate fluctuations. In order to detect changes in the ice cover, the accuracy of ice parameters derived from passive microwave data must be known. The Landsat/SMMR comparison shows that the overall ice concentration can be retrieved from SMMR data to a comparative agreement of 3.5% during the pre-melt and onset of melt, and 10% during melt periods.

Acknowledgment

This work was supported by the Cooperative Institute for Research in Environmental Sciences (CIRES), University of Colorado at Boulder through a Visiting Fellowship for K.S. and in part through a National Science Foundation grant (DPP-8520883). We also acknowledge the National Snow and Ice Data Center (NSIDC) at CIRES for providing the gridded SMMR data, and the SMMR Information Processing Team of the Nimbus Project and the National Space Science Data Center for providing the CELL ALL SMMR tapes. We also thank Donald Cavalieri for helpful comments during the revision of this paper. The authors profited by the detailed and constructive comments of one reviewer.

References

Burns, B. A., D. J. Cavalieri, M. R. Keller, W. J. Campbell, T. C. Grenfell, G. A. Maykut, and P. Gloersen, Multisensor comparison of ice concentration in the Marginal Ice Zone, *J. Geophys. Res., 92(C7)*, 6843-6856, 1987.

Campbell, W. J., P. Gloersen, W. J. Webster, T. T. Wilheit, and R. O. Ramseier, Beaufort Sea ice zones as delineated by microwave imagery, *J. Geophys. Res., 81*, 1103-1110, 1976.

Campbell, W. J., J. Wayenberg, J. B. Ramseyer, R. O. Ramseier, M. R. Vant, R. Weaver, A. Redmond, L. Arsenault, P. Gloersen, H. J. Zwally, T. T. Wilheit, T. C. Chang, D. Hall, L. Gray, D. C. Meeks, M. L. Bryan, F. T. Barath, C. Elachi, F. Leberl, and T. Farr, Microwave remote sensing of sea ice in the AIDJEX main experiment, *Boundary-Layer Meteorol., 13*, 309-337, 1978.

Campbell, W. J., P. Gloersen, H. J. Zwally, R. O. Ramseier, and C. Elachi, Simultaneous passive and active microwave observations of near-shore Beauford sea ice, *J. Petroleum Techno., 32(6).*, 1105-1112, 1980.

Cavalieri, D. J., P. Gloersen, and W. J. Campbell, Determination of sea ice parameters with Nimbus 7 SMMR, *J. Geophy. Res., 89*, 5355-5369, 1984.

Campbell, W.J., P. Gloersen, E. G. Josberger, O. M. Johannessen, P. S. Guest, N. Mognard, R. Shuchman, B. A. Burns, N. Lannelongue, and L. L. Davidson, Variations of mesoscale and large-scale sea ice morphology in the 1984 Marginal Ice Zone Experiment as observed by microwave remote sensing, *J. Geophys. Res., 92(C7)*, 6805-6824, 1987.

Cavalieri, D. J., and S. Martin, A passive microwave study of polynyas along the antarctic Wilkes Land coast. Oceanology of the Antarctic Continental Shelf, *Antarctic Res. Series 43*, AGU, 227-252, 1985.

Cavalieri, D. J., P. Gloersen, and T. T. Wilheit, Aircraft and satellite passive microwave observations of the Bering sea ice cover during MIZEX West, *IEEE Trans. Geosci. Remote Sensing, GE-24(3)*, 368-377, 1986.

Comiso, J. C., Sea ice effective microwave emissivities from satellite passive microwave and infrared observations, *J. Geophy. Res., 88(C12)*, 7686-7704, 1983.

Comiso, J. C., Characteristics of arctic winter sea ice from satellite multispectral microwave observations, *J. Geophy. Res., 91(C1)*, 975-994, 1986.

Comiso, J. C., and H. J. Zwally, Antarctic sea ice concentration inferred from Nimbus 5 ESMR and Landsat imagery, *J. Geophy. Res., 87(C8)*, 5836-5844, 1982a.

Comiso, J. C., H. J. Zwally, and J. L. Saba, Radiative transfer modeling of microwave emission and dependence of firn properties, *Ann. Glaciol., 3*, 54-58, 1982b.

Foster, J. L., D. K. Hall, and A. T. C. Chang, An overview of passive microwave snow research and results, *Rev. Geophy. Space Phys., 22(2)*, 195-208. 1984.

Gloersen, P., W. Nordberg, T. J. Schmugge, T. T. Wilheit, and W. J. Campbell, Microwave signatures of first-year and multiyear sea ice, *J. Geophys. Res. 78*, 3564-3572, 1973.

Gloersen, P., T. T. Wilheit, T. C. Chang, W. Nordberg and W. J. Campbell,, Microwave maps of the polar ice of the earth, *Bull. Amer. Meteorol. Soc., 55(12)*, 1442-1448, 1974.

Gloersen, P., R. O. Ramseier, W. J. Campbell, T. C. Chang, and T. T. Wilheit, Variation of ice morphology of selected mesoscale test areas during the Bering Sea Experiment, *Proceedings of the Final Symposium on the Results of the Joint Soviet-American Expedition, Leningrad, May 12-17, 1974*, K. Ya. Kondratyev, Yu. I. Rabinovich, and W. Nordberg, ed., Gidrometeoizdat, Leningrad, 196-218, 1975a.

Gloersen, P., R. O. Ramseier, W. J. Campbell, P. M. Kuhn, and W. J. Webster, Ice thickness distribution as inferred from infrared and microwave remote sensing during the Bering Sea Experiment, *Proceedings of the Final Symposium on the Results of the Joint Soviet-American Expedition, Leningrad, May 12-17*, 1974, K. Ya. Kondratyev, Yu. I. Rabinovich, and W. Nordberg, ed., Gidrometeoizdat, Leningrad, 282-293, 1975b.

Gloersen, P., and F. T. Barath, A scanning multichannel microwave radiometer for Nimbus-G and Seasat-A, *IEEE J. Oceanic Engr. OE-2(2)*, 172-178, 1977.

Gloersen, P., H. J. Zwally, A. T. C. Chang, D. K. Hall, W. J. Campbell, and R. O. Ramseier, Time-dependence of sea ice concentration and multiyear ice fraction in the Arctic Basin, *Boundary-Layer Meteorol., 13,* 339-360, 1978.

Gloersen, P., and D. J. Cavalieri, Reduction of weather effects in the calculation of sea ice concentration from microwave radiances, *J. Geophy. Res., 91(C3),* 3913-3919, 1986.

Grenfell, T. C., Surface-based passive microwave observations of sea ice in the Bering and Greenland Sea, *IEEE Trans. Geosci. Remote Sensing, GE-24(3),* 378-382, 1986.

Grenfell, T. C., and A. W. Lohanick, Temporal variations of microwave signatures of sea ice during the late spring and early summer near Mould Bay NWT, *J. Geophy. Res., 90(C3),* 5063-5074, 1985.

Grenfell, T. C., and J. C. Comiso, Multifrequency passive microwave observations of first-year ice grown in a tank, *IEEE Trans. Geos. Remote Sensing, GE-24(6),* 826-831, 1986.

Ito, H., Sea ice atlas of northern Baffin Bay, *Zurcher Geogr. Schr. 7,* 142 pp., 1982.

Kondratyev, K. Ya., Yu. I. Rabinovich, and W. Nordberg, ed, *Proceedings fo the Final Symposium on the Results of the Joint Soviet-American Expedition, Leningrad, May 12-17, 1974,* Gidrometeoizdat, Leningrad, 316 pp, 1975.

Livingstone, Ch. E., K. P. Singh, and A. L. Gray, Seasonal and regional variations of active/passive microwave signatures of sea ice, *IEEE Trans. Geosci. Remote Sensing, GE-25(2),* 159-173, 1987.

Matzler, C., Microwave signatures of young sea ice and its influence on ice concentration algorithms, *Int. Arch. ISPRS, 34-VII/1,* 757-765, 1982.

Matzler, C., R. O. Ramseier, and E. Svensen, Polarization effects in sea-ice signatures, *IEEE J. Ocean. Engi., OE-9(5),* 333-338. 1984.

Muller, F., A. Ohmura, and R. J. Braithwaite, The North Water Project (Canadian Greenland Arctic), *Polar Geogr., 1(1),* 75-85, 1977.

Nakawo, M., and N. K. Sinha, Brine layer spacing of first-year sea ice, *Atm. Ocean 22(2),* 193-206, 1984.

Parkinson, C. L., J. C. Comiso, H. J. Zwally, D. J. Cavalieri, P. Gloersen, and W. J. Campbell, Arctic sea ice, 1973-1976: Satellite passive microwave observations, *NASA Spec. Publ., SP-489,* 296pp., 1987.

Ramseier, R. O., P. Gloersen, W. J. Campbell, and T. C. Chang, Mesoscale description for the principal Bering Sea ice experiment, *Proceedings of the Final Results of the Joint Soviet-American Expedition, Leningrad, May 12-17, 1974,* K. Ya. Kondratyev, Yu. I. Rabinovich, and W. Nordberg, ed., Gidrometeoizdat, Leningrad, 234-270, 1975.

Schanda, E., and R. Hofer, Microwave multispectral investigations of snow, *Proc. Int. Symp. Remote Sens. Environ., 11th,* 601-607, 1977.

Steffen, K., Warm water cells in the North Water, northern Baffin Bay during winter, *J. Geophy. Res., 90(C5),* 9129-9136, 1985.

Steffen, K., Ice conditions of an arctic polynya: North Water in winter, *J. Glaciol., 32(112),* 383-390, 1986.

Steffen, K., and A. Ohmura, Heat exchange and surface conditions in the North Water, northern Baffin Bay, *Ann. Glaciol., 6,* 178-181, 1985.

Steffen, K. and J. Lewis, Surface temperatures and sea ice typing for northern Baffin Bay, *Int. Jour. Remote Sensing* (in press).

Stiles, W. H., and F. T. Ulaby, The active and passive microwave response to snow parameter, 1, wetness, *J. Geophy. Res., 85,* 1037-1044, 1980.

Stogryn, A., A study of the microwave brightness temperature of snow from the point of view of strong fluctuation theory, *IEEE Trans. Geosci. and Remote Sensing GE-24(2),* 220-231, 1986.Svendsen, E., K. Kloster, B. Farrelly, O. M. Johannessen, H. A. Johannessen, W. J. Campbell, P. Gloersen, D. J. Cavalieri, and C. Matzler, Norwegian remote sensing experiment: Evaluation of the Nimbus-7 scanning multichannel microwave radiometer for sea ice research, *J. Geophys. Res., 88(C5),* 2781-2791, 1983.

Swift, C. T., and D. J. Cavalieri, Passive microwave remote sensing for sea ice research, *EOS, Dec. 3,* 1210-1213, 1985.

World Meteorological Organization, WMO Sea Ice Nomenclature, 147p., Geneva, 1970.

Zwally, H. J., J. C. Comiso, C. L. Parkinson, W. J. Campbell, F. D. Carsey, and P. Gloersen, Antarctic sea ice, 1973-1976: Satellite passive microwave observations, *NASA Spec. Publ., SP-459*, 206p, 1983.

Table 1. *Nimbus 7 SMMR brightness temperatures for white ice for northern Baffin Bay (ice concentration 10/10).*

Date	3/2/81	3/30/81	4/12/81	5/5/81	5/17/81	6/8/81
18GHz/H						
Mean T_B	228.7	230.3	229.0	232.2	226.3	215.8
S.D.	4.3	4.6	2.7	4.0	8.1	6.7
Max T_B	236.0	237.0	232.0	240.0	233.0	225.0
18GHz/V						
Mean T_B	237.0	238.1	238.1	243.9	241.1	234.5
S.D.	3.5	2.6	1.7	1.8	5.8	4.7
Max T_B	242.0	242.0	240.0	247.0	246.0	241.0
37GHz/H						
Mean T_B	229.3	229.9	226.9	231.8	230.0	209.2
S.D.	6.1	4.7	3.2	3.5	6.2	9.2
Max T_B	239.0	235.0	233.0	240.0	238.0	225.0
37GHz/V						
Mean T_B	235.4	236.3	233.7	241.2	242.1	225.3
S.D.	4.9	3.3	2.7	2.5	3.9	8.5
Max T_B	242.0	240.0	241.0	246.0	247.0	240.0

S.D.: Standard Deviation

Fig. 1 Map of northern Baffin Bay with North Water region.

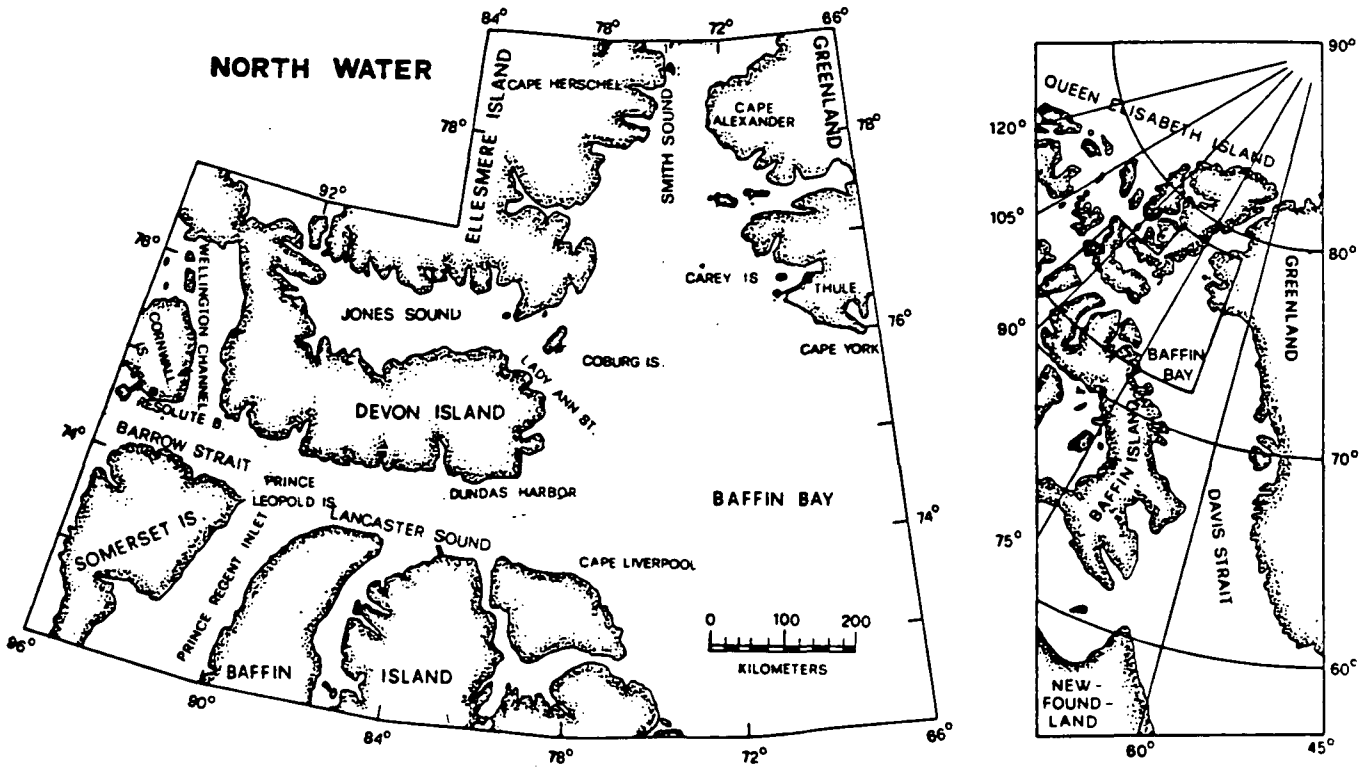

Fig. 2 *Change of salinity at different ice depths between Julian Day 300, 1980 (October 27) and Julian Day 77, 1981 (March 18) of the fast ice in Barrow Strait, N.W.T., Canada. Corresponding snow depth on the sea ice and total ice thickness are given in upper graph.*

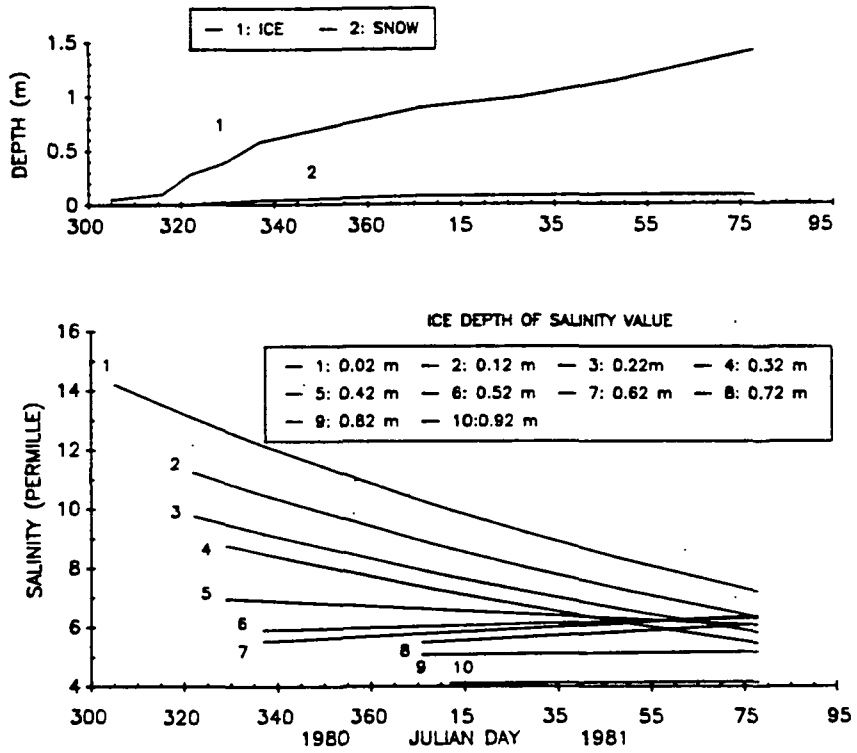

C-2

Fig. 3 *Frequency distribution of 18 and 37 GHz brightness temperatures at vertical and horizontal polarization for compact pack ice and fast ice during pre-melt (March 2, 1981) in northern Baffin Bay.*

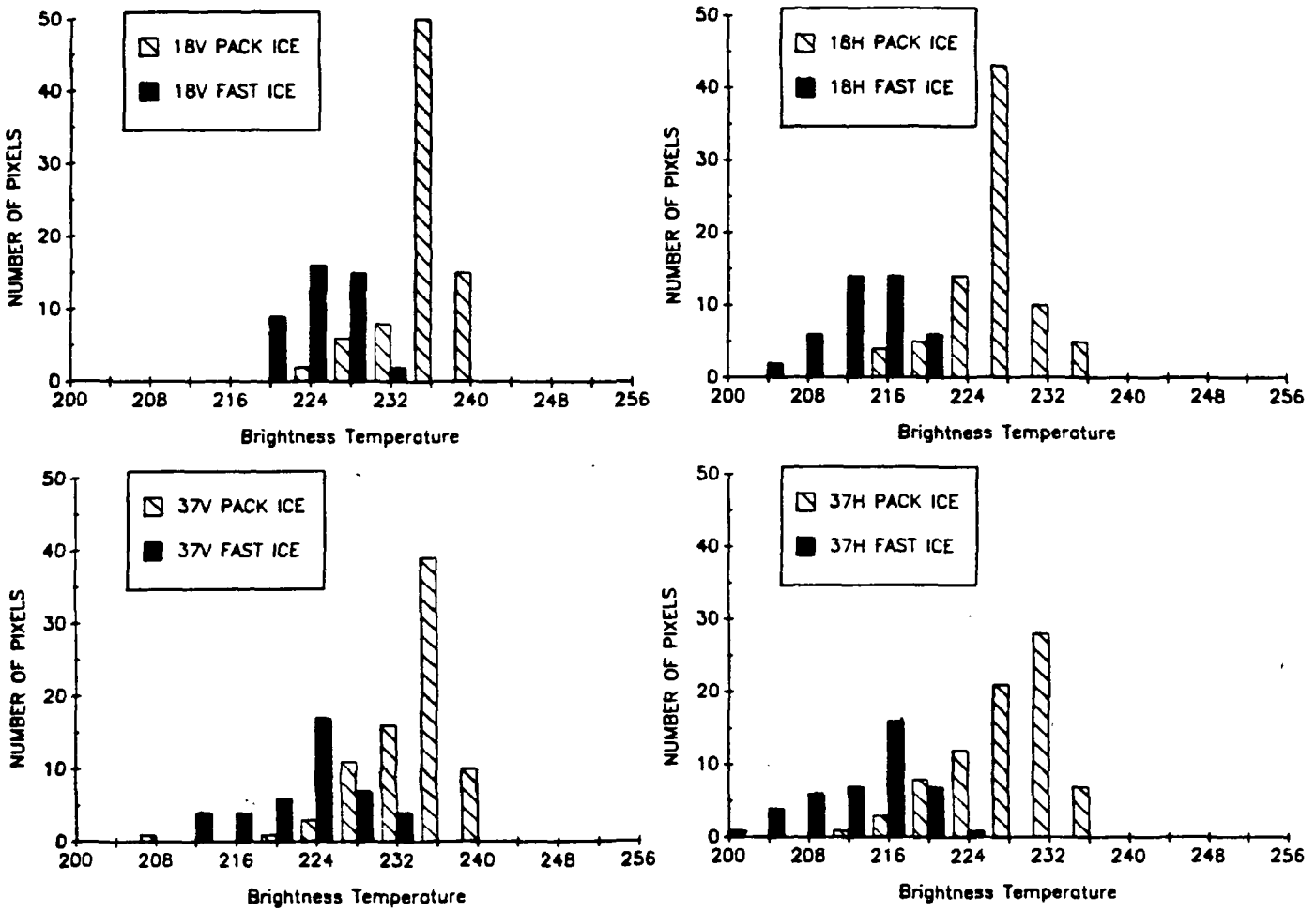

Fig. 4 *Same than Fig. 3 during onset of melt (May 5, 1981).*

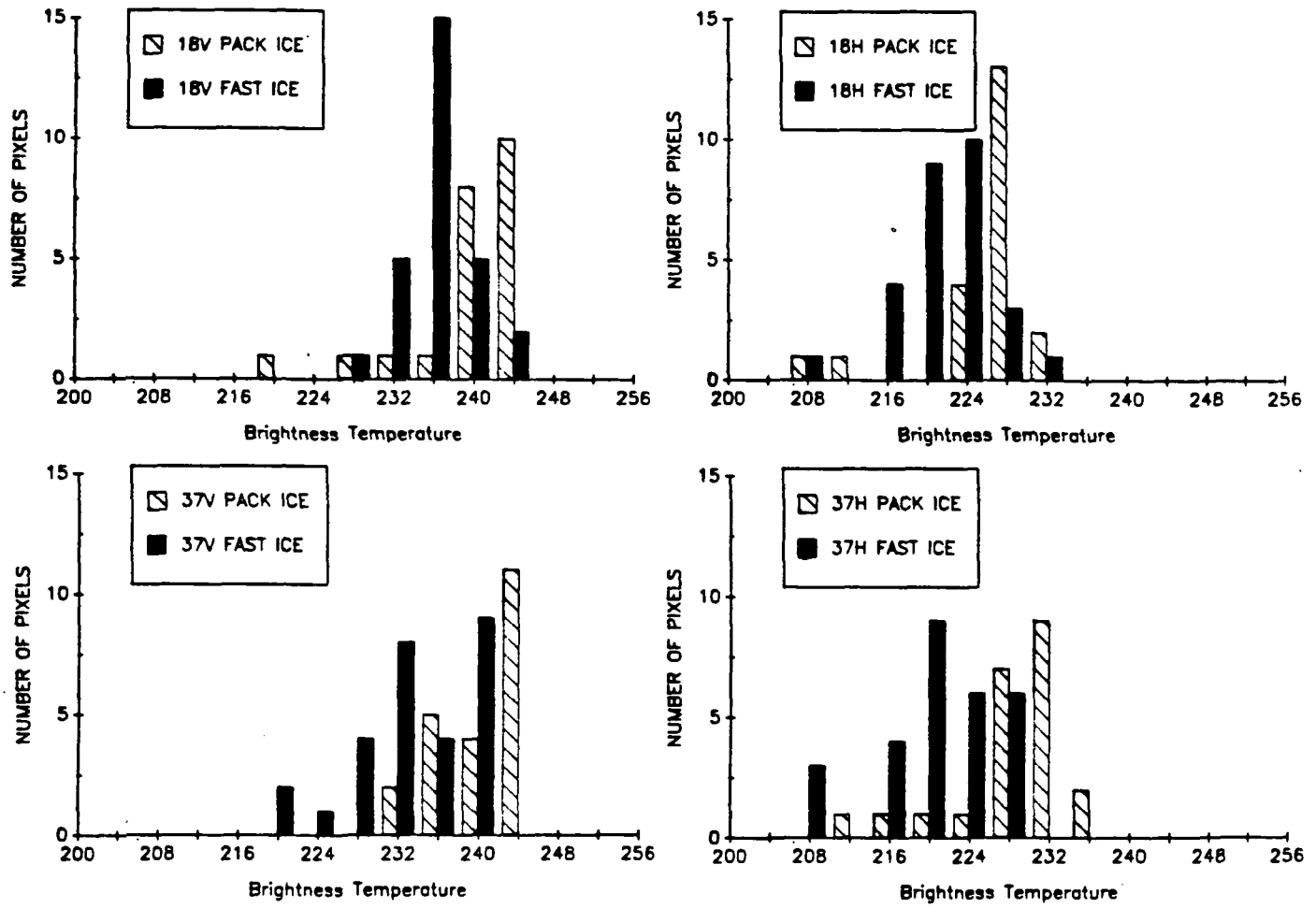

Fig. 5 Same than Fig. 3 during melt (June 8, 1981).

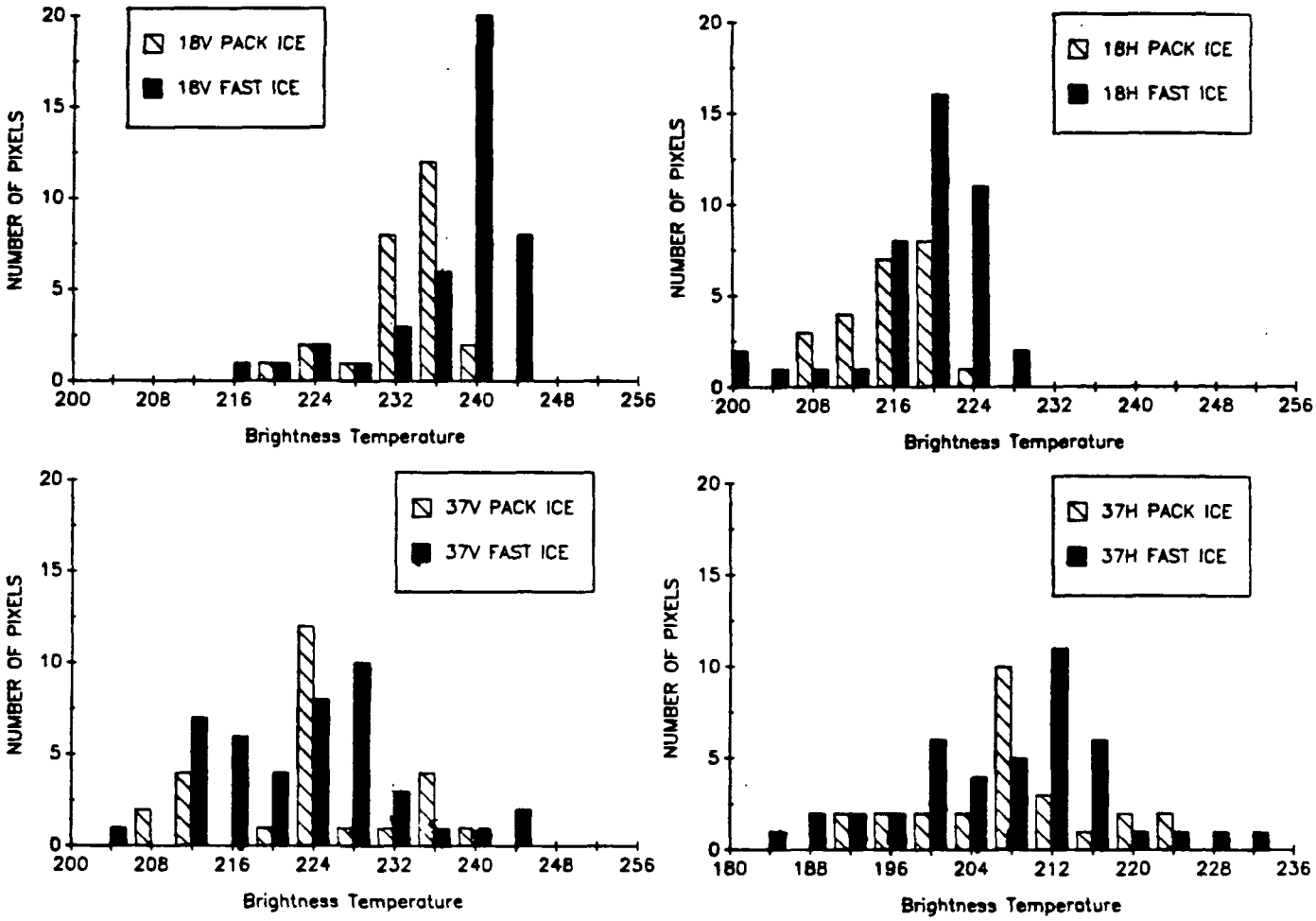

Fig. 6 *Seasonal variation of 18 and 37 GHz brightness temperatures (T_B) for fast ice and compact pack ice. The diamonds represent the mean T_B +standard deviation for horizontal and vertical polarization during pre-melt (black symbol; March 2, March 30, and April 12, 1981), onset of melt (dark-gray symbol; May 5, 1981, light-grey symbol; May 17, 1981) and melt period (white symbol; June 8, 1981).*

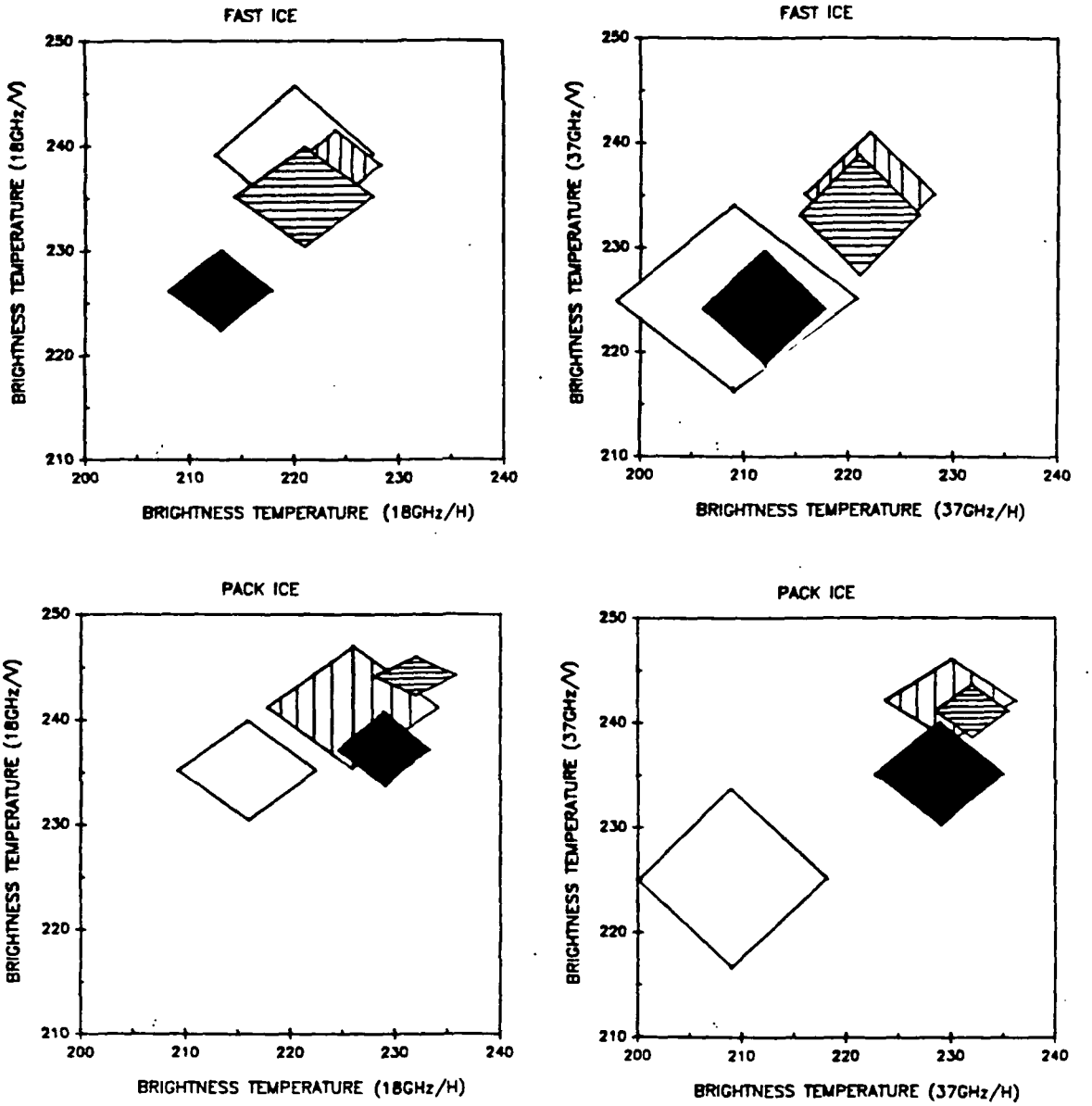

Fig. 7 *Change of mean fast ice brightness temperature (T_B) for SMMR footprints containing different percentages of land as classified by the Landsat data (pre-melt situation; March 2, 1981). The total amount of SMMR footprints used for the calculation is given on the right ordinate.*

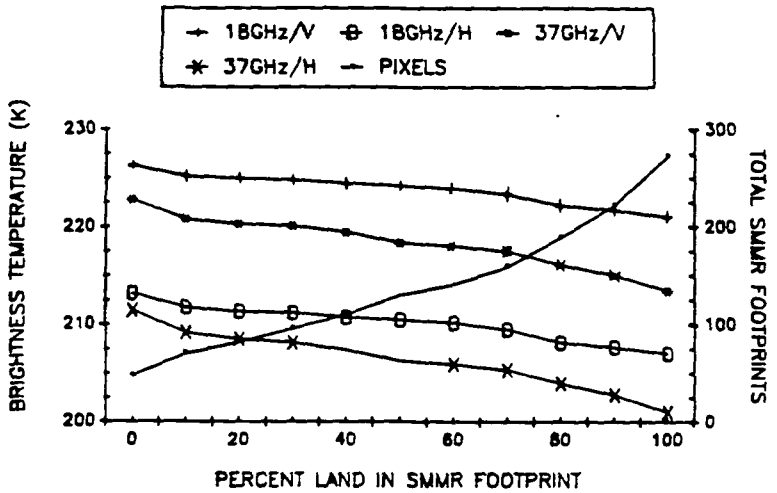

Fig. 8 *Polarization ratios (PR) at 18 and 37 GHz derived by intercomparison of Landsat and SMMR data for: (a) white ice (WI), grey ice (GI), nilas (NI) and open water (OW); (b) white ice/grey ice (WIGI), white ice/nilas (WINI), white ice/open water (WIOW) and grey ice/nilas (GINI); and (d) white-ice concentration. Figures 8a,b,d depict the polarization ratio +standard deviation, and Figure 8c shows the mean polarization value.*

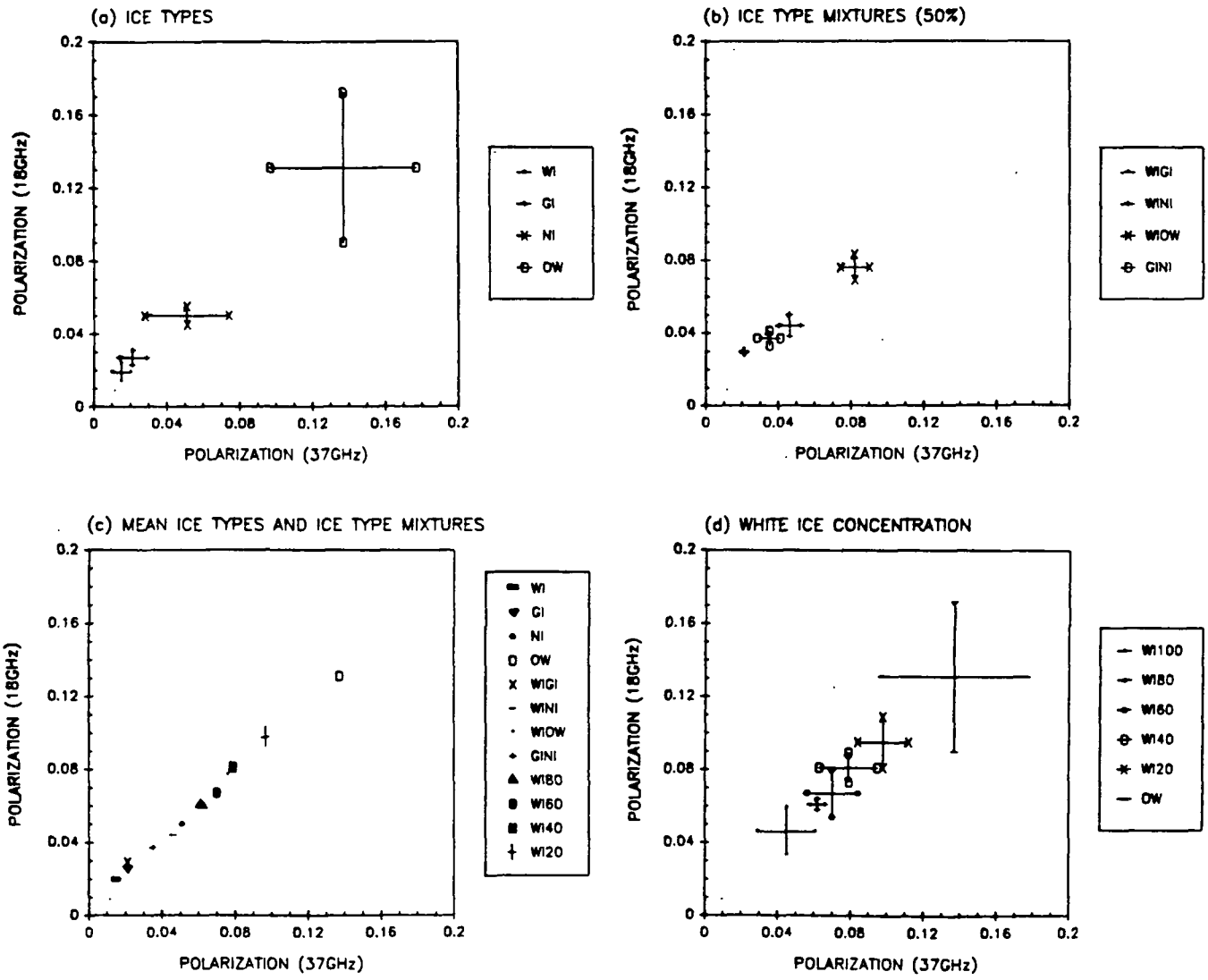

Fig. 9 *Brightness temperatures of compact pack ice at 18 and 37 GHz vertical and horizontal polarization for the northern Baffin Bay used as tie-points for retrieval of ice concentration from SMMR data.*

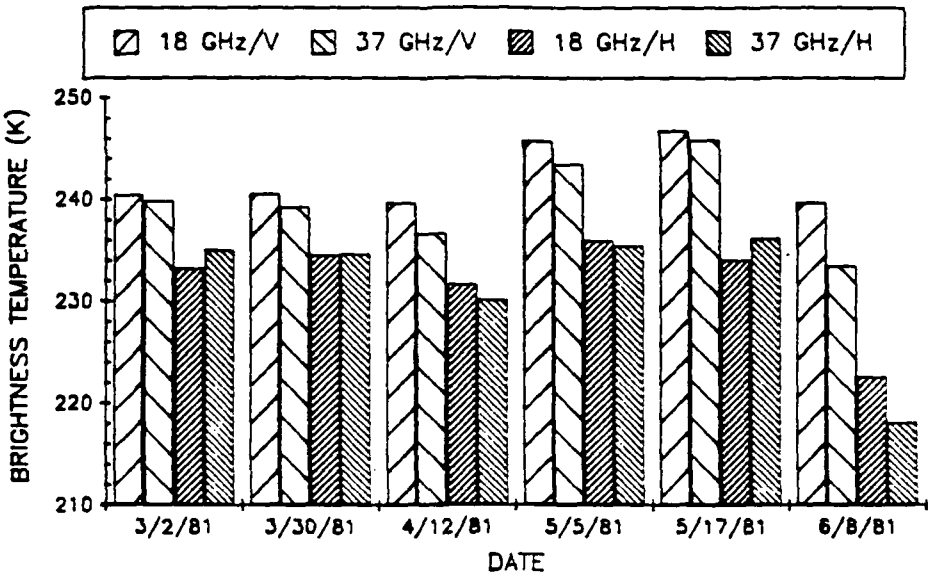

Fig. 10 *Total ice concentrations for northern Baffin Bay derived from SMMR data using the SMMR Team algorithm with 18 GHz (ST_{18}), 37 GHz (ST_{37}), and a linear interpolation algorithm with 37 GHz (LI_{37}). Landsat-derived concentrations are also shown.*

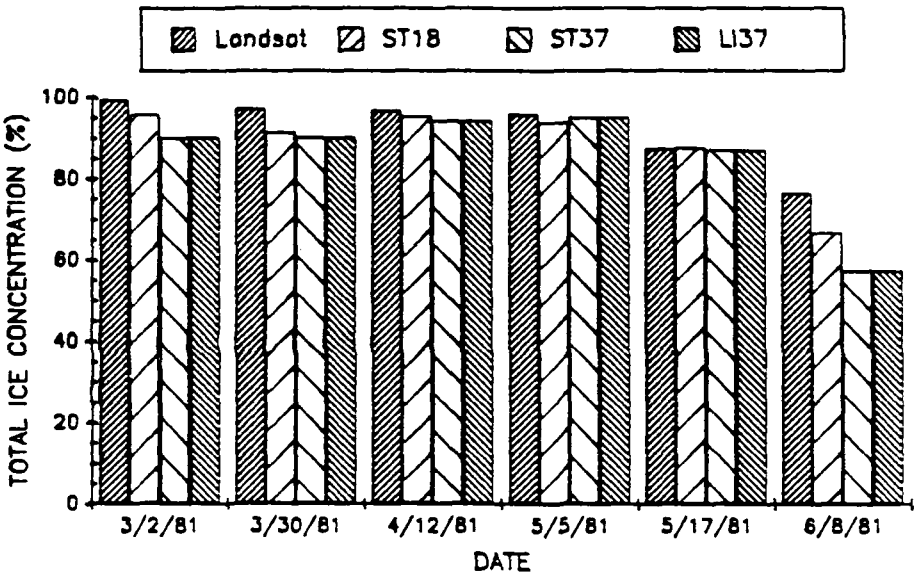

Fig. 11 *Scatter diagram of concentration estimates from Landsat and SMMR data for the melt period (June 8, 1981) in northern Baffin Bay. SMMR ice concentrations were derived with the ST_{18} algorithm.*

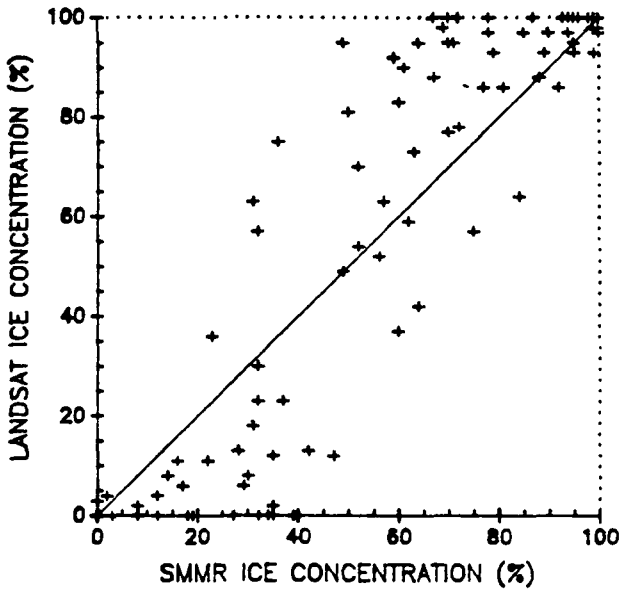

Fig. 12 *Correlation of SMMR-derived ice concentrations with Landsat-derived concentrations for individual SMMR-footprints. Ice concentrations were derived using the SMMR Team algorithm with 18 GHz (ST_{18}), 37 GHz (ST_{37}), and the linear interpolation algorithm with 37 GHz (LI_{37}).*